REPORT DOCUMENTATION PAGE

Form Approved
OMB No. 0704-0188

1. AGENCY USE ONLY *(Leave blank)*

2. REPORT DATE
8 May 1997

3. REPORT TYPE AND DATES COVERED
Final Technical Report 01/11/92-31/08/9

4. TITLE AND SUBTITLE
Momentum Transport in Turbulent Boundary Layers with Multiple Pressure Gradients

5. FUNDING NUMBERS
G-F49620-93-1-0003

6. AUTHOR(S)
A.C. Schwarz, M.W. Plesniak and S.N.B. Murthy

7. PERFORMING ORGANIZATION NAME(S) AND ADDRESS(ES)
Purdue University
School of Mechanical Engineering
1288 Mechanical Engineering Building
West Lafayette, IN 47907-1288

8.
AFOSR-TR-97
0565

9. SPONSORING/MONITORING AGENCY NAME(S) AND ADDRESS(ES)
AFOSR/NA
110 Duncan Avenue, Suite B115
Bolling AFB, DC 20332-0001

10. SPONSORING/MONITORING AGENCY REPORT NUMBER

11. SUPPLEMENTARY NOTES

12a. DISTRIBUTION/AVAILABILITY STATEMENT
Approved for public release; disbribution is unlimited.

12b. DISTRIBUTION CODE

13. ABSTRACT *(Maximum 200 words)*

An experimental study was performed to examine the effects of multiple extra rates of strain imposed on a turbulent boundary layer. This study is motivated by the necessity to develop predictive models of momentum and heat transport to facilitate design of turbomachinery, especially in the leading edge region of inlet guide vanes. The strain rates considered in the simplified experimental configuration resulted from wall curvature and axial pressure gradient. The effects of these strains on the transport of turbulence were studied for various combinations of strong and moderate curvature coupled with favorable and adverse pressure gradients. Extensive laser Doppler velocimetry measurements were made in a low-speed water channel, with an ability to resolve the near-wall region. Mean velocities, Reynolds stresses and production terms were computed from the measurements. Time-resolved velocity records were used to infer turbulent burst period and ejection duration using the uv2 quadrant technique, with grouping. The results revealed that the strain rates interacted nonlinearly and that the rate of application was at least as important as the magnitude of the applied strains. The friction velocity provided appropriate scaling for Reynolds stresses in the inner layer, but outside of the logarithmic layer large changes caused by the extra strains were not compensated by this scale. An analytical framework based on the orientation of the principle axes of the strain rate and Reynolds stress tensors was evaluated.

14. SUBJECT TERMS
turbulence, boundary layer, curvature, multiple strains, bursting, pressure gradient, turbine cooling

15. NUMBER OF PAGES
115

16. PRICE CODE

17. SECURITY CLASSIFICATION OF REPORT	**18. SECURITY CLASSIFICATION OF THIS PAGE**	**19. SECURITY CLASSIFICATION OF ABSTRACT**	**20. LIMITATION OF ABSTRACT**
Unclassified	Unclassified	Unclassified	UL

NSN 7540-01-280-5500

DTIC QUALITY INSPECTED 3

Standard Form 298 (Rev. 2-89)
Prescribed by ANSI Std Z39-18

Final Technical Report

MOMENTUM TRANSPORT IN TURBULENT BOUNDARY LAYERS WITH MULTIPLE PRESSURE GRADIENTS

(Project Period: 01 Nov 92 – 31 Aug 96)
Grant No. F49620–93–1–0003

by

Andreas C. Schwarz, Graduate Research Assistant

Michael W. Plesniak, Principal Investigator
Tel: (765) 494–1537

and

S.N.B. Murthy, Co–principal Investigator
Tel: (765) 494–1509

Purdue University
School of Mechanical Engineering
Thermal Sciences and Propulsion Center
West Lafayette, IN 47907–1003

Prepared For:
Air Force Office of Scientific Research/NA
110 Duncan Avenue Suite B115
Bolling AFB, DC 20332–0001

Attention: Drs. James M. McMichael and Mark Glauser
Program Managers

May 1997

REPORT DOCUMENTATION PAGE

Form Approved
OMB No. 0704-0188

1. AGENCY USE ONLY *(Leave blank)*

2. REPORT DATE
8 May 1997

3. REPORT TYPE AND DATES COVERED
Final Technical Report 01/11/92-31/08/96

4. TITLE AND SUBTITLE
Momentum Transport in Turbulent Boundary Layers with Multiple Pressure Gradients

5. FUNDING NUMBERS
G-F49620-93-1-0003

6. AUTHOR(S)
A.C. Schwarz, M.W. Plesniak and S.N.B. Murthy

7. PERFORMING ORGANIZATION NAME(S) AND ADDRESS(ES)
Purdue University
School of Mechanical Engineering
1288 Mechanical Engineering Building
West Lafayette, IN 47907-1288

8. PERFORMING ORGANIZATION REPORT NUMBER

9. SPONSORING/MONITORING AGENCY NAME(S) AND ADDRESS(ES)
AFOSR/NA
110 Duncan Avenue, Suite B115
Bolling AFB, DC 20332-0001

10. SPONSORING/MONITORING AGENCY REPORT NUMBER

11. SUPPLEMENTARY NOTES

12a. DISTRIBUTION/AVAILABILITY STATEMENT
Approved for public release; disbribution is unlimited.

12b. DISTRIBUTION CODE

13. ABSTRACT *(Maximum 200 words)*

An experimental study was performed to examine the effects of multiple extra rates of strain imposed on a turbulent boundary layer. This study is motivated by the necessity to develop predictive models of momentum and heat transport to facilitate design of turbomachinery, especially in the leading edge region of inlet guide vanes. The strain rates considered in the simplified experimental configuration resulted from wall curvature and axial pressure gradient. The effects of these strains on the transport of turbulence were studied for various combinations of strong and moderate curvature coupled with favorable and adverse pressure gradients. Extensive laser Doppler velocimetry measurements were made in a low-speed water channel, with an ability to resolve the near-wall region. Mean velocities, Reynolds stresses and production terms were computed from the measurements. Time-resolved velocity records were used to infer turbulent burst period and ejection duration using the uv2 quadrant technique, with grouping. The results revealed that the strain rates interacted nonlinearly and that the rate of application was at least as important as the magnitude of the applied strains. The friction velocity provided appropriate scaling for Reynolds stresses in the inner layer, but outside of the logarithmic layer large changes caused by the extra strains were not compensated by this scale. An analytical framework based on the orientation of the principle axes of the strain rate and Reynolds stress tensors was evaluated.

14. SUBJECT TERMS
turbulence, boundary layer, curvature, multiple strains, bursting, pressure gradient, turbine cooling

15. NUMBER OF PAGES
115

16. PRICE CODE

17. SECURITY CLASSIFICATION OF REPORT
Unclassified

18. SECURITY CLASSIFICATION OF THIS PAGE
Unclassified

19. SECURITY CLASSIFICATION OF ABSTRACT
Unclassified

20. LIMITATION OF ABSTRACT
UL

NSN 7540-01-280-5500

Standard Form 298 (Rev. 2-89)
Prescribed by ANSI Std Z39-18

TABLE OF CONTENTS

Page

LIST OF TABLES

LIST OF FIGURES

NOMENCLATURE

English Symbols

A_{ij}	Advection tensor (Eqn. 1.1)
$\tilde{A}_{ij}$	Rate of deformation tensor
B	Log-law slope intercept
c_f	Skin friction coefficient, $c_f = 2\tau_w / \left(\rho U_{pw}^2\right) = 2\left(u_\tau / U_{pw}\right)^2$
D_{ij}	Dissipation tensor (Eqn. 1.1)
e	Extra rate-of-strain, $e = \partial \overline{V} / \partial x$
f_{vis}	Viscous frequency,. $f_{vis} = \partial \overline{U} / \partial y\big|_{wall} \approx u_\tau^2 / \nu$
FPG	Favorable pressure gradient
H	Shape factor, $H = \delta^* / \theta$
h	Curvature correction factor, $h = 1+y/R$
G	Clauser equilibrium shape factor (Eqn. 4.4)
k	Acceleration parameter, $k = \nu / U_e^2 \cdot dU_e / ds$
L	Large-eddy (integral) length scale
n	Wall-normal streamline coordinate
P	Mean static fluid pressure
P_{ij}	Production tensor (Eqn. 1.1)
P_{rat}	Pressure gradient ratio, $P_{rat} = \left\|dP / ds\right\| / (dP / dn)$
$\overline{q^2} / 2$	Turbulent kinetic energy
R	Radius of curvature
r	Streamline curvature, $r = R+n$
Re	Reynolds number
Re_t	Turbulence Reynolds number, $Re_t = u_{RMS} L / \nu$
Re_θ	Momentum thickness Reynolds number, $Re_\theta = U_{pw} \theta / \nu$

S.G.	Specific Gravity
S_{ij}	Strain rate tensor
S_{rad}	Radial strain rate ratio, $S_{rad} = \left(\overline{U}/r\right)\left(\partial\overline{U}/\partial n\right)$
s	Streamwise coordinate
s_o	Location of onset of curvature
SFPG	Strong favorable pressure gradient
T_E	Large eddy lifetime
t_D	Distortion time scale
t_L	Lagrangian time scale
$\overline{T}_B$	Mean burst period
$T_{B,in}$	Mean inner normalized burst period (Eqn. 5.1)
$T_{B,out}$	Mean outer normalized burst period (Eqn. 5.2)
$\overline{T}_E$	Mean ejection duration
U(t)	Instantaneous streamwise velocity
U^+	Inner normalized streamwise velocity, $U^+ = \overline{U}/u_\tau$
U_c^+	Inner normalized, curvature corrected streamwise velocity, $U_c^+ = \frac{\overline{U}}{u_\tau}\cdot\frac{(R+y)}{R}$
U_e	Streamwise velocity at edge of boundary layer
U_{pw}	Potential wall velocity
u(t)	Instantaneous streamwise velocity fluctuation, $u(t) = U(t) - \overline{U}$
u′	Streamwise RMS velocity
u_τ	Shear velocity, $u_\tau = \sqrt{\tau_w/\rho}$
$\overline{uv}$	Primary Reynolds shear stress (divided by ρ), $\overline{uv} = \overline{\left[\left(U(t)-\overline{U}\right)\left(V(t)-\overline{V}\right)\right]}$
V(t)	Instantaneous wall-normal velocity
$\overline{V}$	Mean wall-normal velocity
v(t)	Instantaneous wall-normal velocity fluctuation, $v(t) = V(t) - \overline{V}$
v′	Wall-normal RMS velocity
X	Large eddy memory time (Eqn. 4.1)
x	Streamwise cartesian coordinate
y	Wall-normal coordinate

y^+	Inner normalized wall-normal coordinate, $y^+ = yu_\tau / \nu$
ZPG	Zero pressure gradient
z	Spanwise coordinate

Greek Symbols

α	Streamwise angular position in curved test section
α_{eff}	Effective strain parameter (Eqn. 1.4)
α_{ReS}	Angle of Reynolds stress tensor principal axes (Eqn. 5.6)
α_{SR}	Angle of strain rate tensor principal axes (Eqn. 5.5)
β	Pressure gradient parameter, $\beta = \delta^* / \tau_w \cdot dP / ds$
β_{TSt}	Total strain parameter (Eqn. 5.8)
Δ	Clauser equilibrium thickness (Eqn. 4.3)
Δ_{ij}	Diffusion tensor (Eqn. 1.1)
Δ_E^+	Mean inner normalized ejection duration, $\Delta_E^+ = \overline{T}_E u_\tau^2 / \nu$
Δ_P	Pressure gradient parameter, $\Delta_P = \nu / \left(\rho u_\tau^2\right) \cdot dP / ds$
Δk^+	Perturbation wall curvature parameter, $\Delta k^+ = \Delta R \nu / u_\tau$
δ	Boundary layer thickness
δ^*	Displacement thickness
ε	Isotropic turbulent dissipation rate
ϕ_{ij}	Pressure-strain tensor (Eqn. 1.1)
κ	Van Kármán constant
μ	Dynamic fluid viscosity
ν	Kinematic fluid viscosity
ω_z	Spanwise vorticity component
Π_i	Independent dimensionless parameters
ρ	Fluid density
θ	Momentum thickness
τ_w	Wall shear stress, $\tau_w = \mu \, \partial \overline{U} / \partial y \|_{y=0}$

ABSTRACT

An experimental study was performed to examine the effects of multiple extra rates of strain imposed on a turbulent boundary layer. This study is motivated by the necessity to develop predictive models of momentum and heat transport to facilitate design of turbomachinery, especially in the leading edge region of inlet guide vanes. The strain rates considered in the simplified experimental configuration resulted from wall curvature and axial pressure gradient. The effects of these strains on the transport of turbulence were studied for various combinations of strong and moderate curvature coupled with favorable and adverse pressure gradients. Extensive laser Doppler velocimetry measurements were made in a low-speed water channel, with an ability to resolve the near-wall region. Mean velocities, Reynolds stresses and production terms were computed from the measurements. Time-resolved velocity records were used to infer turbulent burst period and ejection duration using the uv2 quadrant technique, with grouping. The results revealed that the strain rates interacted nonlinearly and that the rate of application was at least as important as the magnitude of the applied strains. The friction velocity provided appropriate scaling for Reynolds stresses in the inner layer, but outside of the logarithmic layer large changes caused by the extra strains were not compensated by this scale. An analytical framework based on the orientation of the principle axes of the strain rate and Reynolds stress tensors was evaluated.

CHAPTER 1. INTRODUCTION AND LITERATURE REVIEW

1.1 Introduction

There are many practical flows of engineering interest which are influenced by multiple, interacting strains. For example, the momentum and heat transfer mechanisms in turbomachinery are highly complex due to curved surfaces, low aspect ratio passages and streamwise and spanwise strains. In Figure 1.1, a schematic of a typical blade passage is depicted with the emphasis on the surface curvatures, the leading edge of the turbine blade and the changes in the cross-sectional area between the blades. With the desire to achieve higher thrust-to-weight ratios in turbomachines, it has become increasingly important to understand the fundamental mechanisms of momentum and heat transfer because of the required higher turbine inlet temperatures. Other examples of highly complex thermal systems include internal combustion (I.C.) engines as well as several external flow situations such as submersibles, aviatory vehicles, et cetera.

The hierarchy of turbulent flows begins with isotropic turbulence, then homogeneous but non-isotropic flows without a mean velocity gradient to a plane strain acting on initially isotropic turbulence (see Gence and Mathieu, 1979). In the latter case, the principal axes of the Reynolds shear stress tensor coincide with those of the mean rate of strain. The next step in the hierarchy of turbulent flows involves the action of a constant shear on an initially isotropic turbulence, where the mean gradient is compounded by a pure plane strain associated with mean rotation. In this case, the principal axes of the Reynolds stress tensor are not aligned with those of the strain rate tensor, because of the mean rotation. An overview of the different complexities in turbulent flow is shown in Figure 1.2.

The effects of single extra strain rates on the structure of a two-dimensional turbulent boundary layer (TBL) have been thoroughly studied. However, turbulent flow fields that involve extra rates-of-strain such as streamwise curvature or lateral divergence can not be predicted with acceptable accuracy by the same methods that were developed for classical shear layers (see Bradshaw, 1975). The TBL developing over a curved wall is considered to be a complex turbulent flow, since an "additional strain" associated with curvature of the mean streamlines is added to simple shear. Bradshaw (1973) defined an extra strain rate as any rate-of-strain component, denoted in general by the symbol e, other than the a simple shear $\partial\overline{U}/\partial y$. In a curved shear layer the extra rate-of-strain is $e = \partial\overline{V}/\partial x$ in (x,y) coordinates, or $e = -\overline{U}/(R+n)$ in (s,n) coordinate system.

A number of researchers have studied the influence of additional rates of strain, e.g. convex and concave curvature (cf. So and Mellor, 1973; Gillis and Johnston, 1983; Muck *et al.*, 1985; Barlow and Johnston, 1988a, b), as well as adverse and favorable streamwise pressure gradients, (cf. Kline *et al.*, 1967; Narashimha and Sreenivasan, 1979; White and Tiederman, 1990; and Nagano *et al.*, 1991). Even though the response in laminar flows to multiple strain rates can be expected to obey simple mechanical laws for combinations of strains in a Newtonian fluid, the effects of the individual strain rates in the presence of turbulence may not be supersposable in a linear fashion, since turbulent motions are affected over all scales. Thus, there remains a significant need for detailed experimental studies of the response and downstream development of a TBL subjected to multiple strain rates.

1.2 Literature Review

Several aspects of complex turbulent flows have been studied extensively, and are well known. While an exhaustive review of all complex flow literature is not feasible within the contraints of this report, this section will summarize research efforts in the area of streamline curvature, streamwise pressure gradients and a few selected attempts of investigating the effects of multiple strain rates on the turbulence structure.

1.2.1 Streamline Curvature

Streamline curvature effects have been extensively studied for about three decades. The emphasis has been on the experimental exploration of how streamline curvature (both convex and concave) affects the turbulence structure of both external and internal flow fields. Table 1.1 summarizes some groundbreaking work done in this area. Bradshaw (1973) noted in his review of streamline curvature, that the effects of extra strain rates are an order of magnitude greater than would be predicted by a straightforward extension of simple shear layer calculations. Here, the extra rate of strain is $\partial\overline{V}/\partial x = -\overline{U}/R_{st}$, where R_{st} is the streamline curvature. The interpretation problem of the unexpected influences of the extra rates of strain due to streamline curvature arises from the fact that the extra strain rate $\partial \overline{V} / \partial x = \{O(\delta / R)\}\ \partial \overline{U} / \partial y$, whereas the production term (P_{ij}) of the Reynolds stress transport equations is usually an order of magnitude larger than the advection term (A_{ij}), or in more general terms $P_{ij} = \{O(L / \delta)\}\ A_{ij}$ (van den Berg, 1984), where L is a typical streamwise length scale. The mismatch between the orders of magnitude of these terms and the relatively large changes in the production due to small extra rates of strain is attributed to the pressure-strain term, ϕ_{ij}. Using van den Berg's notation, the transport equation for the turbulent stress component $\overline{u_i u_j}$ is written as:

$$A_{ij} = P_{ij} - \Delta_{ij} - D_{ij} + \phi_{ij} \tag{1.1}$$

where Δ_{ij} is the diffusion term and D_{ij} the dissipation term. Note that the dissipation term only accounts for the final (isotropic) stage in the turbulent scale cascade process, where the smallest eddies of the flow dissipate their energy by viscosity.

In a more recent review on the effects of streamwise curvature effects in turbulent boundary layers by Patel and Sotiropolous (1997), the authors analyzed a number of experiments to elucidate the effects of curvature and to evaluate turbulence models to predict transport of momentum and heat in turbulent boundary layers. Their main conclusion was that, in spite of the high level of effort that has been devoted to this subject, little progress has been made in quantifying all of the effects of streamwise curvature. As far as the effects of convex curvature are concerned, the authors concluded that the usual integral parameters (H and c_f), profiles of the mean velocity and some key turbulence quantities (i.e. TKE, turbulent shear stress, and ratio of normal to streamwise turbulent stresses) are sufficient to observe the effects of convex curvature.

An additional problem with the extra strain rate due to streamline curvature $\partial \overline{V} / \partial x$, is that the velocity derivative is not Galilean invariant, because it is referred to axes aligned with the streamwise velocity (Spalart and Shur, 1997). It is impossible to interprete $\partial \overline{V} / \partial x$ as an "extra rate of strain", because it has been shown to have a significant effect on the turbulence (Bradshaw, 1973), even though values of $\partial \overline{V} / \partial x$ are much smaller than that of $\partial \overline{U} / \partial y$ and they are equal partners of the spanwise component of vorticity, ω_z. Therefore, it becomes more appropriate to introduce a Galilean invariant measure in order to develop more general turbulence problems.

As reported in previous studies (e.g. So and Mellor, 1973 and Gillis and Johnston, 1983), a significant favorable pressure gradient occurs on the convex wall at the onset of curvature, where the radius of curvature changes from infinity to a finite value. This behavior can be predicted by combining the Euler equations in the streamwise and wall-normal direction.

$$\frac{\partial P}{\partial s} = -\rho V \frac{\partial V}{\partial s} = -\frac{\rho}{2}\frac{\partial \left(V^2\right)}{\partial s} \tag{1.2.a}$$

$$\frac{\partial P}{\partial n} = \rho \frac{V^2}{R} \quad \Rightarrow \quad V^2 = \frac{R}{\rho}\frac{\partial P}{\partial n} \tag{1.2.b}$$

Combining equations 1.2.a and 1.2.b yields:

$$\frac{\partial P}{\partial s} = -\frac{1}{2}\frac{\partial}{\partial s}\left(R\frac{\partial P}{\partial n}\right) = -\frac{R}{2}\frac{\partial}{\partial s}\left(\frac{\partial P}{\partial n}\right) \tag{1.3}$$

Equation 1.3 shows how the streamwise pressure gradient arises as a consequence of changes in the radius of curvature.

One of the first thorough experimental investigations of turbulent flow over curved surfaces with strong curvature ($\delta_0 / R \approx 0.10$, where δ_0 is the initial boundary layer thickness upstream of the onset of curvature and R is the radius of curvature) was performed by So and Mellor (1973). On the convex wall it was found that the turbulent boundary layer was two-dimensional and that the turbulent shear stress vanished in the outer half of the boundary layer. A zero streamwise pressure gradient was maintained over the convex wall by carefully contouring the opposite wall except immediately downstream of the onset of curvature, where locally a favorable pressure gradient prevailed.

Two experiments with different strengths of curvature ($\delta_0 / R \approx 0.10$ and 0.05) were performed by Gillis and Johnston (1983) in a low-speed wind tunnel to study the turbulence structure of the boundary layer that formed over the convex wall, and after 90° of turning, its recovery behavior on a flat surface. The streamwise pressure gradient was forced to be zero over the entire test surface, requiring careful design of the wall opposite the curved test wall. Consistent with the results of So and Mellor (1973), they found that the primary Reynolds shear stress was diminished in the outer region of the turbulent boundary layer, and that the shear stress profiles for both experiments collapsed when

$-\overline{uv}/u_\tau^2$ was plotted versus distance from the wall normalized with the wall radius of curvature, y/R, indicating that the radius of curvature influences the active turbulence length scales in curved boundary layers with strong curvature. Here, $-\overline{uv}$ is the primary Reynolds shear stress (divided by the fluid density ρ) and u_τ is the shear velocity defined as $u_\tau = (\tau_w/\rho)^{1/2}$. The active shear-layer in the downstream region was thinner than its initial value at the onset of curvature.

The structure of mildly curved convex and concave turbulent boundary layers ($\delta_o/R = \pm\, 0.01$) was studied by Ramaprian and Shivaprasad (1978). With detailed turbulence measurements, they found that even mild curvature has very strong effects on the various aspects of the turbulence structure. The turbulence energy production rate was significantly affected by convex curvature, where the production mechanism is confined to a region very close to the wall. In addition, convex curvature not only suppressed both the amount of outward diffusion of turbulent kinetic energy (TKE) from the wall region and the extent of the region which receives TKE from the wall region, but also the integral time scales were strongly affected especially by convex curvature. The authors concluded that the structure (size, orientation and decay time) of the energy containing eddies is highly sensitive to wall curvature.

The effect of mild convex curvature ($\delta_o/R \approx 0.01$) was also investigated by Gibson *et al.* (1984), where four non-zero components of the Reynolds stress tensor and three triple velocity products were obtained at different downstream positions of an open-return blower-type wind tunnel. The turbulence intensities, shear stress and wall friction were all reduced by approximately 10% relative to their flat-plate values and the triple products were halved in the presence of mild convex curvature. Apparently, the initial response of the TBL to the change in wall curvature was triggered by the effects of the extra strain, which resulted in the reduction of the rate of shear stress production from the mean flow. Because the radial strain rate ratio, $S_{rad} = (\overline{U}/r)/(\partial\overline{U}/\partial y)$, increases with distance from the wall (y), the effect of the extra strain rate due to curvature on the shear stress is most effective outside the near-wall region.

In order to clearly distinguish between turbulent and non-turbulent flow regimes in a TBL over a mildly curved convex wall ($\delta_o/R \approx 0.01$), conditional-sampling techniques were used in an investigation by Muck *et al.* (1985). In conjunction with the work by Hoffman *et al.* (1985), who studied concave curvature effects, it was demostrated that the effects of convex (stabilizing) and concave (destabilizing) curvature are completely different. The most obvious evidence in these two studies was the very rapid response of the TBL to the application or removal of convex curvature, as compared to the slow reaction to concave curvature. This information was considered crucial for refining existing calculation methods for turbulent flows with streamwise curvature.

The (lack of) applicability of the "log-law" in TBLs with one or more extra rates-of-strain has been widely discussed. In a comprehensive study by Gibson (1988) on the effects of surface curvature, it was shown that although the logarithmic region existed for the mean streamwise velocity component, the "log-law" constants could be different from the standard values (1/0.41 for the slope and 5.0 for the intercept). In his work, Gibson (1988) suggested a value of 5.78 for the intercept, while the von Kármán constant remained unchanged. A more extensive discussion of this issue can be found in Schwarz & Plesniak (1996b).

In an extensive visual study on the effects of stabilizing convex curvature (with $\delta_0/R \approx 0.05$), Chiwanga and Ramaprian (1993) showed that the large-scale structures were highly attenuated by convex wall curvature, confirming that the curved TBL is dominated by smaller scale motions. The attenuation of the large-scale structures was expected to result in a substantial loss of upstream history of the boundary layer. In the recovery zone, the TBL tried to reorganize itself, but approximately 33 δ_0 were required after the end of curvature to identify large-scale structures again.

A thorough study of the effects of concave curvature on the turbulence structure was conducted by Barlow and Johnston (1988a and 1988b) in a low-speed, free surface water channel using flow visualization and two-component laser-Doppler velocimetry. The strength of the concave curvature was moderate at $\delta_0/R \approx 0.06$. The overall results showed that large-scale motions were amplified by the destabilizing curvature in a two-stage process. The new eddy structure which developed over at least 20 δ_0 downstream of the onset of curvature enhanced the mixing across the boundary layer, which could be seen in the spectral measurements and an increase in the correlation coefficient. For the natural flow experiment, the large-scale did not have a preferred spanwise location and the TBL remained nearly two-dimensional in the mean. On the other hand, in the presence of upstream vortex generators, a fixed array of longitudinal roll cells were induced allowing measurements to be made in large inflow and outflow region, respectively. Under these conditions, the bursting process and the $\overline{uv}$ correlations were suppressed in the inflow regions, whereas the opposite trend was observed for the outflow regions. A turbulence model for concave boundary layer flows must accurately account for the slow development of the large-scale structures.

1.2.2 Streamwise Pressure Gradients

The level at which streamwise pressure gradients interact with turbulent flow is not well understood. For example, the absolute turbulence properties appear to be only slightly affected by pressure gradient (Bradshaw, 1994), because the Reynolds stress transport equations do not explicitly contain the mean pressure. The only terms that are directly affected are the y-components diffusion terms.

The influence of additional strain rates due to adverse and favorable streamwise pressure gradients has been studied extensively. Both adverse and favorable streamwise pressure gradients can have significant effects on the mean flow and the turbulence quantities. Several conditions have been shown to destroy the log-law region, i.e. strongly accelerating flow leading to relaminarization (cf. Blackwelder and Kovasznay, 1972; and Narashimha and Sreenivasan, 1983), increasingly adverse, non-equilibrium pressure gradients (cf. Nagano *et al.*, 1991), and TBLs with alternating pressure gradients (cf. Tsuji and Morikawa, 1975; and Bandyopadhyay and Ahmed, 1993). Table 1.2 is a summary of a few selected publications in this area. Adverse pressure gradient can destroy the logarithmic region and significantly change higher-order velocity moments as reported by Nagano *et al.* (1991), although it is unclear whether or not their turbulent boundary layer was in equilibrium. On the other hand, in cases of equilibrium boundary layers, the validity of the "log-law" was established by White & Tiederman (1990) and Koskie (1991).

In the review article by Narashimha and Sreenivasan (1979), the authors describe the influence of highly accelerated flows on the mean statistics and turbulence structures in the boundary layer, especially its tendency of reversion to laminar flow. They suggest a two-layer model, in which the turbulence in the outer portion of the boundary layer is rapidly distorted and the Reynolds shear stress is nearly frozen. The viscous region exhibits random oscillations in response to the forcing provided by the remainder of the original turbulence. In this situation, reversion is a result of the slowly responding Reynolds stresses to the dominating pressure forces in the outer region, accompanied by the generation of a new laminar sub-boundary layer which is stabilized by the strong acceleration.

In a groundbreaking experiment by Kline *et al.* (1967), the near-wall structure of a turbulent boundary layer with zero, adverse and favorable streamwise pressure gradients was investigated. They identified motions in the viscous sublayer giving rise to "low-speed streaks". These streaks were found to undergo a violent breakup process due to an instability mechanism, resulting in ejections of low-speed fluid from regions very near the wall. This rather complex behavior, known as a turbulent burst, is significant in the production of turbulence energy and its exchange with the outer portions of the boundary layer. Additional details concerning the TBL structure and bursting phenomenon are given by Robinson (1991). While adverse pressure gradients (APG) are known to make bursting more frequent and violent, favorable pressure gradients (FPG) reduce its frequency, and, if sufficiently accelerated ($k \approx 3.5 \cdot 10^{-6}$, where $k = \nu / U_e^2 \cdot dU_e / ds$ is the acceleration parameter, and U_e is the streamwise velocity at the edge of the boundary layer), the bursting process ceases, leading to reverse transition and relaminarization.

In a study by Narayanan and Ramjee (1969) concerning the influence of FPG on reverse transition in a flat plate boundary, mean and fluctuating streamwise velocity profiles, as well as the wall shear stress were measured in a two-dimensional turbulent boundary layer. The breakdown of the "logarithmic law" occurred at a value of the pressure gradient parameter $\Delta_P = \nu / \left(\rho u_\tau^3\right) \cdot dP / ds \approx -0.02$, where ν is the kinematic viscosity and dP / ds is the streamwise pressure gradient. This is associated with thickening of the linear sublayer, which occurs before the relaminarization of the mean velocity profiles and is a first sign for the onset of the reverse transition process. The development of the boundary layer downstream of this point was signified by: (1) increase in the shape factor $H = \delta^* / \theta$, where δ^* is the displacement thickness and θ is the momentum thickness of the turbulent boundary layer, (2) decrease in the skin friction coefficient $c_f = \tau_w / \left(\frac{1}{2} \rho U_\infty^2\right)$, where τ_w is the wall shear stress and U_∞ is the free-stream streamwise velocity; and (3) similarity of the streamwise Reynolds normal stress profiles, $\overline{u^2}$, in the turbulence decay region.

1.2.3 Multiple Strain Rates

The response of a TBL to multiple curvatures (convex and concave) and pressure gradients (favorable and adverse) has been studied by Bandyopadhyay and Ahmed (1993) in an S-shaped duct. The formation of internal layers was detected at the convex curvature junctions. According to a criterion determined by Baskaran *et al.* (1987), an internal layer grows when the curvature parameter $\Delta k^{+} = \Delta R \nu / u_{\tau} > 0.373 \times 10^{-4}$, where $\Delta R = (1/R_2 - 1/R_1)$, R_1 and R_2 being the radii of curvature upstream and downstream of the onset of curvature, respectively. Bandyopadhyay and Ahmed (1993) also found that the effect of curvature dominates the accompanying sequences of streamwise pressure gradients. They reached this conclusion after carefully analyzing the skin-friction distributions on both walls and comparing them to the corresponding applied curvatures and streamwise pressure gradients.

An experimental study by Webster *et al.* (1996) examined a TBL over a surface bump. The initially flat plate, zero pressure gradient TBL was subjected to alternating concave and convex curvature, as well as adverse and favorable pressure gradients. The surface discontinuity near the leading edge of the bump (concave to convex) triggered an internal layer which grew rapidly because of a strong adverse pressure gradient. On the other hand, it was shown that the effect of convex curvature was small. Even though this is one of the few recent experimental studies concerning multiple pressure gradients, the applied strengths of the radial or streamwise pressure gradient was not independently controllable.

The *interaction* of multiple applied strain rates (i.e. in the radial and streamwise direction) in turbulent shear layers is a topic of great interest. Maxey (1982) introduced the concept of an effective strain rate, α_{eff}, and showed that it is possible to write a transport equation for this quantity assuming homogeneous turbulence. Using the analogy with energy decay of homogeneous isotropic turbulence and introducing a large-eddy distortion time scale, $T_D = L / \left(\delta_D \sqrt{\overline{q^2}} \right)$, where L is the integral length scale, δ_D is a constant and $\sqrt{\overline{q^2}}$ is the root-mean square (RMS) of the trace of the Reynolds stress tensor, the following transport equation is obtained:

$$\frac{\partial \alpha_{eff}}{\partial t} = \frac{\partial \overline{U}}{\partial y} + \frac{\partial}{\partial y}\left(E_D \frac{\partial \alpha_{eff}}{\partial y} \right) - \frac{\alpha_{eff}}{T_D} \tag{1.4}$$

This equation includes a diffusion term which accounts for the transport of effective strain by the advection of turbulent eddies, where E_D is the diffusion coefficient. However, this approach is applicable only in the in the case of single imposed strains or distortions, whereas in the case of a complex flow with multiple interacting strains, no formal theory yet exists. In addition, it is not clear how the different rates of application of a newly introduced strain rate affects the momentum transport inside a TBL.

In a more recent approach for combining multiple strain rates, Spalart and Shur (1997) present an equation for the Lagrangian derivative of the direction of the strain-rate tensor principal axes with respect to an inertial reference frame as follows:

$$\frac{D\alpha}{Dt} = \Omega + \frac{1}{2\left(S_{11}^2 + S_{12}^2\right)}\left[S_{11}\frac{DS_{12}}{Dt} - S_{12}\frac{DS_{11}}{Dt} \right] \tag{1.5}$$

where S_{ij} is the strain rate tensor defined with respect to the calculation reference frame, which may be rotating at the rate Ω. The situation for a two-dimensioanl fluid element exposed to strain-rate field is depicted in Figure 1.2 using streamwise coordinates s and n, where $S_{11} = S_{ss}$, $S_{22} = S_{nn}$, and $S_{12} = S_{sn}$, respectively. Since it is the Lagrangian derivative of a quantity which is defined with respect to an inertial frame, $D\alpha/Dt$ is Galilean-invariant, unlike the traditional rate of strain parameter such as $-\overline{U}/r$. This approach is based on the hypothesis that turbulence is enhanced under weak rotation or curvature, if the Reynolds stress principal axes lead the strain rate axes, and vice versa. With this hypothesis, the rotation and curvature effects are unified.

1.3 Engineering Relevance

The flow inside a turbomachine invariably involves multiple pressure gradients. The diverse geometrical features of axial, radial and mixed flow machines bring about the simultaneous action of pressure gradients in different directions in the flowfield. Therefore, such flows have stagnation pressure that are non-uniform both in magnitude and direction.

At the solid walls, boundary layers arise due to viscous effects in the fluid. These boundary layers become subjected to the action of multiple pressure gradients and they may be laminar, transitioning or fully turbulent. The development of the boundary layers in the presence of secondary flows is of significant engineering interest in the design of turbomachinery (cf. Bradshaw, 1975, 1976 and 1997; and Atkins & Smith, 1982). One of the chief problems in the case of turbines is the determination of convective heat transfer between the working fluid and the material surfaces. Therefore, it is of considerable importance to establish a relation between momentum and heat transfer in the complex, three-dimensional boundary layer (i.e. Becker & Rivir, 1979; and Blair, 1983).

1.4 Summary and Objectives

In the reviewed literature on complex turbulent flows, the problem of the response of a turbulent boundary layer to *multiple* strain rates does not appear to have been explored extensively. However, there is a good understanding of how single imposed extra strain rates affect turbulence transport. It is well known that convex curvature immediately reduces the extent of the active shear layer region and hence suppresses the momentum exchange between the inner and outer layer, whereas concave curvature increases radial mixing but it is significantly slower to respond downstream of the onset of curvature than convex curvature. It has also been shown that streamwise pressure gradients influence the turbulence structure.

Despite a number of experimental studies on flows with multiple strain rates, there still is a lack of detailed, near-wall structural information concerning TBLs that experience controlled, multiple pressure gradients. Previous studies have not addressed the fundamental issue of whether or not multiple strain rates *interact* with each other within the turbulent boundary layer. Therefore, the major objective for this study is establish, through experiments and analysis of data, the changes in the flow structure in a flow exposed to multiple pressure gradients, and thereby arrive at a mechanistic model of interactive processes, that is applicable more generally. Subsequently, it becomes necessary to resolve the following issues:

- To determine whether or not the different strain rates interact with each other
- To determine whether the boundary layer reaches a state of similarity
- To determine the response of the turbulent boundary layer immediately upstream

and downstream of the onset of newly introduced strains (radial and streamwise)

- To investigate how different portions of the turbulent boundary layer respond to multiple strain rates
- To determine the response of the turbulence production processes to multiple strain rates
- To investigate the feasibility of a total strain parameter and its relevance to turbulence modeling

Table 1.1 Summary of Curved Turbulent Boundary Layer Studies

Author (Year)	**Flow Geometry**	**Curvature Parameter**	**Measured Quantities**	**Major Conclusions**
Alving et al. (1990)	Flat plate TBL relaxation	Convex curvature, $\delta_o/R \approx 0.08$, 90° bend	Mean and turbulent quantities, power spectra, cross correlations	Different behavior between mean flow and turbulence relaxation process. Turbulence process more complex and longer.
Barlow and Johnston (1988)	TBL with streamwise wall curvature	Moderate concave curvature, $\delta_o/R \approx 0.05$	Mean and turbulent velocity measurements and spectra, flow visualization	Primary effect of concave curvature was shown to amplify large-scale, negatively correlated eddies. Two-stage response of TBL to sudden onset of curvature. Wall-normal velocity are mostly affected due to direct coupling to mean flow
Chiwanga and Ramaprian (1993)	TBL with streamwise wall curvature	Convex curvature, $\delta_o/R \approx 0.05$, 90° bend	Flow visualization using smoke illuminated by laser light sheet	Large-scale structures highly attenuated by convex wall curvature. Curved TBL dominated by smaller scale motions leading to entrainment reduction.
Gibson (1984)	TBL with streamwise wall curvature	Convex curvature, $\delta_o/R \approx 0.008$	Mean flow and turbulence measurements	Reduction in shear stress and turbulence energy accompanied by reductions in turbulent diffusion of Reynolds stress.
Gibson(1988)	TBL with streamwise wall curvature	Convex curvature with different strengths, mild concave curvature	Effect of curvature on law of the wall	Mean velocity and temperature profiles showed greater deviation from log-law distribution for more highly curved flow geometry.

Table 1.1, continued

Author (Year)	**Flow Geometry**	**Curvature Parameter**	**Measured Quantities**	**Major Conclusions**
Gillis and Johnston (1983)	TBL with streamwise wall curvature and recovery	Convex curvature with different strengths, $\delta_o/R \approx$ 0.10 and 0.05	Mean and turbulence measurements	Immediate and significant reduction of the turbulence lengthscales caused by convex curvature. Profiles of inner normalized primary Reynolds shear stress collapse when plotted against y/R showing that the large eddies have been destroyed.
Hoffmann *et al.* (1985)	TBL with streamwise wall curvature	Concave curvature with δ_o/R =0.01 - 0.02	Mean and turbulence measurements including conditional sampling	Results in concave boundary layer heavily depend on vortex structure. For moderate curvature, spanwise variation of surface shear stress and heat transfer rate is sufficiently small
Hunt and Joubert (1979)	Curved high aspect ratio duct	Small streamwise curvature, $R \approx 100$ D	Mean and turbulence measurements, including energy spectra	Need to distinguish between 'shear-dominated' flows for small curvature cases and 'inertia-dominated' flow for highly curved situations. Changes in Reynolds stress components caused by reorientation of turbulent energy components.

Table 1.1, continued

Author (Year)	**Flow Geometry**	**Curvature Parameter**	**Measured Quantities**	**Major Conclusions**
Moser and Moin (1987)	Turbulent curved channel flow	Convex and concave curvature	Direct numerical simulation of channel flow with mild curvature	Remarkable qualitative and quantitative similarities with experimental results. Many turbulence statistics were same on both walls when scaled with the local wall variables. Reynolds shear stress showed the most significant exception as did near-wall skewness and flatness.
Muck *et al.* (1985)	TBL with streamwise wall curvature	Mild convex curvature, $\delta_o/R \approx 0.009$	Mean and turbulence measurements, including higher order moments	Effects of stabilizing and destabilizing curvature on turbulent shear layers are strikingly different. Response of TBL to application or removal of stabilizing (convex) curvature is very rapid as compared to slow response to concave curvature.
Ramaprian and Shivaprasad (1978)	TBLs along curved surfaces	Mild convex and concave surfaces, $\delta_o/R = \pm 0.01$	Measurements of turbulent energy balance, autocorrelations and spectra	Mild curvature has strong various aspects of turbulence structure, i.e. convex curvature suppresses diffusion of turbulent energy away from wall, reduces integral time scales and shifts spectral distribution of turbulent energy and Reynolds shear stress towards higher wave numbers

Table 1.1, continued

Author (Year)	**Flow Geometry**	**Curvature Parameter**	**Measured Quantities**	**Major Conclusions**
Smits *et al.* (1979)	TBL recovery downstream of short curvature regions	Strong convex and concave curvature with 20° and 30° turning angle	Mean and turbulence measurements	Decay of the high turbulent intensity at exit from concave bend is not monotonic. On convex side, flow recovers monotonically (in the main) from low level of turbulent intensity
So and Mellor (1972)	Streamwise curvature, TBL	Strong convex curvature	Mean and turbulence measurements, production terms	Reynolds stress is decreased near the wall and vanishes about midway between the wall and the edge of the boundary layer due to convex curvature. TBL never reached a state of equilibrium.

Table 1.2 Summary of Streamwise Pressure Gradients Studies

Author (Year)	**Flow Geometry**	**Pressure Gradient**	**Measured Quantities**	**Major Conclusions**
Arora *et al.* (1980)	Conical Diffuser	8° total divergence angle	Mean static pressures, turbulence measurements using hot-wires	Dissipation of TKE was generally on the same order as production inside the diffuser
Blackwelder and Kovasznay (1972)	Fully developed TBL subjected to strong FPG	Maximum acceleration parameter, $k \approx 4.8\ 10^{-6}$	Single- and X-wire measurements for mean and turbulence quantities and space-time correlations	Large departure from the logarithmic 'law of the wall' associated with skin-friction reduction and increase of the linear sublayer.
Clauser (1953)	Adverse pressure gradient TBL	Constant Clauser parameter	Pressure measurements, Mean velocity profiles and integral parameters	Velocity profiles were of similar shape when presented in a set of universal constant for an adverse pressure gradient flow.
Durbin and Belcher (1992)	TBL with strong adverse pressure gradients	Kinematic pressure gradient and pressure gradient velocity	Asymptotic analysis in the context of eddy viscosity closure modeling	Boundary layer devided into three regions: the wall layer, wake layer and a transition layer. Two key differences from ZPG: wall layer not exponentially thinner than the wake, and wake has large velocity deficit
Evans (1985)	Suction surface of compressor blade	Constant APG over most of suction surface	Mean velocity profiles affected by freestream turbulence	Coles profile for TBLs is valid for APG boundary layer. Turbulence intensity affects the outer layer velocity defect profiles

Table 1.2, continued

Author (Year)	**Flow Geometry**	**Pressure Gradient**	**Measured Quantities**	**Major Conclusions**
Kline *et al.* (1967)	Flat plate TBL	APG and FPG, $-2.00 \times 10^{-6} \leq k \leq 3.85 \times 10^{-6}$	Mean and turbulence velocity measurements, visual studies using hydrogen bubble technique	Presence of well-organized spatially and temporally dependent motions in 'linear sublayer', leading to low-speed streaks in the near-wall region. Interaction with outer flow portions eventually leads to bursting, playing a dominant role in production process.
Lian (1990)	TBL with strong adverse pressure gradient	APG strong enough to cause small regions of reverse flow	Flow structures using hydrogen bubble techniques and flow mean velocities	Long streaks along low-speed / high -speed interface are continually stretching. Streamwise vortices were also observed along these interfaces. Spanwise vortices were observed at front of high-speed regions
Nagano *et al.* (1991)	TBL with adverse pressure gradient	Clauser pressure gradient parameter β increasing from 0.8 to 4.7	Mean and turbulence velocity measurements including triple products	Mean flow and turbulence statistics were seriously affected by increasing APG. The 'law-of-the-wall' does not hold. Drastic structural changes were observed, especially in the higher-order velocity moments

Table 1.2, continued

Author (Year)	**Flow Geometry**	**Pressure Gradient**	**Measured Quantities**	**Major Conclusions**
Narashimha and Sreenivasan (1973)	Analytical investigation of highly accelerated TBLs	Pressure gradient parameter, scaled on characteristic Reynolds stress gradient	N/A	Wall parameters suggest presence of a small reverse-transitional region. In inner layer, velocity fluctuations decay in streamwise direction according inverse power-law. In outer layer, there is evidence of rapid distortion of turbulence.
Samuel and Joubert (1974)	TBL with increasingly adverse pressure gradient	Pressure coefficient, c_p, as well as the first and second streamwise derivative	Mean and turbulence measurements as well as streamwise velocity spectra	Comparisons between measurements and existing boundary layer models indicated that 'law-of-the-wall' is all-embracing model for TBL development.
Schofield (1981)	Analysis of equilibrium TBL with moderate to strong APGs	Revised Clauser pressure gradient parameter	N/A	Predicted shear stress profiles using Schofield-Perry law (1972) show good agreement with experimental data. Method to predict smoothly changing APG boundary layer is outlined and demonstrated
Smits *et al.* (1983)	Low-Reynolds number TBL with zero and favorable PGrads	Pressure coefficient, c_p, and Clauser's PGrad parameter, β, varying between 0.0 and -0.20	Pressure and mean velocity measurements	Skin-friction behavior well fitted by simple power-law relationship in both zero and favorable pressure gradient flow

Table 1.2, continued

Author (Year)	**Flow Geometry**	**Pressure Gradient**	**Measured Quantities**	**Major Conclusions**
Tsuji and Morikawa (1975)	TBL with alternating pressure gradients	Acceleration parameter, k, varying between -0.80 and 1.28 x 10^{-6}	Mean and turbulence measurements	Internal layer developed in APG region downstream of strong FPG region, destroying log-law.

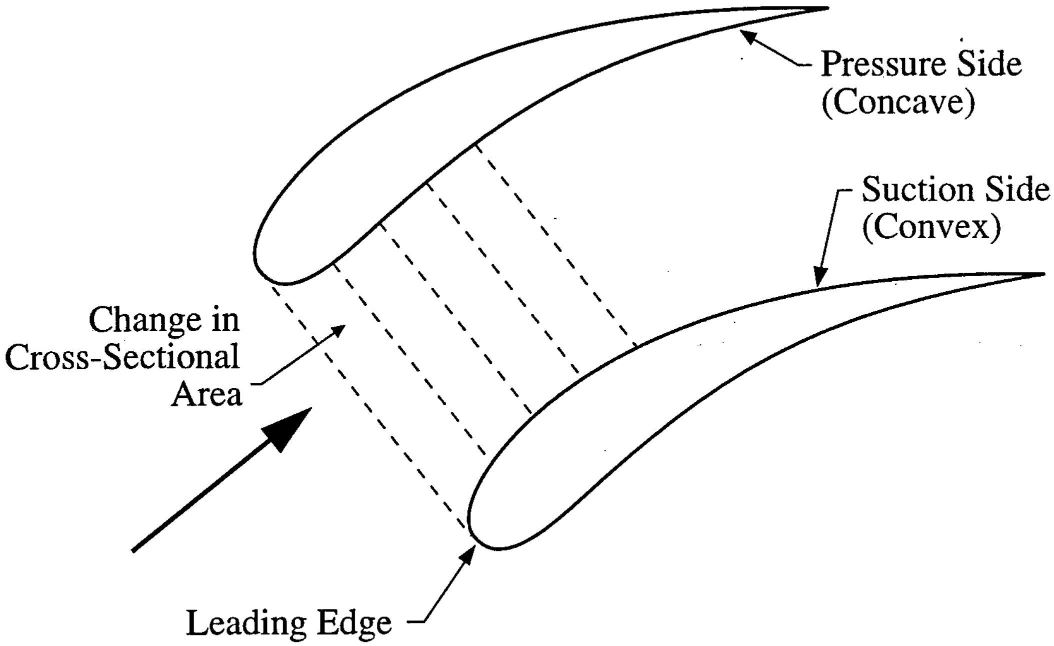

Figure 1.1 Schematic of typical flow passage in turbomachinery

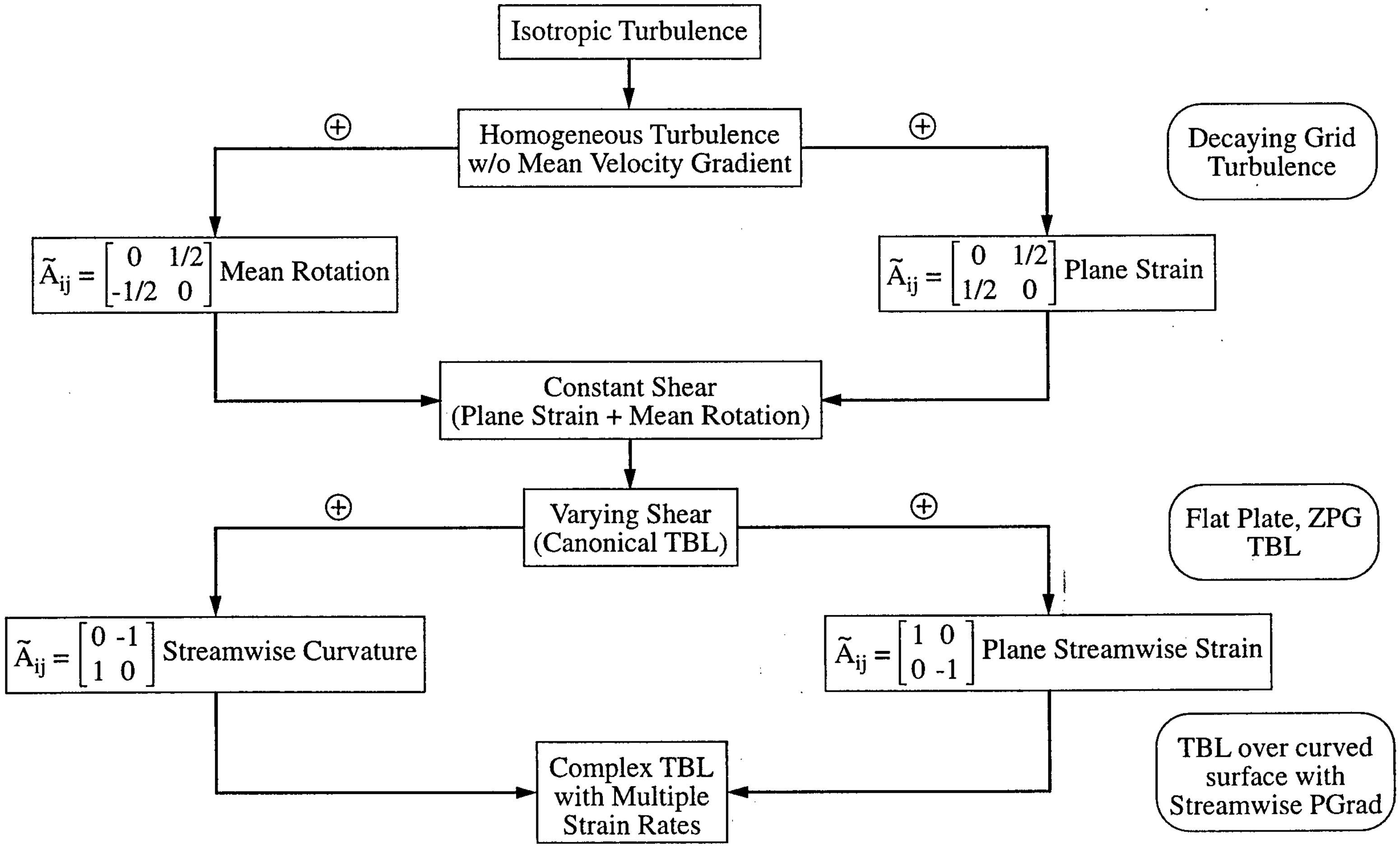

Figure 1.2 Overview of hierarchy of turbulent flows

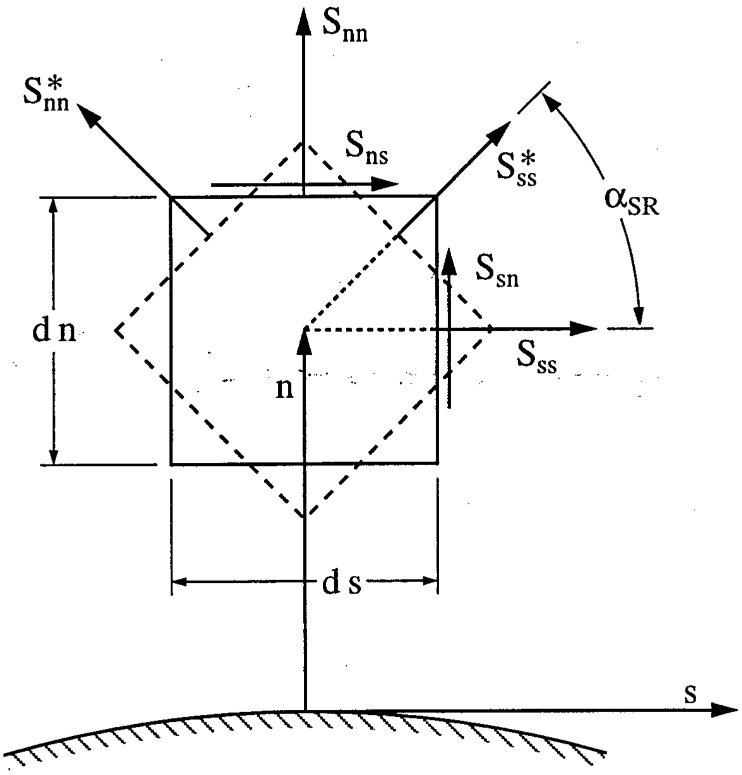

Figure 1.3 Two-dimensional fluid element showing components of strain rate tensor

CHAPTER 2. EXPERIMENTAL APPARATUS AND PROCEDURES

2.1 Water Channel

The experiments were performed in the Purdue multiple strain rate facility, a recirculating water channel (shown schematically in Figure 2.1) driven by four centrifugal pumps each rated at $5.7 \times 10^{-3}\ \mathrm{m}^3/\mathrm{s}$ (90 gpm). Two interchangeable curved test sections were employed to impose moderate and strong convex curvature. Softened and filtered water entered the straight development section through a series of screens, into a smooth two-dimensional contraction section followed by a honeycomb section to reduce large-scale vortical motions in the entrance region. An equilibrium turbulent boundary layer developed on the smooth wall of the straight upstream section (2.46 m long for test section 1 and 1.95 m long for test section 2). The spanwise dimension of all test sections was 200 mm (z-direction) and their width (y-direction) was 100 mm at the boundary layer trip and approximately 110 mm at the entrance into the curved test section, s=0.

A flexible wall (constructed from 3.2 mm thick Lexan®) was placed between the measurement wall and opposite side wall to adjust the cross-sectional area, and hence to impose the streamwise pressure gradient. The primary geometric parameters for both test sections are shown in Figure 2.2. The flexible wall was adjusted to yield a zero pressure gradient (ZPG) in the straight section and a zero, adverse (APG) or favorable pressure gradients (FPG) of different strengths in the curved test section. The width of the test section downstream of the onset of curvature was different for each streamwise pressure gradient. The exact wall shapes were measured and recorded. Figure 2.3 schematically illustrates the shapes of the flexible wall used to establish the desired streamwise pressure gradient conditions.

As shown in chapter 1, a streamwise change in the wall-normal pressure gradient induces a streamwise pressure gradient due to the discontinuity in the radius of curvature. By increasing the cross-sectional area upstream of the straight curvature junction, this effect was counteracted to minimize the influence of the locally strong FPG.

For test section 1 (TS1), the boundary layer thickness at the exit of the upstream straight section was $\delta_0 \approx 40$ mm, resulting in a curvature parameter of $\delta_0/R \approx 0.10$, which comprises a strong curvature. For test section 2 (TS2), the initial boundary layer thickness was $\delta_0 \approx 35$ mm, which resulted in a curvature parameter of $\delta_0/R \approx 0.05$

(moderate curvature). Typical values of the curvature parameter Δk^+ for each test section were: $\Delta k^+ = 6.20\text{x}10^{-5}$ for TS1 and $\Delta k^+ = 3.54\text{x}10^{-5}$ TS2, using inner variables evaluated just upstream of the onset of curvature under ZPG conditions.

2.2 Measurements Techniques

2.2.1 Pressure Gradient

Pressure taps installed along the convex wall were used to measure the imposed streamwise pressure gradients with a Gilmont® micro-manometer. The manometer working fluid was carbon-tetra-chloride (CCl_4 with S.G. = 1.584) which results in a sensitivity of ±1 Pa. The pressure tap spacing was varied between 25.4 mm (near the onset of curvature) and 101.6 mm further downstream in the curved test sections. The exact locations of all pressure taps are listed in Tables 2.1 and 2.2.

2.2.2 Two-component LDV

A two-component laser-Doppler velocimeter (LDV) system was employed for simultaneous measurements of the streamwise and wall-normal instantaneous velocity. The transmitting optics of the two-component, three beam LDV system consisted of a Thermo System Incorporated (TSI®) model 9100-8 velocimeter modified to measure velocity components at ±45° to the mean flow direction in TS1. A different configuration was used for the velocity measurements in TS2, where the three-beam system was oriented to directly measure streamwise and wall-normal velocity components. Using a pair of Bragg cells, both monochromatic beams were frequency shifted at 40 MHz to minimize fringe biasing.

The transmitting and receiving optics are shown schematically in Figure 2.4. Operating in the forward scattering mode, near-wall measurements were made possible by inclining the optical axis of the transmitting side by approximately 3° with respect to the measurement wall. The transmitting lens, transmitting mirror and the entire receiving optical train were mounted as one assembly which translated in the direction normal to the measurement wall (y-direction). A Mitotoyo dial gage model 3058-11 with a resolution of ±0.01 mm was used to measure the probe volume translation. The location of the wall was approximated to within three viscous units by visually observing the crossing of the transmitting beam on the measurement wall. This position was corrected in the post-processing stage using the inferred wall shear velocity from the Clauser method and an explicit equation for the law of the wall given by Liakopolous (1984). This correction was usually less than two viscous units.

The probe volume was 45 μm in diameter and had a spanwise extent of approximately 920 μm, which corresponded to 2 and 40 viscous units, respectively, when normalized with inner variables, u_τ and ν. In order to enhance the spatial coincidence of the two probe volumes, a 50 μm pinhole was inserted into the receiving optics, which reduced the effective probe volume length to 12 viscous units. The relative position of the probe volume with respect to the measurement wall was first approximated by observing the beam crossing and its reflection from the wall through the receiving optics eyepiece. Using this method usually placed the probe volume within half probe volume diameter (one viscous unit) relative to the wall (y = 0.0 mm). An explicit relationship for the mean streamwise velocity component, $U^+ = f(y^+)$, suggested by Liakopolous (1984) which represents the near-wall behavior throughout the logarithmic region very well was used for a final wall correction. Spatial and temporal measurement coincidence were achieved by carefully aligning the transmitted beams and the receiving optics, and by setting a coincidence window on the counter processors (TSI 1980B) to ensure that the accepted signal on both channels originated from the same scattering particle passing through the probe volume. The flow was seeded with 0.3 μm diameter fat particles from homogenized cream at a concentration of approximately 2.5 $\mathrm{ml/m^3}$.

In order to calculate reliable statistics (mean and higher order moments), various numbers of statistically independent velocity realizations were required. For the two-component velocity profiles, a minimum of 10,000 realizations were acquired for each velocity component. Figure 2.5 depicts a block diagram of the data acquisition system used for the coincident two-component LDV data. The downmixed, high-pass filtered Doppler signal entered a pair of TSI 1984 input conditioners, where typical signal-to-noise ratios (SNR) were estimated using an oscilloscope. A temporal coincidence window estimated from a typical particle transit time through the probe volume (e.g. 40 μs) was set on the

1998A TSI master interface, which controlled the combined data transfer of both velocity words to the MassComp© 5520 computer via an TSI interface.

Velocity bias occurs in LDV measurements of a highly turbulent flow, due to the fact that the probability of measuring a high velocity particle is higher than that of measuring a low velocity particle (McLaughlin and Tiederman, 1973). This effect results in significant measurement error, especially near the wall, where the turbulence intensities are highest. Velocity bias was minimized using the fixed-waiting-time sampling method. In this method the data acquisition system is inhibited for a fixed amount of time between two subsequent realizations. The Kolmogorov time scale is representative of the smallest (dissipation) scale of the flow. For the flow studied here, the Kolmogorov time scale was estimated by assuming that dissipation of turbulence kinetic energy (TKE) was equal to production at the production peak (at $y^+ \approx 10$). The data validation rate was maintained (about five times) in excess of the greatest estimated Kolmogorov frequency of the flow and the inhibit time was more than ten times the inverse of the validation rate.

The time-resolved measurements, necessary for bursting period analysis, consisted of 100,000 velocity realizations with the counter processors operating in the single-point per Doppler-burst mode. In this case, velocity bias was reduced by correcting the individual velocity measurements using a two-dimensional weighting factor as suggested by McLaughlin and Tiederman (1973). During these measurements, the particle arrival rate was maintained in excess of the wall strain rate, which is an approximation for the viscous frequency of the flow, $f_{vis} = \partial\overline{U}/\partial y|_w = u_\tau^2/\nu$, which for TS1 was typically 1800 Hz for the zero, between 2400 & 2800 Hz for the favorable, and between 2700 & 650 Hz for the adverse streamwise pressure gradient cases. Note that for the APG case, convex curvature and streamwise pressure gradient have opposite effects in terms of stabilizing or destabilizing the flow, thus a wide range of wall strain rates results. For TS2, the typical values for the viscous frequency were 1600 Hz for ZPG, and 2900 Hz for the strong FPG case.

2.3 Data Reduction

2.3.1 Velocity Statistics

The calculation of the velocity statistics required special attention using the following procedure. First, the individual velocity realizations measured on each channel, U_1' and U_2' were calculated. Due to a slight error of the relative beam pair alignment, each U_1', U_2' pair was transformed into precisely orthogonal velocity components U_1 and U_2 using the following:

$$U_1 = U_1' \tag{2.3}$$

$$U_2 = \frac{1}{\sin\alpha} U_2' - \frac{1}{\tan\alpha} U_1' \tag{2.4}$$

In Equation 2.4, α is the angle between the measured velocity components as shown in Figure 2.6.

The velocity statistics were first determined for the U_1 and U_2 velocities and then transformed to the laboratory coordinate system (streamwise and wall-normal direction) according to the following procedure. For any angle θ, calculated from the beam configuration, the streamwise and normal velocity components were determined from:

$$U = U_2 \cos\theta + U_1 \sin\theta \tag{2.5}$$

$$V = U_2 \sin\theta - U_1 \cos\theta \tag{2.6}$$

These equations were substituted into the definitions of the Reynolds averaged statistics ($U_i = \overline{U}_i + u_i$), which yielded the equations for the Reynolds normal and shear stress components as:

$$\overline{u^2} = \overline{u_1{}^2} \sin^2\theta + \overline{u_2{}^2} \cos^2\theta + 2\overline{u_1 u_2} \sin\theta\cos\theta \tag{2.7}$$

$$\overline{v^2} = \overline{u_1{}^2} \cos^2\theta + \overline{u_2{}^2} \sin^2\theta - 2\overline{u_1 u_2} \sin\theta\cos\theta \tag{2.8}$$

$$\overline{uv} = \left(\overline{u_2{}^2} - \overline{u_1{}^2}\right) \sin\theta\cos\theta + \overline{u_1 u_2}\left(\sin^2\theta - \cos^2\theta\right) \tag{2.9}$$

Similarly, higher order moments (skewness, flatness and other triple products) were calculated from the two-component LDV data. These equations are given in section 2.3.3.

2.3.2 Burst Detection

The structure of turbulence in boundary layers has been studied extensively (Robinson, 1991, see Figure 2.7). One of the events associated with coherent structures is an ejection, or series of ejections comprising a turbulent burst. The bursting cycle is the main turbulence production mechanism (Runstadler *et al.*, 1963). During an ejection event, the low-speed fluid near the wall undergoes a rapid acceleration away from the wall and mixes with the higher-speed fluid above the wall. Consequently, the ejection process is associated with a positive v-fluctuation (higher than the mean) and a negative u-fluctuation (lower than the mean). These characteristics led Lu and Willmarth (1973) to propose the second quadrant (uv_2) burst detection technique for an Eulerian velocity probe. This detector triggers on large negative values of the instantaneous product of the streamwise and wall-normal velocity fluctuations when they occur in the second quadrant of the uv-plane, i.e.

$$uv(t) < -H \cdot u'v' \text{ and } u(t) < 0 \text{ or } v(t) > 0, \tag{2.10}$$

where H is a threshold specified by the user. The fact that a threshold independent range exists allows meaningful estimates of the mean time between bursts to be made. This detection method was chosen over single-component burst detection methods, e.g. the VITA (Blackwelder and Kaplan, 1976) and modified u-level (Bogard and Tiederman, 1986) techniques, because the uv_2 method gives the best correlation between probe detections and visually observed ejections (Bogard, 1982).

It was also necessary to group multiple ejections appropriately, depending on whether they originated from the same or from different bursts, through the use of a grouping time, τ_g. This grouping procedure was developed by Bogard and Tiederman (1986) and has also been used by other investigators (e.g. Barlow and Johnston, 1988b; and Schwarz and Plesniak, 1996a). Ideally, a histogram of the time between ejections would have two separate distributions; one for ejections from the same burst and one for ejections from different bursts. In practice, there is some overlap between the two distributions. Ejections separated by τ less than τ_g are assumed to originate from the same burst, while those with longer separation times originate from different bursts. The appropriate grouping time for a given threshold can be determined using the histogram of the time between ejections plotted on a semi-logarithmic scale (see Figure 2.8). It is assumed that the distribution of times between ejections within the same burst and the time between detections from different bursts both decrease exponentially, yielding two linear regions with a region in between where the distributions overlap (not necessarily linear). The extrema of the overlap region are indicated by τ_1 and τ_2 and the grouping time was chosen at the midpoint of the overlap region (White and Tiederman, 1990). Thus, the ambiguity in τ_g is half of the interval between τ_1 and τ_2. The propagation of this ambiguity is the major contributor to the uncertainty in the mean burst period $\overline{T_B}$. This grouping procedure was repeated for ten different thresholds between 0.0 and 1.6 for each burst record. In Figure 2.9, the burst period is plotted as function of the detector threshold (H), and the threshold independent region is clearly evident. The reported time between bursts ($\overline{T_B}$) is calculated by simply averaging the values within the threshold independent range.

2.3.3 Higher-order Moments and Deduced Quantities

Higher order velocity moments were calculated to further analyze the turbulence data. The skewness and flatness (kurtosis) of the streamwise and wall-normal velocity components are defined as $u_{i,\mathrm{skew}} = \overline{u_i^3}/{u_i'}^3$ and $u_{i,\mathrm{flat}} = \overline{u_i^4}/{u_i'}^4$, respectively. The resulting equations for these third and forth order moments in the laboratory coordinate system that were derived from the rotated reference frame are:

$$\overline{u^3} = \overline{u_2^3}\cos^3\theta + 3\overline{u_1u_2^2}\sin\theta\cos^2\theta + 3\overline{u_1^2u_2}\sin^2\theta\cos\theta + \overline{u_1^3}\cos^3\theta \qquad (2.11)$$

$$\overline{v^3} = \overline{u_2^3}\sin^3\theta - 3\overline{u_1u_2^2}\sin^2\theta\cos\theta + 3\overline{u_1^2u_2}\sin\theta\cos^2\theta - \overline{u_1^3}\cos^3\theta \qquad (2.12)$$

$$\begin{aligned}\overline{u^4} = {} & \overline{u_2^4}\cos^4\theta + 4\overline{u_1u_2^3}\sin\theta\cos^3\theta + 6\overline{u_1^2u_2^2}\sin^2\theta\cos^2\theta \\ & + 4\overline{u_1^3u_2}\sin^3\theta\cos\theta + \overline{u_1^4}\sin^4\theta\end{aligned} \qquad (2.13)$$

$$\overline{v^4} = \overline{u_2{}^4}\sin^4\theta - 4\overline{u_1{}^3u_2}\sin\theta\cos^3\theta + 6\overline{u_1{}^2u_2{}^2}\sin^2\theta\cos^2\theta - 4\overline{u_1u_2{}^3}\sin^3\theta\cos\theta + \overline{u_1{}^4}\cos^4\theta \tag{2.14}$$

2.4 Uncertainty Estimates

The error analysis of the LDV data followed that recommended by Walker & Tiederman (1988) and Yanta and Smith (1973). The uncertainty in the estimate for statistical quantities depends on both the ensemble size and the RMS level for a mean quantity but it depends solely on the ensemble size for an RMS quantity. A 95% confidence interval for Gaussian (or nearly Gaussian) distributions was assumed (Kline & McClintock, 1953; and Moffat, 1988). The spatial absolute uncertainties were ±1 mm in the streamwise (s) and ±0.02 mm in the wall-normal (y) direction.

Typical uncertainty bounds for the Reynolds stresses are shown in the upper right corner of the appropriate figures. Typical uncertainties on the RMS and mean velocities are on the order of the plot symbol sizes, i.e. less than 1%, except for the near-wall region ($y^+ \leq 10$, where $y^+ = yu_\tau/\nu$ is the inner normalized wall-normal coordinate). For $y^+ \leq 10$, the measured wall-normal RMS velocity component was significantly higher than several benchmarks, e.g. the direct numerical simulation data by Spalart (1988), and hence is omitted. The maximum uncertainty on the shear stress was typically 12 to 13% (for N = 10,000) in the maximum stress region ($y^+ \approx 40-80$). Typical values for the relative uncertainties for the mean and RMS velocity components and for the primary Reynolds shear stress are listed in Table 2.3 for N = 20,000 at $y^+ \approx 10$ and 100.

Uncertainty in the shear velocity is less than 1% due to the mean streamwise velocity measurements and approximately 5% due to the additional uncertainty introduced by the Clauser method, which has been used to infer the wall shear stress. Note that for flows with curvature and pressure gradient, the constants in the log-law may be different than the universal flat plate values (Gibson, 1988; and Moser and Moin, 1987). The uncertainty for the pressure gradient parameter is of the same order as the size of the corresponding plotting symbols (1.6% for k).

The uncertainties associated with measuring quantities upon which the burst periods depend are on the order of 1 to 2%. However, due to the post-processing operations, i.e. choice of thresholds, and determining grouping times to discriminate between ejections originating from the same or different bursts, the ambiguity in the absolute value of $\overline{T}_B$ is typically between 15 and 20%. Thus, while the absolute magnitudes of burst period are uncertain up to 20%, all of the data sets were processed consistently to minimize the ambiguity and the trends exhibited are faithful to within the measurement uncertainty of 2%. The normalized ejection duration $\Delta\tau_E^+ = \Delta\tau_E u_\tau^2 / \nu$ was calculated from the individual time-resolved measurements for each threshold and its uncertainty is approximately 3.5%.

Table 2.1 Location of pressure taps for test section with strong curvature ($\delta_o / R \approx 0.10$)

Tap Number	$s - s_o$ [mm]	α [°]
1	-121	straight
2	-90	straight
3	-59	straight
4	-28	straight
5	20	2.9
6	45	6.5
7	70	10.0
8	95	13.6
9	120	17.2
10	150	21.5
11	200	28.7
12	225	32.2
13	250	35.8
14	275	39.4
15	300	43.0
16	350	50.1
17	375	53.7
18	400	57.3
19	450	64.5
20	500	71.6

Table 2.2 Location of pressure taps for test section with moderate curvature ($\delta_o / R \approx 0.05$)

Tap Number	$s - s_o$ [mm]	α [°]
1	-254	straight
2	-203	straight
3	-165	straight
4	-140	straight
5	-108	straight
6	-7	straight
7	18	1.5
8	44	3.6
9	69	5.6
10	94	7.7
11	120	9.8
12	145	11.9
13	171	14.0
14	221	18.1
15	272	22.3
16	323	16.4
17	374	30.6
18	425	34.8
19	475	38.9
20	577	47.2
21	679	55.5
22	780	63.9
23	882	72.2
24	983	80.5

Table 2.3 Summary of measurement uncertainties for 95% confidence interval

	$y^+ \approx 10$	$y^+ \approx 100$
$\sigma_{\overline{U}}$	± 0.45 %	± 0.41 %
$\sigma_{\overline{V}}$	± 0.40 %	± 0.40 %
$\sigma_{u'}$	± 0.68 %	± 0.68 %
$\sigma_{v'}$	± 0.83 %	± 0.56 %
$\sigma_{\overline{uv}}$	± 7.15 %	± 5.26 %

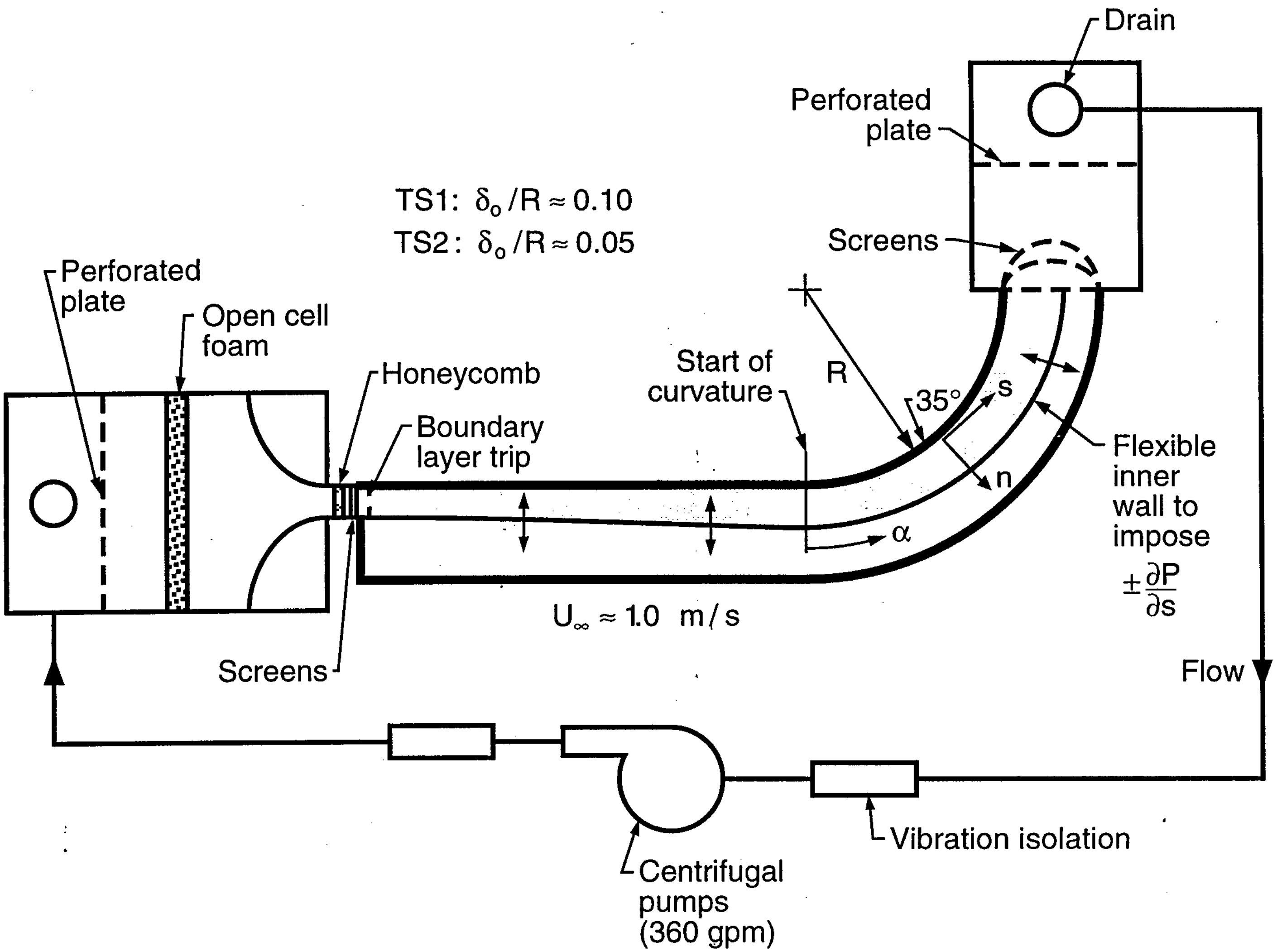

Figure 2.1 Schematic of low-speed water tunnel

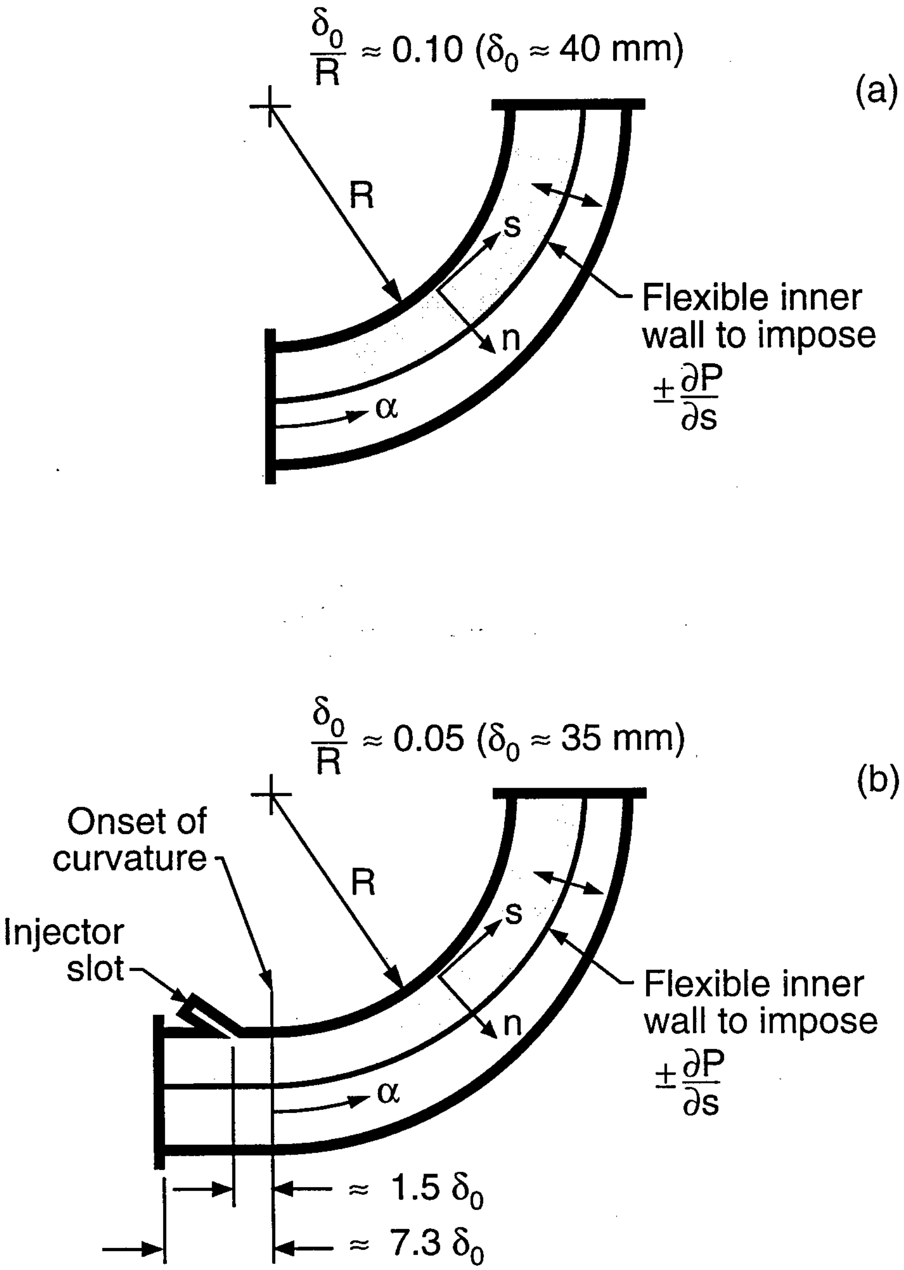

Figure 2.2 Details of curved test section with (a) strong and (b) moderate curvature

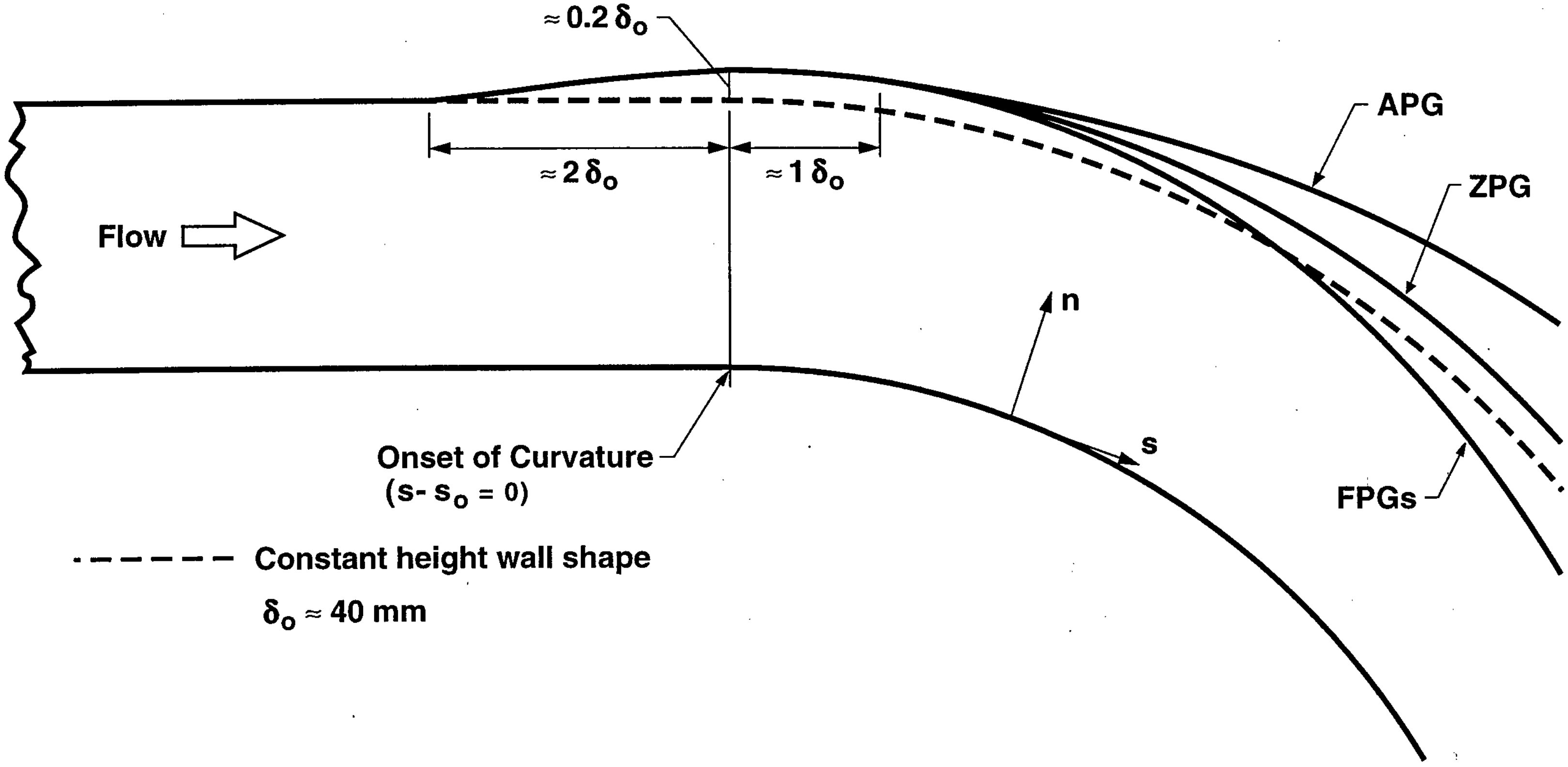

Figure 2.3 Schematic of wall shapes used to achieve various pressure gradients

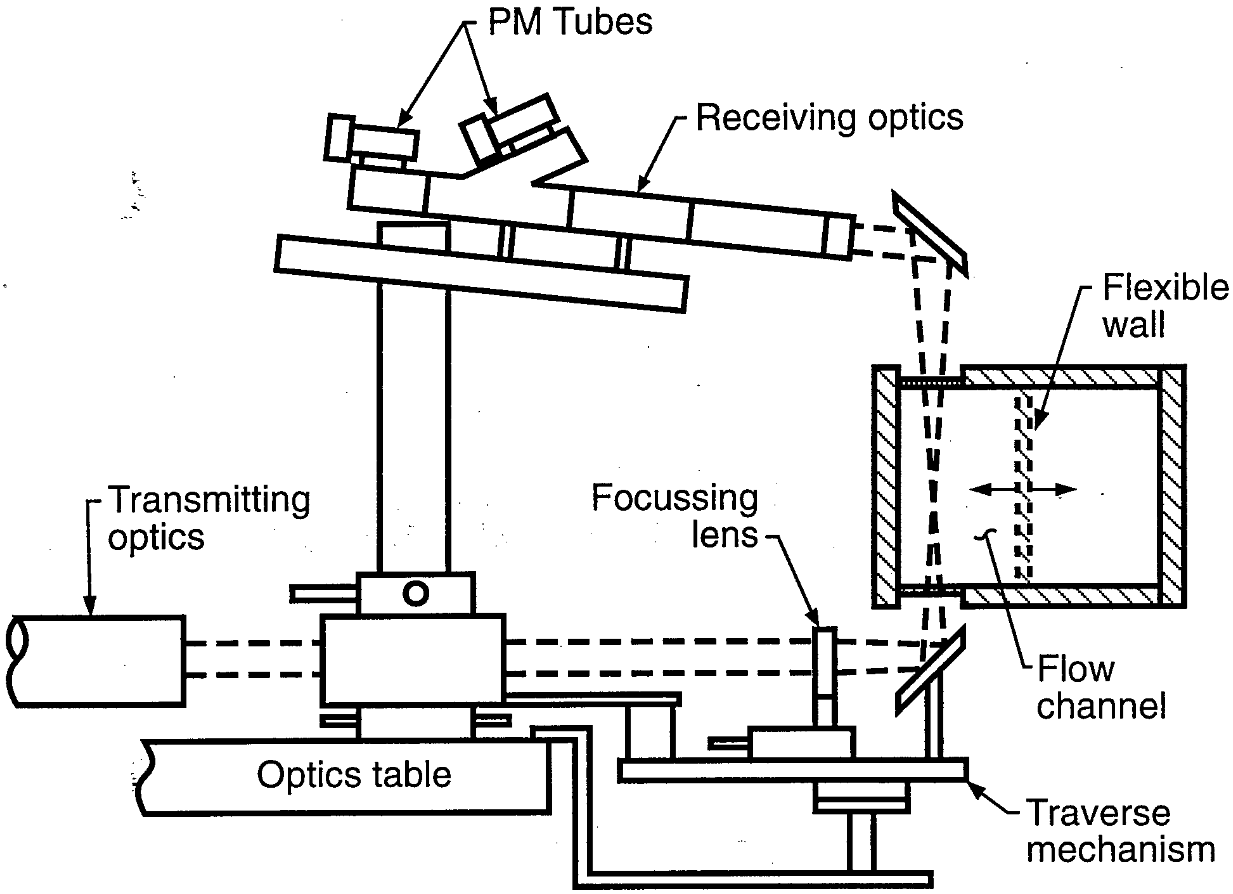

$d_m \approx 45 \times 10^{-6}$ m

$\ell_m \approx 900 \times 10^{-6}$ m

Figure 2.4 Schematic of LDV transmitting and receiving optics

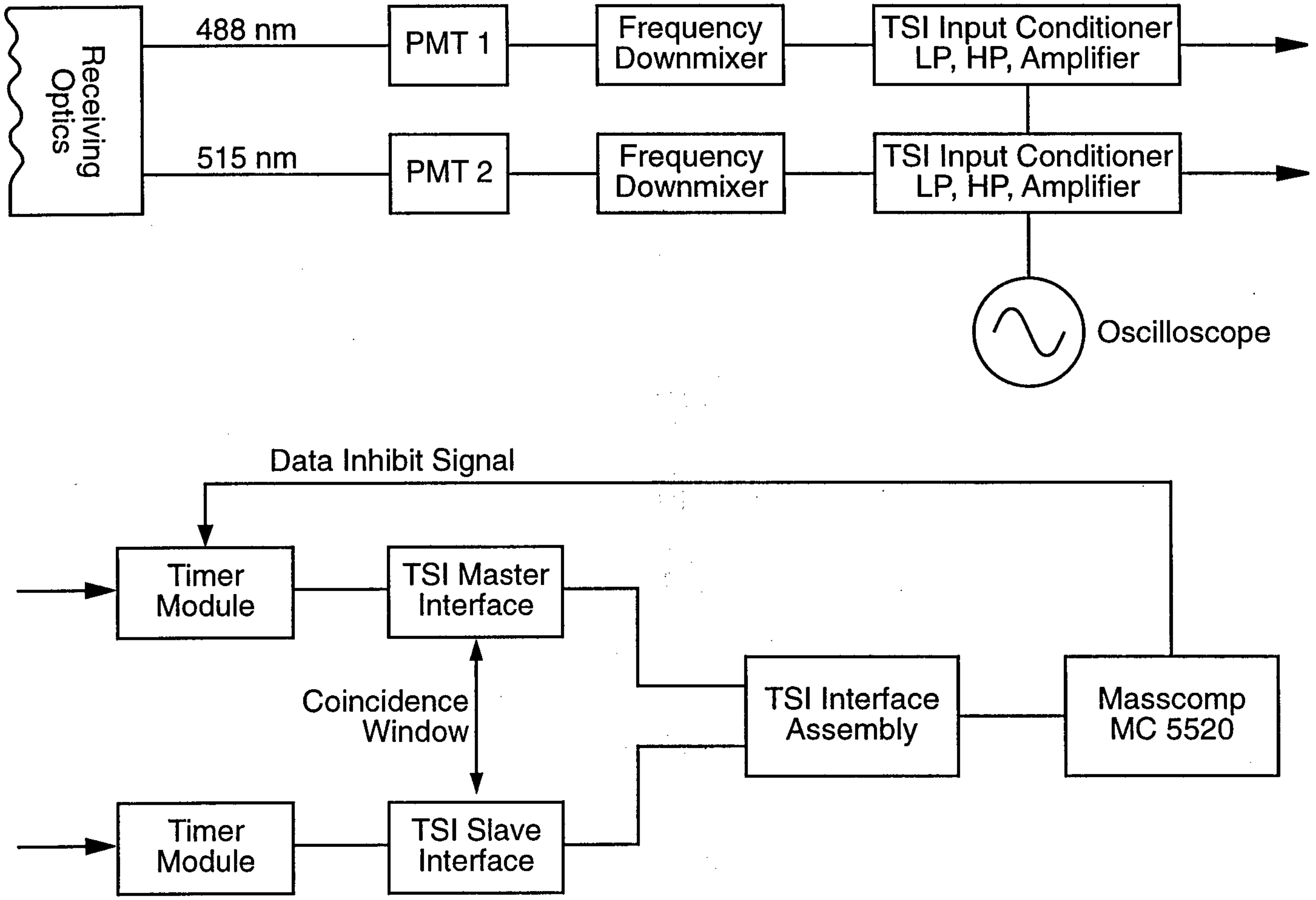

Figure 2.5 Schematic of data acquisition system

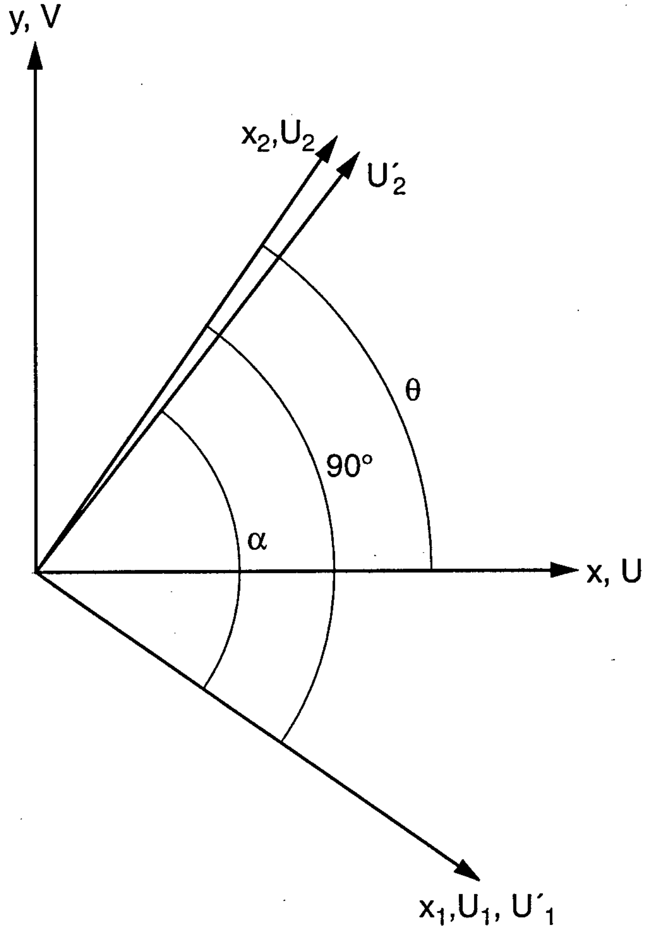

Figure 2.6 Schematic of coordinate rotation and correction for non-orthogonality of velocity components

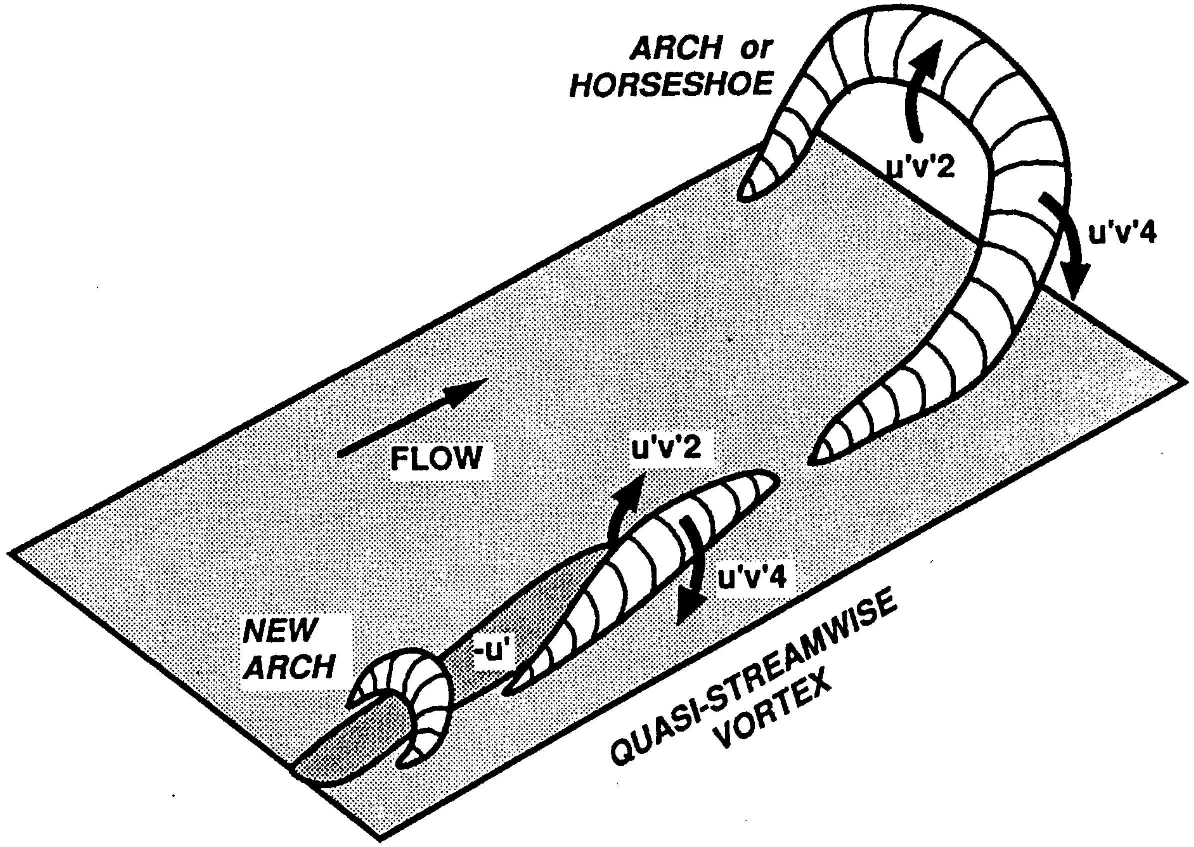

Figure 2.7 Sketch of Reynolds stress producing vortical structures (Robinson, 1991)

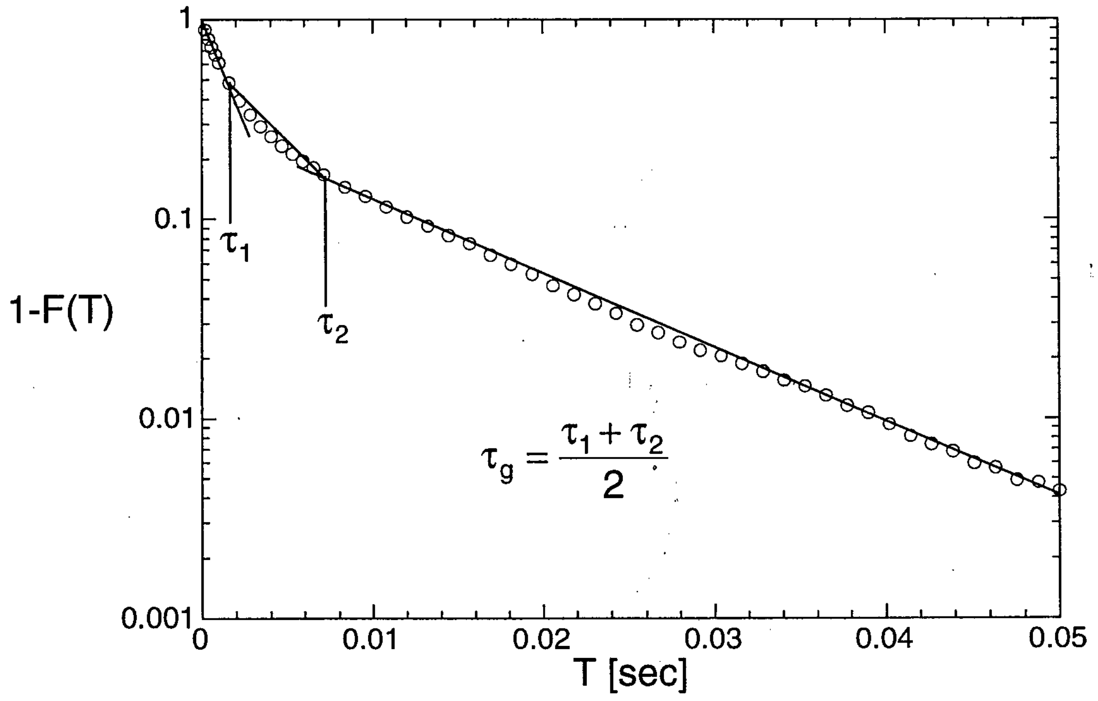

Figure 2.8 Histogram of time between ejections to determine the grouping time

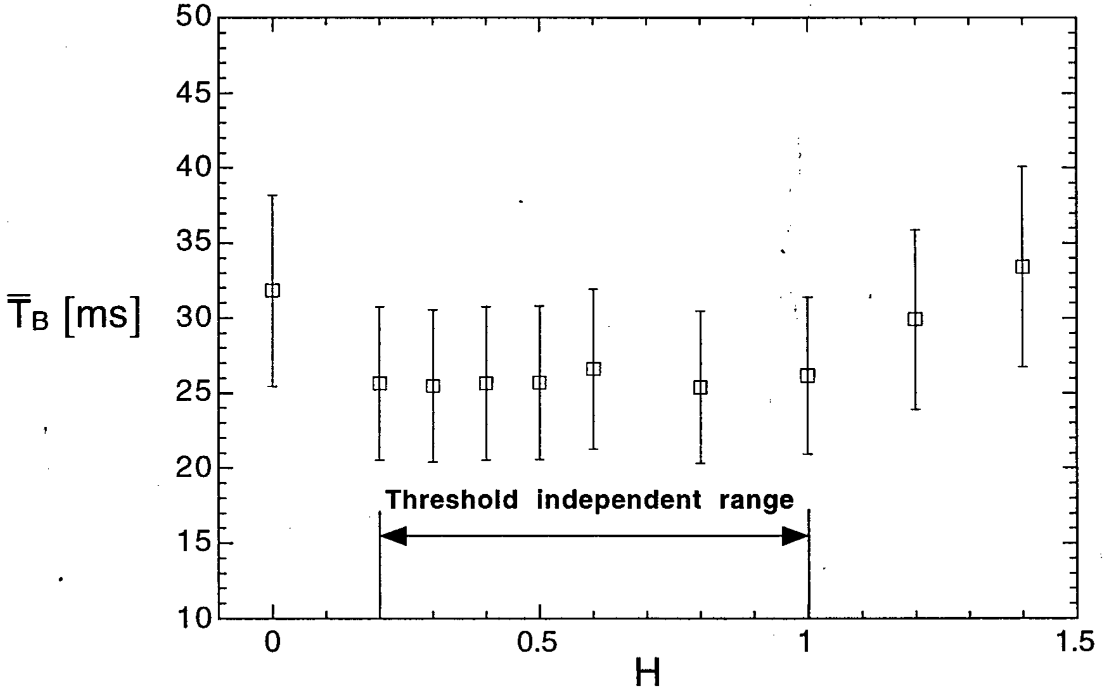

Figure 2.9 Time between bursts as a function of detector threshold

CHAPTER 3. RESULTS

Streamwise and wall-normal profiles of mean and turbulence quantities in boundary layers with multiple strain rates are presented in this chapter. First, the integral parameters dP/ds, k, c_f, and θ are shown under various combinations of strain rates. Next, profiles of inner normalized mean streamwise velocity are presented. Finally, turbulent normal stresses and the primary Reynolds shear stress are shown under the different experimental conditions. The cases investigated are summarized in Table 3.1. Typical ranges for the acceleration parameter k, the momentum thickness Reynolds number Re_θ, and the pressure gradient ratio $P_{rat} = \frac{|dP/ds|}{dP/dr}$ are: $-0.5 \cdot 10^{-6} \leq k \leq 1.8 \cdot 10^{-6}$, $3{,}500 \leq Re_\theta \leq 10{,}500$, and $0 \leq P_{rat} \leq 1.2$, respectively. All data sets presented here are compared to a ZPG boundary layer that formed over a smooth flat wall with $Re_\theta \approx 3250$ and also with the DNS results of Spalart (1988). Note that in the curved portion of the boundary layer, the reference free-stream velocity is replaced by the potential velocity at the wall, U_{pw}.

3.1 Pressure Gradients and Integral Parameters

In this investigation it was necessary to establish zero, as well as constant favorable and adverse pressure gradients of different magnitudes downstream of the onset of curvature. In Figure 3.1, the streamwise pressure gradient distribution is shown for both test sections; test section 1 (TS1) with $\delta_o/R \approx 0.10$ (Figure 3.1a) and test section 2 (TS2) with $\delta_o/R \approx 0.05$ (Figure3.1b). Nearly constant levels of pressure gradient were achieved over a significant portion of the convex wall for both test sections, except in the region immediately downstream of the onset of curvature, where a favorable pressure gradient prevailed for a short distance. As discussed in chapter 1, this pressure gradient arises from the discontinuity in wall curvature. To counteract this effect in the initial region of the curved test section, the flexible wall opposite to the measurement wall was carefully contoured. This led to a compensation of the pressure gradient immediately upstream and downstream of the onset of curvature. In the following chapter, details of the different shapes of the flexible wall, and the resulting pressure gradients, are discussed further, especially with respect to the combined effects of streamwise and wall-normal pressure gradients. The streamwise distribution of the local acceleration parameter, $k = \nu / U_e^2 \cdot dU_e / ds$, shown in Figure 3.2, exhibits the same trends (with opposite sign) as the pressure gradient. This parameter is a good indicator of how strongly the turbulence structure is affected, especially in regard to reverse transistion (relaminarization). It is well knownthat high levels of acceleration can result in boundary layer relaminarization (cf. Kline *et al.*, 1967; Sreenivasan, 1979).

The distribution of the local skin-friction coefficient in each test section is shown in Figure 3.3. Included are some of the upstream, flat-plate data which were acquired in the same facility by Koskie (1990) as well as computational results that were obtained from a finite difference boundary layer code (CBTSL by Cebeci and Bradshaw, 1977), which solves the thin-shear layer, partial differential equations. Despite the positive shift near the onset of curvature for both test sections (due to the locally strong FPG), the skin-friction coefficient is reduced over the convex wall in the presence of zero pressure gradient (ZPG) in both test sections. The degree of reduction is greater for the stronger curvature, since stronger convex curvature causes increased stabilization of the turbulent boundary layer (Gillis and Johnston, 1983). On the other hand, FPGs counteract the reduction caused by the convex curvature, whereas adverse pressure gradient (APG) augments the reduction of the skin-friction over the convex wall for TS1. This behavior is a clear indication that an *interactive* process is occurring between the two applied extra rates-of-strain. Similar observations were made in the skin-friction distribution measured in the investigation by Bandyopadhyay and Ahmed (1993). In that study, an S-shaped duct resulted in asymmetrical responses between the two walls, clearly implying the interaction of the radial and streamwise strain rate. Note that the strong FPG combined with the moderate convex curvature (TS2) counteracts the stabilizing effects of the curved wall more strongly than does SFPG with the strong curvature (TS1).

Finally, the momentum thickness distribution along the measurement wall for all cases presented above is shown in Figure 3.4. The momentum thickness for flows over curved surfaces can be determined from an expression given by Simon and Honami (1981)

$$\int_0^{\theta} U_p dn = \int_0^{\infty} \left(U_p - \overline{U} \right) dn \qquad (3.1)$$

which yields

$$\theta = \int_0^\infty \left(1 + \frac{n}{R}\right) \frac{\overline{U}\left(U_p - \overline{U}\right)}{U_{pw}^2} dn \quad . \tag{3.2}$$

As expected, the convex curvature causes an increase for the ZPG cases, and the growth is more pronounced for the stronger curvature (Figure 3.4a). This effect is counteracted in the presence of favorable pressure gradients and augmented for adverse pressure gradient.

Spanwise variations of integral parameters were evaluated from single-component LDV measurements to check the mean two-dimensionality of the flow. Representative values of the skin-friction, displacement thickness, and potential wall velocity at five spanwise locations are listed in Table 3.2. The flow is reasonably two-dimensional at this streamwise location ($\alpha \approx 35^0$), where the largest variation of $\pm 5.1\%$ occurred for the skin-friction coefficient.

3.2 Initial Region of Curvature with Streamwise ZPG and FPG

In this section, the mean and fluctuating velocity and primary Reynolds stress profiles are presented with the emphasis on the region immediately downstream of the onset of curvature (within the first 20° of turning) to illustrate the effect of the abrupt change of surface curvature on the turbulent boundary layer. As discussed by Bradshaw (1973), the "memory time" of the stress-containing eddies in the outer portion of the boundary layer is approximately $s - s_0 \approx 10\delta_0$. This distance corresponds to 55° of turning in TS1 and 30° for TS2. All profiles presented in this section were acquired within the first 20° of both test sections. This is representative of the leading edge region of the suction (convex) side in a turbine vane passage, where the flow initially accelerates. Thus, the comparison between zero (ZPG) streamwise and strong favorable (SFPG) pressure gradients will be made. For all streamwise pressure gradient cases presented here, the flexible wall shape partially compensated the locally strong acceleration effects near the onset of curvature.

Two-component velocity profiles were acquired at different streamwise locations along the convex wall in the mid-plane of the test section (z=0 mm) to document the downstream development of the TBL under streamwise zero and strong favorable pressure gradient. All of the data sets are compared to a ZPG boundary layer over a smooth flat wall with $\mathrm{Re}_\theta \approx 3250$ and to the DNS results of Spalart (1988), where $\mathrm{Re}_\theta = 1410$. The shear velocity, u_τ, has been used for inner variable normalization. It was determined using the standard Clauser method, although the log-law must be used cautiously in curved TBLs (cf. Gibson, 1988; and Schwarz and Plesniak, 1996b). In this study, the classical constants ($\kappa = 0.41$ and $B = 5.0$) were retained to evaluate the shear velocity, primarily because no direct measurements of the wall shear stress were available and to facilitate comparison to the vast body of previous work on curved boundary layers (e.g. So & Mellor, 1973; Smits *et al.*, 1979; Gillis & Johnston, 1983; Muck *et al.*, 1985; Barlow & Johnston, 1988a, b). It was estimated that the maximum change in u_τ using the modified constants proposed by Gibson (1988) is 5%.

3.2.1 Mean Velocities

In Figures 3.5 and 3.6 the streamwise development of the mean velocity profiles over a moderately (TS2) and strongly (TS1) curved convex wall with zero compensated (ZPGC) and strong favorable compensated (SFPGC) streamwise pressure gradients are shown. As previously reported by other investigators (e.g. Gillis and Johnston, 1983 and Gibson *et al.*, 1984), the extent of the logarithmic region is reduced due to the presence of the convex curvature ($30 \le y^+ \le 100$). The DNS results of Spalart (1988) represent the near-wall behavior of the data throughout most of the boundary layer very well. Note that the deviation of the current flat-plate data from the DNS results in the outer portion of the boundary layer is due to the higher Reynolds number of the present data set.

The mean streamwise velocity is primarily affected outside the log-law region for all cases presented here. For the zero streamwise pressure gradient condition (Figure 3.5), the wake strength increases in the downstream direction. This behavior is more pronounced for the more moderate curvature case (Figure 3.5a). On the other hand, in the presence of a strong favorable pressure gradient, only small changes are observed in the outer portion of the boundary layer (Figure 3.6). Here, the favorable pressure gradient opposes the wake-enhancing effect of the convex curvature.

3.2.2 Fluctuating Velocity and Reynolds Stress Profiles

In this section, the root-mean-square (RMS) streamwise and wall-normal velocities and the primary Reynolds shear stress profiles are shown for the same conditions that were discussed above. These quantities were all normalized using the local shear velocity, u_τ (raised to the appropriate power). The profiles for the ZPGC cases are presented (Figures 3.7 through 3.9) before showing the results for the SFPGC cases (Figures 3.10 through 3.12).

The streamwise and wall-normal RMS velocities, shown in Figures 3.7 and 3.8 for the ZPGC case, collapse throughout the entire boundary layer at every streamwise location except for the first measurement station ($\alpha \approx 5^o$, Figure 3.7) for the moderate curvature case ($\delta_o/R \approx 0.05$) where both the streamwise and wall-normal RMS velocity are elevated relative to the downstream locations. The primary peak in the streamwise RMS velocities occurred at the same wall-normal distance ($y^+ \approx 15$) as for the flat plate case. The increase of both components relative to the flat plate values and the DNS data in the outer portion of the TBL is attributable to a difference in Reynolds number. The main effect of the increasing Reynolds number is the growth (here in inner variables) of the TBL.

In Figure 3.9, the primary Reynolds shear stress profiles exhibit similarity over the curved wall for the moderate wall curvature (Figure 3.9a) but change in the streamwise direction for the strong convex curvature (Figure 3.9b). In the latter case, there is a dramatic reduction in the primary Reynolds shear stress (uv^+) outside the logarithmic region with respect to flat plate values at the farthest downstream location ($\alpha \approx 20^o$). This effect has been reported by other investigators (e.g. So and Mellor, 1973, Gillis and Johnston 1983) and is attributed to the attenuation of the larger-scale structures in the outer portion of the boundary layer due to the strong stabilizing convex curvature. Chiwanga and Ramaprian (1993) showed that the size of the energy-containing eddies was dramatically reduced for a flow over a convex surface even with moderate curvature (their curvature parameter was $\delta_0 / R \approx 0.04$). These eddies are reduced in size because the streamlines near the free-stream have a convex curvature and the resulting normal pressure gradient causes a reduction in the entrainment of the ambient fluid by the boundary layer. It is also apparent in Figure 3.9b that the stronger convex curvature causes an increased reduction of the primary Reynolds shear stress immediately downstream ($\alpha \approx 8^o$) of the onset of curvature.

The combined effect of streamwise acceleration (SFPGC) along with convex curvature on the measured turbulent stresses is shown in Figures 3.10 through 3.12. These data illustrate that the favorable pressure gradient augments the Reynolds-stress-reducing effects of the convex curvature. The largest reduction in the RMS velocity profiles is observed for the moderate curvature case at the farthest downstream location, $\alpha \approx 20^o$ (Figure 3.10). For the same case, it is also noteworthy that for the initial streamwise evolution of uv^+, its peak value decreases downstream of the onset of curvature up to $\alpha \approx 10^o$, after which it rebounds to an even higher value than at $\alpha \approx 5^o$. Streamwise changes in the uv^+ profiles for the strong curvature case (Figure 3.12b) are not as dramatic as for the moderate convex curvature. At the first downstream location ($\alpha \approx 8^o$), the peak value is slightly reduced in the constant stress region relative to the downstream locations. On the other hand, it remains elevated relative to the two downstream locations in the outer portion of the boundary layer, which is due to a remnants of the larger-scale eddy structures.

3.3 Downstream Region of Curvature with Streamwise ZPG and FPG

3.3.1 Mean Velocities

In Figure 3.13, the mean normalized streamwise velocity component is shown to illustrate the downstream development of the TBL in the presence of a streamwise ZPG for the strong curvature case ($\delta_o/R \approx 0.10$). As discussed before, the extent of the log-law region is reduced ($30 \leq y^+ \leq 100$) due to the presence of the strong convex curvature. All of the data, including the DNS data set by Spalart (1988), collapsed quite well in the near-wall region of the TBL and throughout the log-law region. Initially, the wake component in the outer portion of the TBL increased with downstream distance. There was no further change in the profiles between the 45° and 55° locations, indicating that a state of equilibrium was reached sufficiently far downstream of the onset of curvature.

3.3.2 Fluctuating Velocity and Reynolds Stress Profiles

Profiles of the streamwise and wall-normal root-mean square (RMS) velocities, along with the primary Reynolds shear stress, shown in Figures 3.14 and 3.15, support the observations made for the mean streamwise velocity, namely that similarity is achieved by $\alpha \approx 45^\circ$. The RMS velocity components plotted in Figure 3.8 changed only slightly as the flowfield developed downstream. The primary peaks in the streamwise velocity, which occurred at the same wall-normal distance of $y^+ \approx 15$, were reduced by 14% compared to those measured on the flat plate. The primary Reynolds shear stress, shown in Figure 3.15, exhibits noteworthy features as well. Beyond the shortened logarithmic region, $-\overline{uv}/u_\tau^2$ is reduced relative to the flat plate values, which is attributable to the attenuation of the larger-scale structures in the outer portion of the boundary layer as discussed before

3.4 Closing Remarks

The results presented in this chapter document the importance of extra strain rates on the mean and turbulent statistics of the turbulent boundary layer. The convex curvature affected the turbulence immediately downstream of the onset of curvature and its effects are visible throughout almost the entire boundary layer. On the other hand, strong streamwise acceleration induced by a streamwise favorable pressure gradient (FPG), only modified the boundary layer mean and Reynolds stress profiles outside the log-law region. In the presence of FPG, the wake-enhancing effect of the convex curvature was counteracted, whereas the stabilizing effect on the turbulence was augmented.

The issues of equilibrium and how the turbulence production cycle responds to the sudden introduction of extra strain rates are discussed in the next chapter.

Table 3.1 Summary of cases investigated (⊗ indicates time-resolved, two-component velocity records)

Strong Curvature ($\delta/R \approx 0.10$), TS1

Δs; α / PGrads	kx10^6	8°	15°	20°	35°	45°	55°
ZPGU	0.0	–	–	⊗	⊗	–	⊗
ZPGC	0.0	⊗	⊗	⊗	⊗	⊗	⊗
FPG	0.5	⊗	⊗	⊗	⊗	⊗	⊗
SFPG	1.0	⊗	⊗	⊗	⊗	⊗	⊗
APG	-0.5	⊗	⊗	⊗	⊗	⊗	⊗

Moderate Curvature ($\delta/R \approx 0.05$), TS2

Δs; α / PGrads	kx10^6	$-5\delta_o$	$-1\delta_o$	0°	5°	10°	15°	20°	30°
ZPGU	0.0	⊗	⊗	⊗	*	⊗	⊗	⊗	⊗
ZPGC	0.0	⊗	⊗	⊗	⊗	⊗	⊗	⊗	⊗
SFPG	1.6	⊗	⊗	⊗	⊗	⊗	⊗	⊗	⊗

* no time-resolved data

Table 3.2 Spanwise (z-direction) variation of integral parameters at $\alpha \approx 35^{o}$ under ZPG conditions

z [mm]	c_f x 10^3	δ^* [mm]	U_{pw} [m/s]
-40	2.348	5.08	1.189
-20	2.350	4.81	1.218
0	2.438	4.46	1.214
20	2.551	4.41	1.195
40	2.444	4.98	1.188

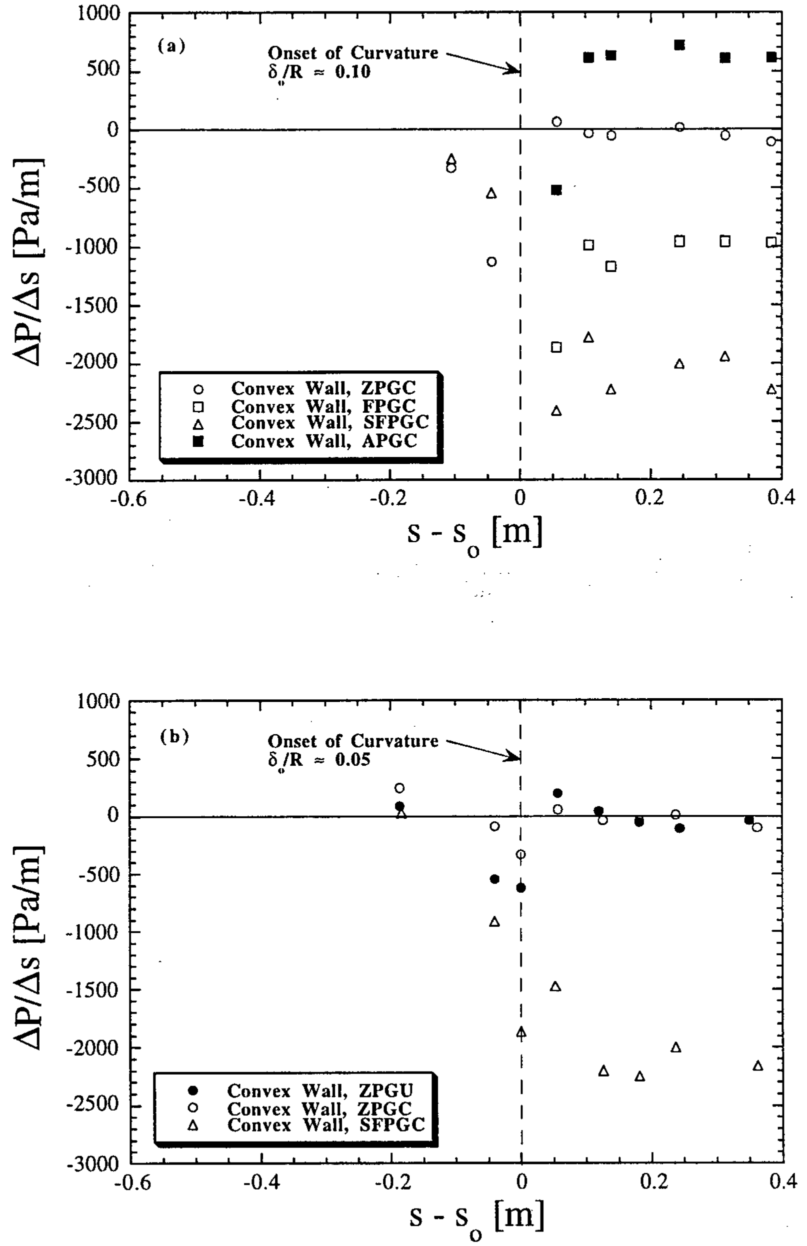

Figure 3.1 Pressure gradient distributions along measurement wall for (a) strong and (b) moderate convex curvature

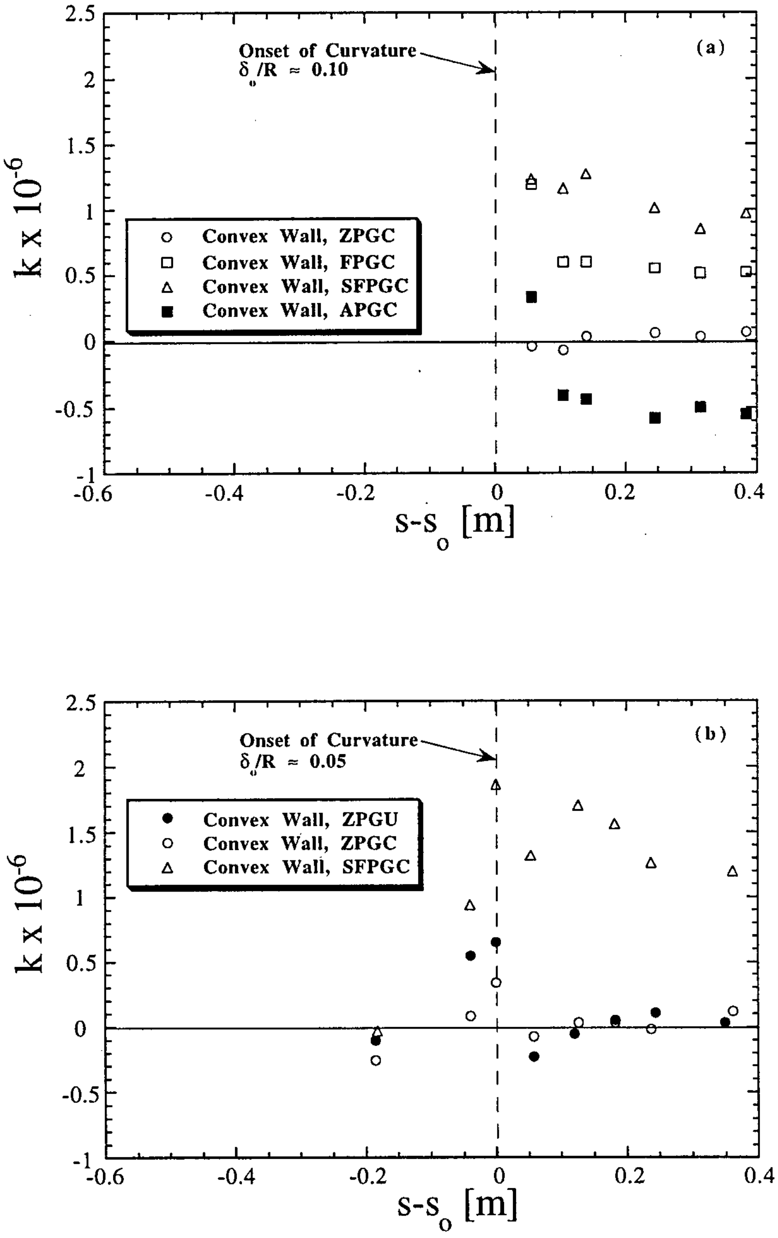

Figure 3.2 Acceleration parameter distributions along measurement wall for (a) strong and (b) moderate convex curvature

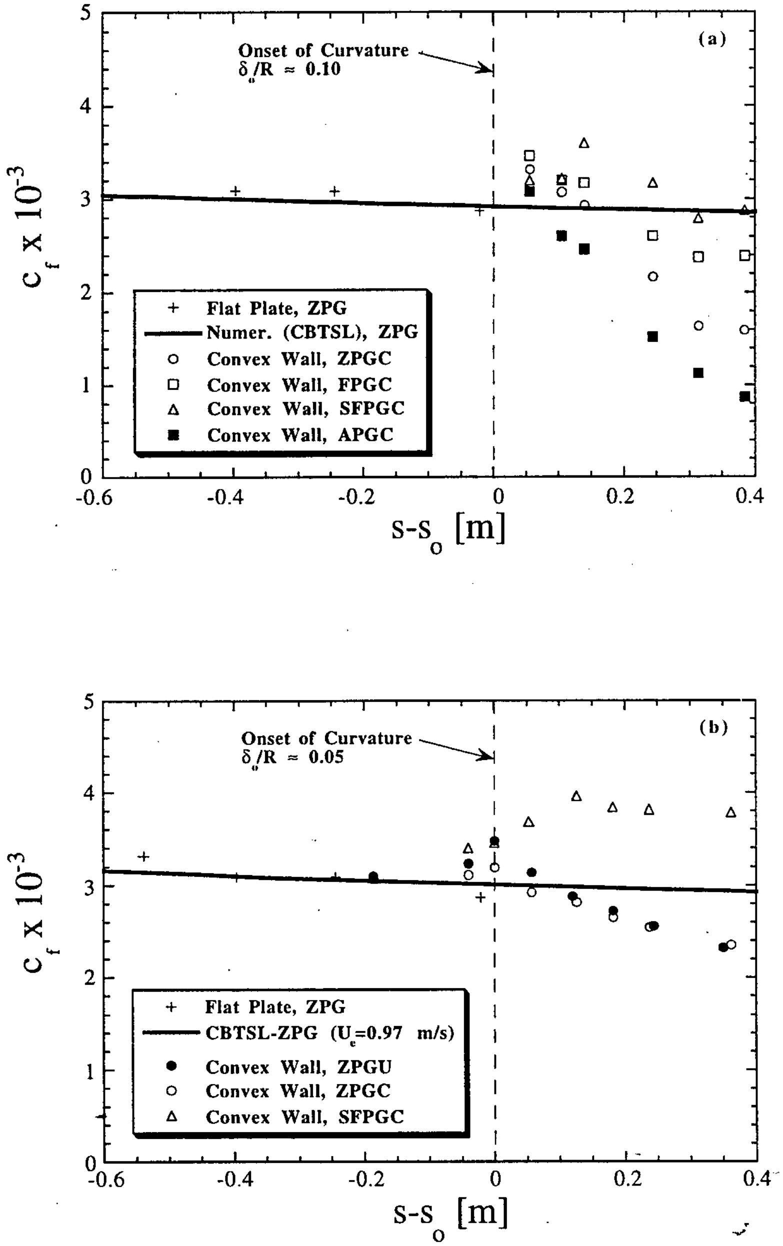

Figure 3.3 Distributions of skin-friction coefficient along measurement wall for (a) strong and (b) moderate convex curvature

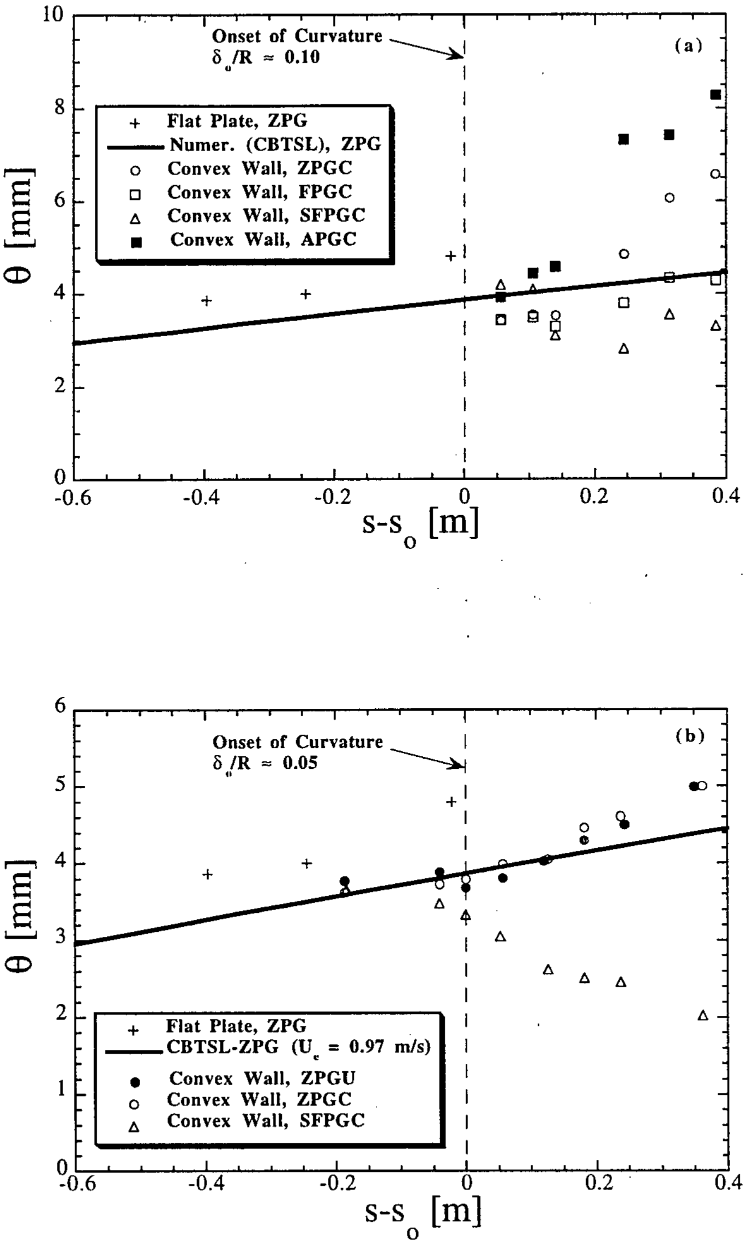

Figure 3.4 Momentum thickness distributions along measurement wall for (a) strong and (b) moderate convex curvature

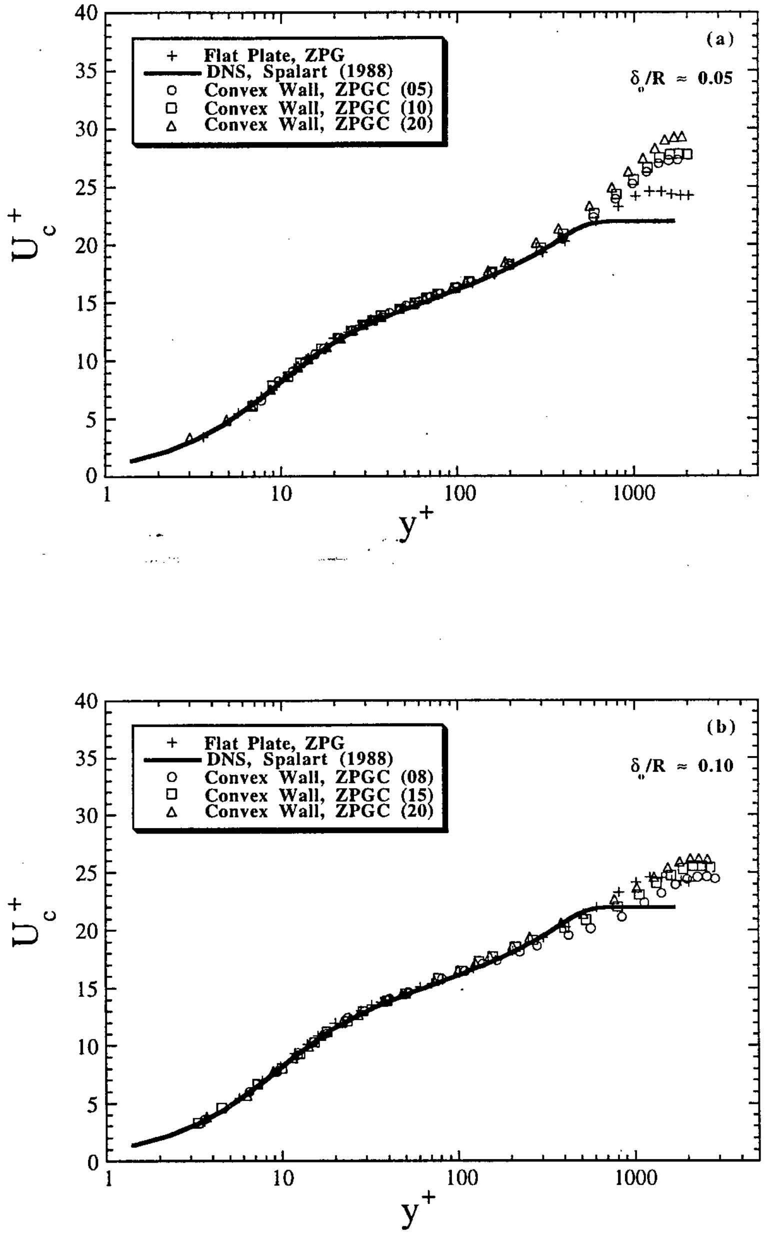

Figure 3.5 Mean streamwise velocity profiles for (a) TS2 and (b) TS1 under compensated zero pressure gradient conditions (ZPGC)

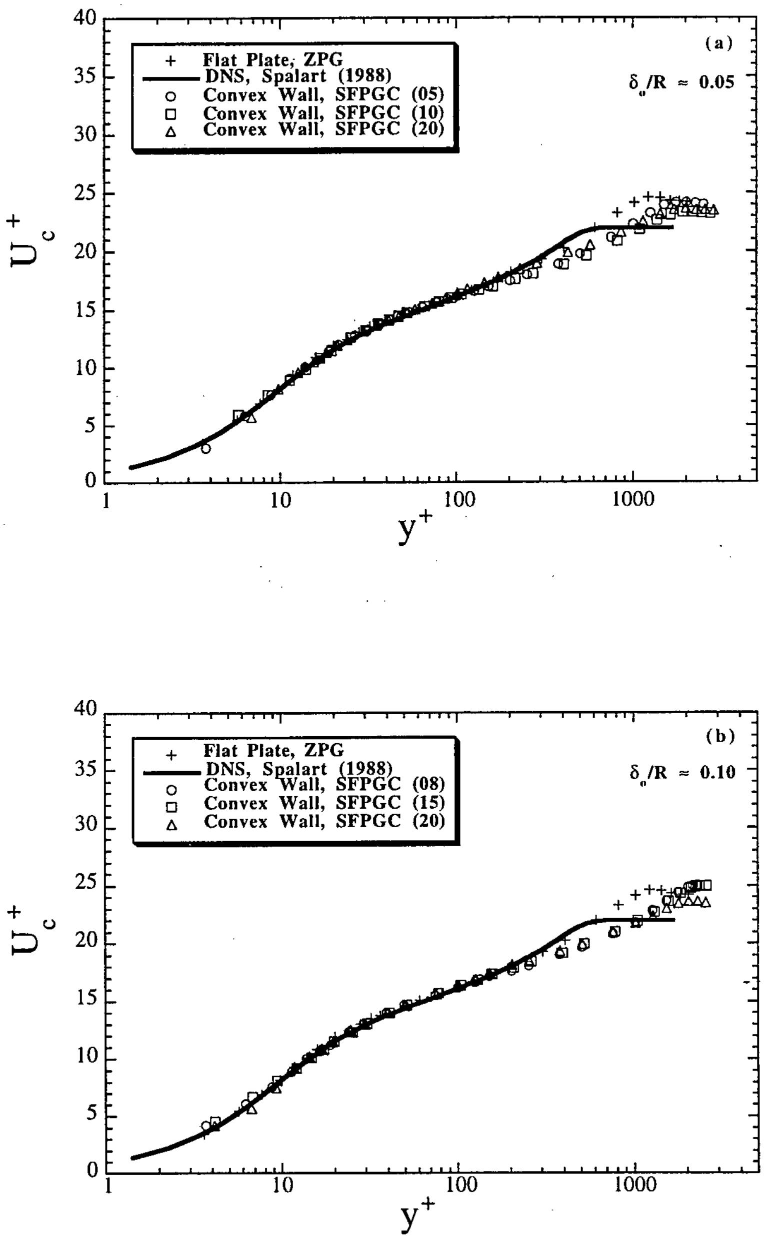

Figure 3.6 Mean streamwise velocity profiles for (a) TS2 and (b) TS1 under compensated strong favorable pressure gradient conditions (SFPGC)

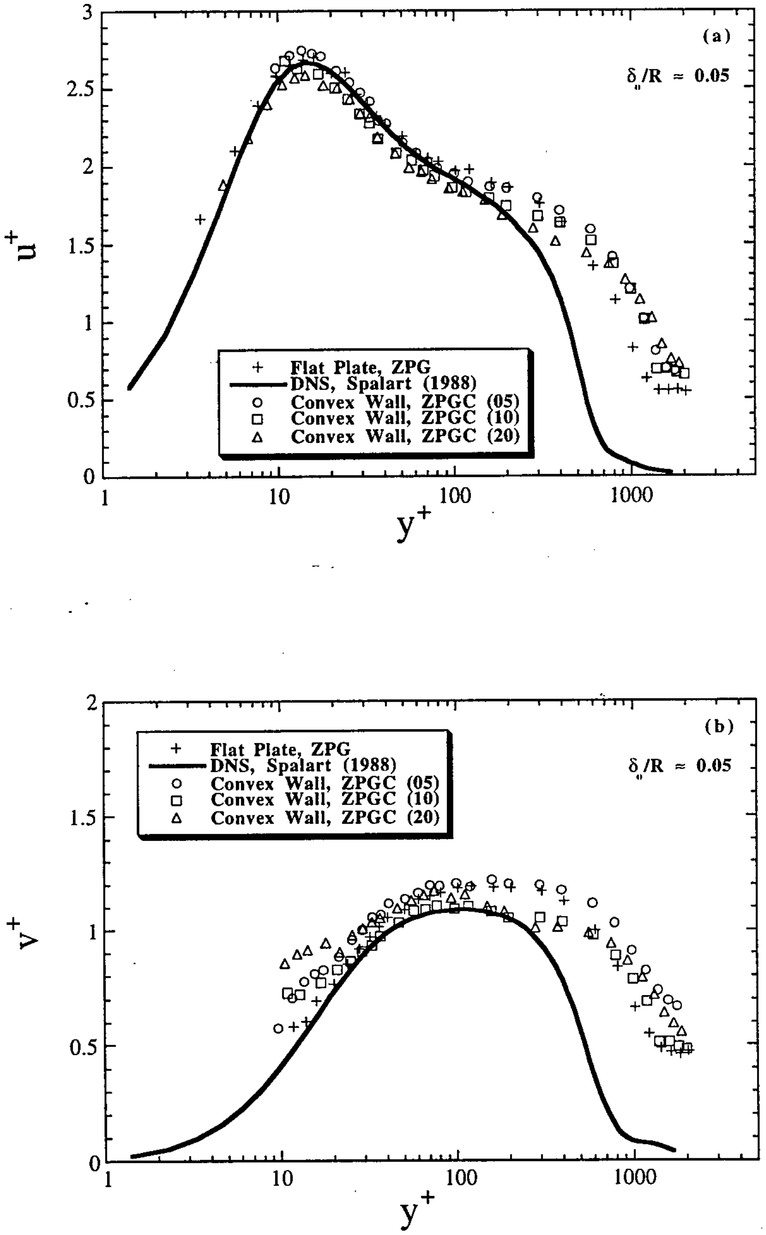

Figure 3.7 Profiles of RMS (a) streamwise and (b) wall-normal velocity for TS2 under ZPGC conditions

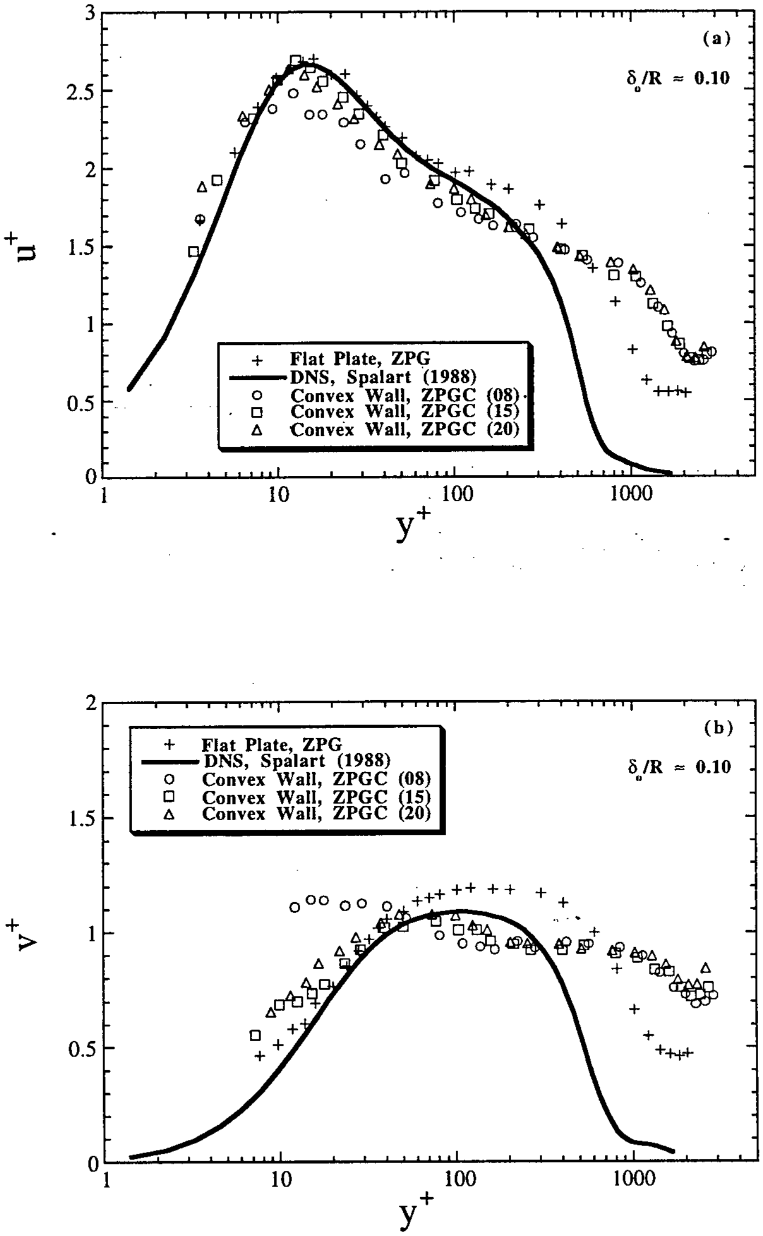

Figure 3.8 Profiles of RMS (a) streamwise and (b) wall-normal velocity for TS1 under ZPGC conditions

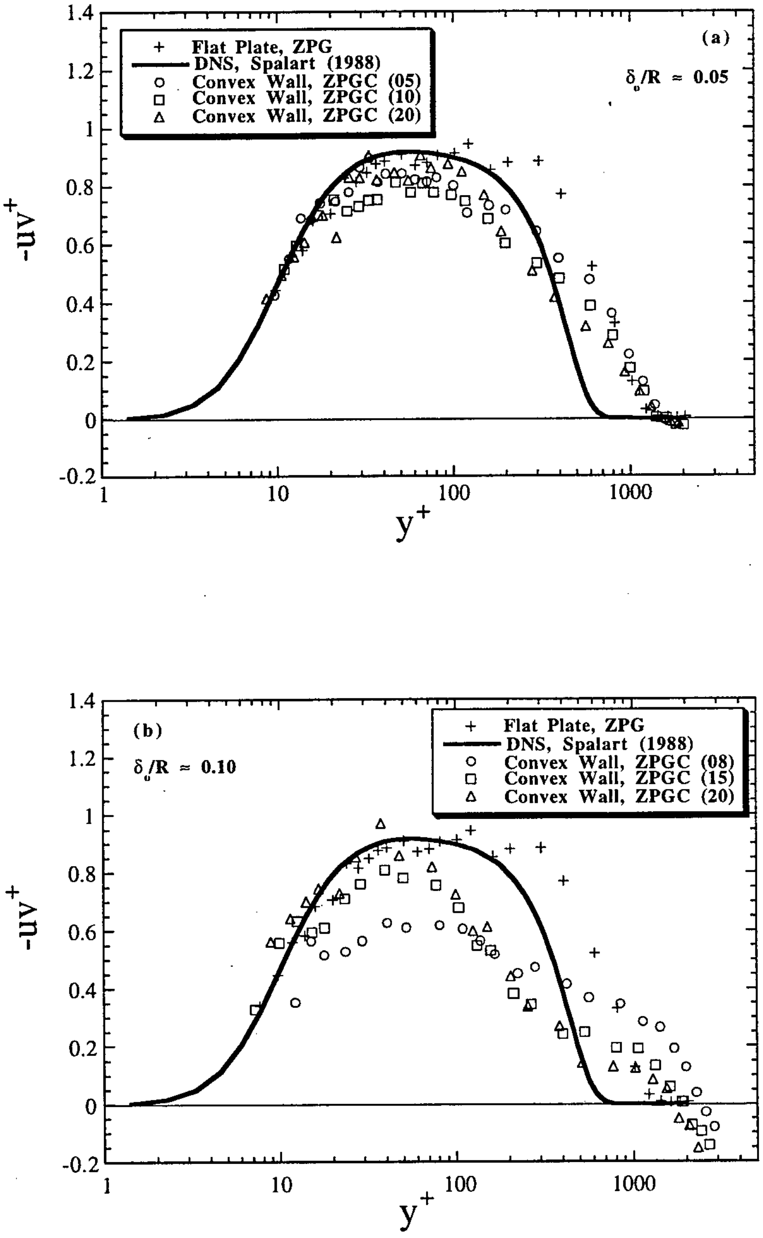

Figure 3.9 Primary Reynolds shear stress profiles for (a) TS2 and (b) TS1 under ZPGC conditions

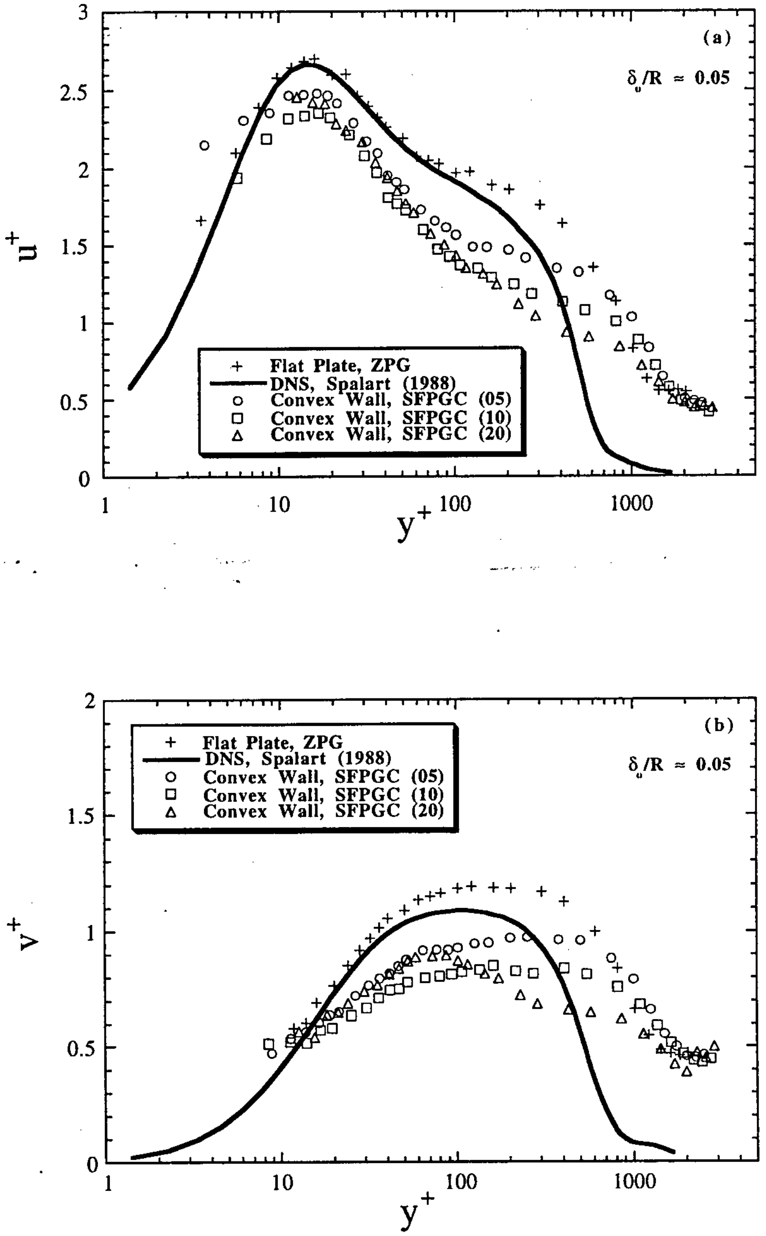

Figure 3.10 Profiles of RMS (a) streamwise and (b) wall-normal velocity for TS2 under SFPGC conditions

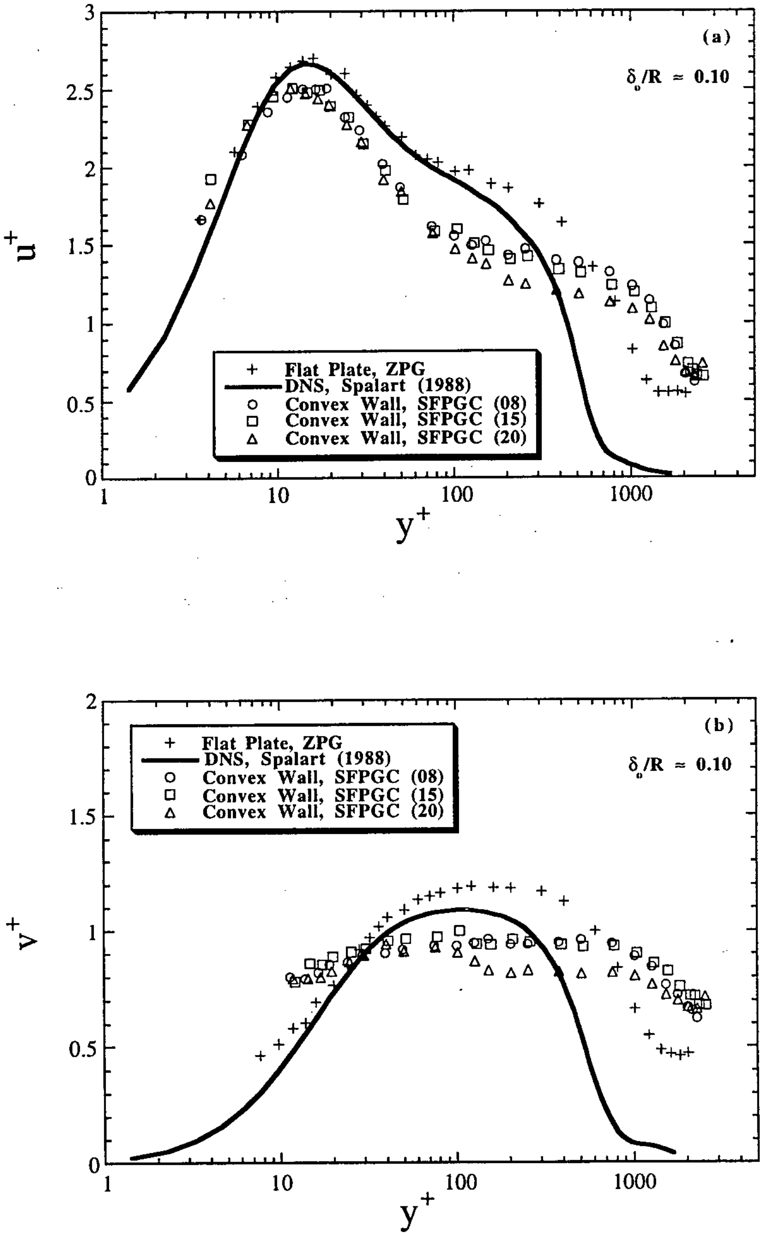

Figure 3.11 Profiles of RMS (a) streamwise and (b) wall-normal velocity for TS1 under SFPGC conditions

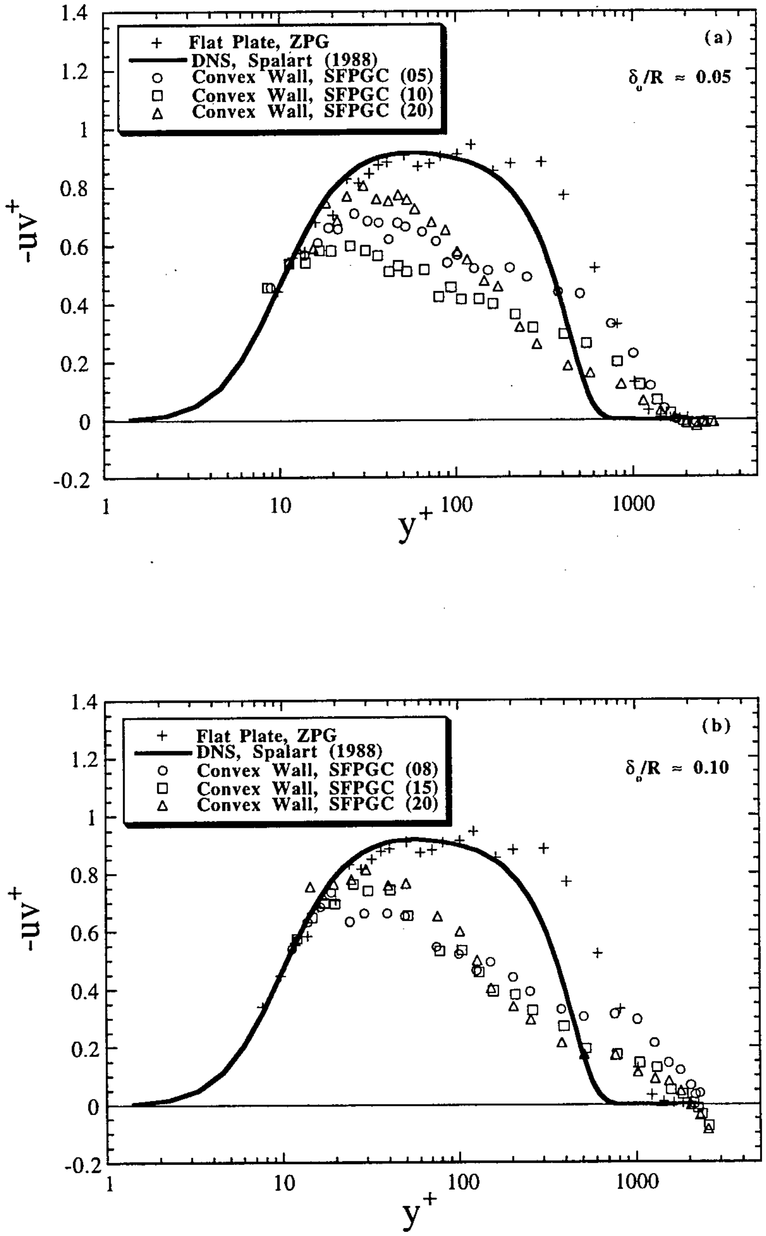

Figure 3.12 Primary Reynolds shear stress profiles for (a) TS2 and (b) TS1 under SFPGC conditions

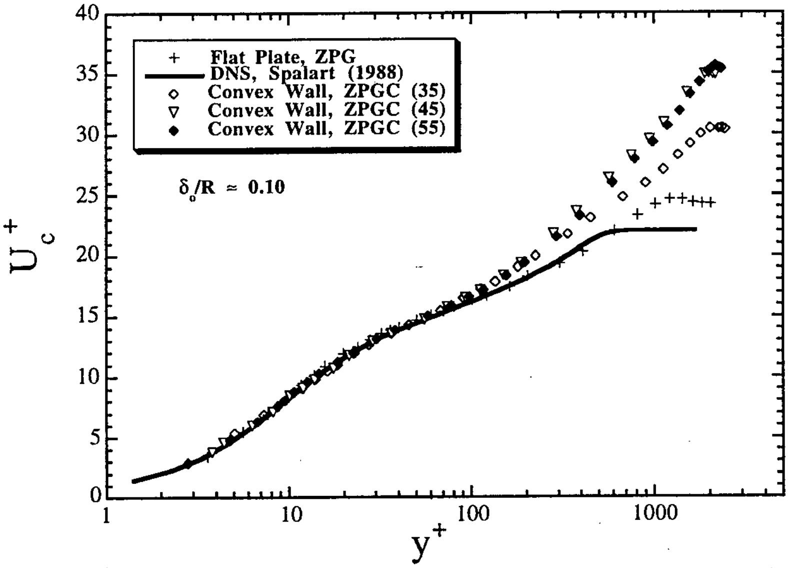

Figure 3.13 Mean streamwise velocity profiles for TS1 under compensated zero pressure gradient conditions (ZPGC)

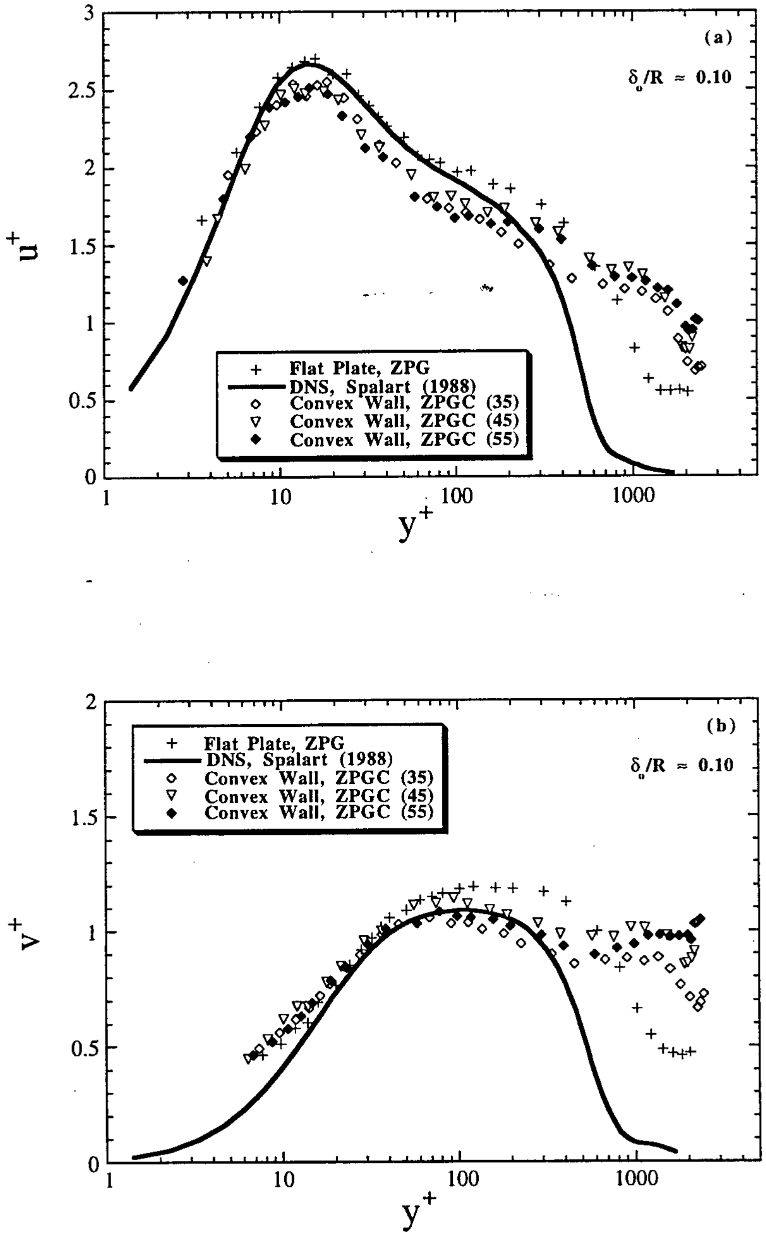

Figure 3.14 Profiles of RMS (a) streamwise and (b) wall-normal velocity for TS1 under compensated zero pressure gradient conditions (ZPGC)

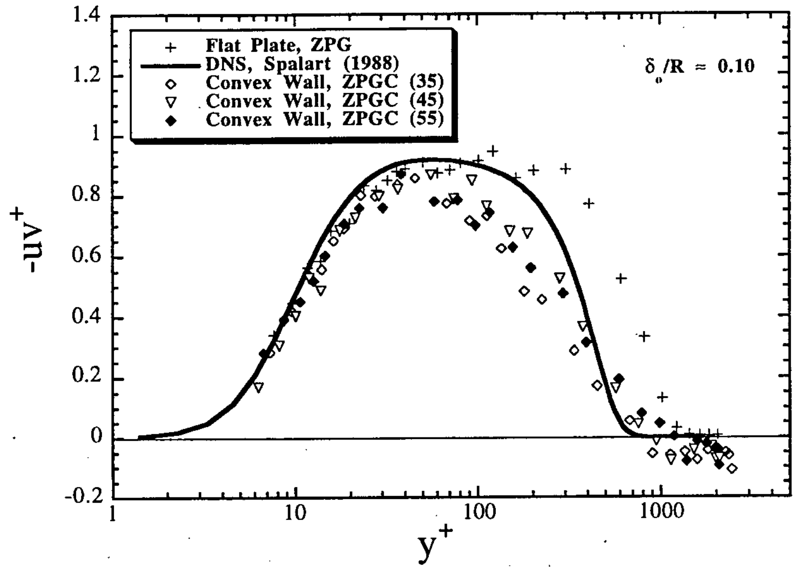

Figure 3.15 Primary Reynolds shear stress profiles for TS1 under compensated zero pressure gradient conditions (ZPGC)

CHAPTER 4. ANALYSIS OF RESULTS AND DISCUSSION

In this chapter, a detailed description and analysis of the structural features of a turbulent boundary layer that is subjected to two interacting extra strain rates will be given. The main emphasis is on how these additional strain rates modify the mean and turbulence flow field. Special attention will be given to how the different strain rates interact with each other. First, a detailed discussion of the different wall shapes used to establish certain streamwise pressure gradients along the convex wall will be given. Then, the data are analyzed with respect to equilibrium criteria. The remainder of this chapter is devoted to discussion of the effect of the various experimental conditions on the mean and turbulence quantities and on the turbulence production cycle.

4.1 Wall Shapes and Pressure Gradients

In order to better understand the overall flow physics of turbulent boundary layers that are exposed to multiple extra rates of strain, it is necessary to closely investigate the response of the streamwise pressure gradient (PGrad) to a set geometry and the wall curvature. The primary goal in contouring the flexible wall opposite to the convex measurement wall was to establish nominally constant streamwise PGrads downstream of the onset of curvature. Unfortunately, it is not possible to introduce a step change in the streamwise PGrad due to limitations on the attainable shape of the flexible wall. Even if a step change in the flexible wall shape would have been feasible, the finite response time of the mean flow would preclude a step-change in pressure gradient. The objective of the analysis in this section was to investigate the mechanism by which multiple extra strain rates affect the mean flow field. In the following paragraph, the flexible wall shape and the resulting PGrads are discussed using measurements that were acquired in the moderate curvature ($\delta_0/R \approx 0.05$) test section.

Different types of zero (ZPG) and strong favorable (SFPG) streamwise PGrads were employed. An important distinction is made between natural (ZPGN and SFPGN) and compensated (ZPGC and SFPGC) conditions. In the natural case, the flexible wall was not adjusted near the onset of curvature (both upstream and downstream). This led to a locally accelerated flow on the convex wall as reported by So and Mellor (1973). The effect was counteracted for the compensated case by widening the flow cross-sectional area near the onset of curvature. In both cases, the flexible wall in the curved region was adjusted to yield a constant streamwise PGrad. For the third ZPG case (ZPGU), the wall correction was not employed upstream of the onset of curvature, but was applied downstream to account for δ^*.

The different wall shapes and the resulting streamwise PGrads are shown in Figure 4.1. The overall trend is that, except for a region near the onset of curvature ($-5.5\ \delta_o \leq s\text{-}s_o \leq 5.5\ \delta_o$), all PGrads are essentially constant sufficiently downstream of the onset of curvature. The total amount by which the flow area was increased to compensate for the local acceleration in the initial region was approximately 0.3 δ_o for the ZPG case and 0.2 δ_o for the SFPG case. For the ZPGC case, the local favorable pressure gradient at the onset of curvature was reduced by a factor of 4.5 through careful contouring of the flexible wall.

In Figures 4.2, 4.3 and 4.4, the wall shape, the wall slope and the streamwise pressure gradients are shown for the two cases separately (ZPG and SFPG), in order to gain further insight. The wall slope, $\Delta h/\Delta s$, was calculated from the wall shape using a first-order, forward-difference scheme. In Figure 4.2, the different wall shapes for the two cases shown here clearly support the observations made earlier in this section. Here, the wall shapes are similar except for a region near the onset of curvature. By expanding the ordinate scale, it becomes evident that for both SFPG cases studied here, the downstream wall shapes are almost identical. In addition, there are two distinct regions with constant wall slopes for the SFPG cases, which are especially apparent in the wall slope distribution shown in Figure 4.3. In this figure, two regions with different constant wall slopes can be identified downstream of the onset of curvature with the transition occurring at $s\text{-}s_o \approx 0.35$m or 10 δ_o. This downstream distance is identical to that computed from the "memory time", X, (multiplied by convection velocity) of the energy-containing eddies (Bradshaw 1973), and can be estimated from

$$X = \frac{0.5\,\overline{q^2}}{-\overline{uv}\,\partial\overline{U}/\partial y}\ \overline{U} \tag{4.1}$$

where $\overline{q^2} = \overline{u_{ii}} = \overline{u^2} + \overline{v^2} + \overline{w^2}$ is the trace of the Reynolds stress tensor (twice the turbulent kinetic energy). For a linear interaction between the applied strain rates, it is expected that the wall shape employed to achieve a constant streamwise pressure gradient remains consistent, i.e. constant wall slope over the entire streamwise distance. However, that behavior was not observed in the data, implying a non-linear interaction. In summary, the wall shapes needed to establish constant static pressure gradient distributions demonstrate that the interaction between the extra rates-of-strain ($\partial\overline{V}/\partial s$ and $\partial\overline{U}/\partial s$) is nonlinear.

4.2 Equilibrium Boundary Layer Considerations

A turbulent boundary layer becomes an equilibrium layer when the velocity profiles are independent of the Reynolds number and the downstream distance s, if non-dimensionalized using an appropriate velocity-defect law (Tennekes & Lumley, 1972). Strictly speaking, a given class of shear flows achieves some state of dynamical equilibrium, in which the local energy input should approximately balance the local loss (mostly through viscous dissipation), i.e.

$$-\overline{uv}\frac{\partial\overline{U}}{\partial y}+\varepsilon\approx 0 \ . \tag{4.2}$$

Equation (4.2) governs the transport of turbulent kinetic energy for homogeneous, stationary turbulence (Hinze, 1975).

The most common thickness parameter for equilibrium flows was determined by Clauser (White, 1974) and is defined as:

$$\Delta=\int_0^\infty\frac{U_e-\overline{U}}{u_\tau}\,dy=\delta^*\lambda \ , \tag{4.3}$$

where $\lambda=\sqrt{2/c_f}$. All velocity profiles can be scaled with y/Δ for a constant Clauser equilibrium shape factor given by:

$$G=\frac{1}{\Delta}\int_0^\infty\left(\frac{U_e-\overline{U}}{u_\tau}\right)^2 dy \tag{4.4}$$

The characteristic value for G is 6 to 7 in a ZPG equilibrium boundary layer. This parameter can be related to the conventional shape factor H ($H=\delta^*/\theta$) by the following:

$$H = \left(1 - \frac{G}{\lambda}\right)^{-1} \Leftrightarrow G = \lambda\left(1 - \frac{1}{H}\right) . \tag{4.5}$$

In an equilibrium boundary layer, the shape factor H varies with the downstream distance because the skin-friction is not constant even though G is.

The departure and return to equilibrium can be described in a (G, β)-plane, where the Clauser equilibrium parameter β is the ratio of pressure to wall friction forces given by

$$\beta = \left(\frac{\delta^*}{\tau_w}\right)\left(\frac{dP}{ds}\right) . \tag{4.6}$$

The streamwise distribution of β is shown for both convex curvatures in Figure 4.5. It is obvious that the adverse pressure gradient acting along with the strong curvature never reaches equilibrium. On the other hand, β tends to a constant value as the flow develops along the convex wall for all other cases.

In Figure 4.6, the (G, β) trajectories are shown for the different streamwise pressure gradients in both test sections. For the strong curvature case, shown in Figure 4.6a, the trajectories for the ZPGC and APGC cases move away from the initial equilibrium, an effect which is most pronounced for the APGC case. In the presence of ZPGC and SFPGC, the boundary layer reaches a new equilibrium condition (with $G \approx 12.9$ for ZPGC and $G \approx 7.1$ for SFPGC). It is surprising that for moderate curvature case (Figure 4.6b), G is rather far from equilibrium at the last measurement location ($\alpha \approx 30°$) for both ZPG cases, whereas in the presence of SFPG, the trajectory tends to return to the initial equilibrium condition, in a non-linear fashion. The same trend can be observed for strong curvature case and SFPGC. A similar behavior was reported by Bandyopadhyay and Ahmed (1993) on both walls of an S-shaped duct. They termed this behavior an hysteresis of the large eddies. These authors also emphasized the importance not only of β but also the effect of $d\beta/ds$ when modeling turbulent boundary layers with streamwise pressure gradient. Note that $d\beta/ds$ accounts for the application rate of the streamwise pressure gradient. The rate of application should also be important when streamwise pressure gradients are combined with radial strains.

4.3 Combined Strain Rates

4.3.1 Effects of Different Streamwise Pressure Gradients

In order to emphasize the effect of different streamwise pressure gradients and their interaction with the convex wall TBL, the data sets discussed below (mean velocity and Reynolds stress profiles) were acquired at one fixed streamwise location, $\alpha \approx 15°$ with different streamwise pressure gradients. As before, they are compared to a ZPG boundary layer that formed over a smooth flat wall with $Re_\theta \approx 3250$ and the DNS results of Spalart (1988). In terms of the acceleration parameter k, the strengths of the imposed streamwise pressure gradients were $k \approx 1.16 \times 10^{-6}$ for the strong compensated favorable pressure gradient (SFPGC), and $k \approx -0.41 \times 10^{-6}$ for the moderate compensated adverse pressure gradient (APGC).

In Figure 4.7, the mean streamwise velocity is shown as a function of the normalized wall-normal coordinate with zero, strong favorable and adverse streamwise pressure gradients at one fixed streamwise location ($\alpha \approx 15°$). This particular streamwise distance was chosen because it is just downstream of the region that is influenced by a locally strong favorable pressure gradient due to sudden change in wall curvature. The mean profiles collapse quite well throughout the logarithmic region, whereas the wake component (outer portion of the turbulent boundary layer) is reduced with increasing strength of FPG, and elevated for APG. As previously reported by other investigators (cf. Gillis and Johnston, 1983; and Gibson, 1984) and in chapter 3, the extent of the logarithmic region was reduced with respect to a flat plate turbulent boundary layer ($30 \leq y^+ \leq 100$). Again, the near-wall behavior is very well represented throughout the logarithmic region by the DNS results of Spalart (1988). Favorable pressure gradient has the tendency to oppose the wake-enhancing effect of the convex curvature, whereas the APG increases the wake component even more. On the other hand, both convex curvature and FPG tend to stabilize the turbulence within the boundary layer, while APG acts to destabilize it.

The streamwise and normal RMS velocities, along with the primary Reynolds shear stress (shown in Figures 4.8 and 4.9) illustrate some interesting features of the imposed extra rates of strain. The near-wall behavior ($y^+ \leq 50$) of the normal stress components is almost entirely compensated by changes in u_τ when subjected to interacting strain rates of different magnitude, except for a reduction of the primary peak in the streamwise RMS velocity relative to the measured flat plate values. Beyond the near-wall region, all Reynolds stress components are reduced relative to the flat plate values except in the wake region. This effect was augmented by the imposed SFPGC and counteracted by the APGC. Similar effects have been observed in flat plate turbulent boundary layers with different streamwise pressure gradients (cf. Koskie, 1991; and Smits *et al.*, 1983). Another interesting trend can be seen in the different profiles of the primary Reynolds shear stress, shown in Figure 4.9. Outside the logarithmic region, this shear stress component is reduced relative to the flat plate values, an effect which has been observed by other investigators (cf. So and Mellor, 1972; Gillis and Johnston, 1983; and Chiwanga and Ramaprian, 1993). Apparently, the process is not yet completed at this measurement location even in the presence of a strong FPG. The effect of the different interacting streamwise pressure gradients on the primary Reynolds shear stress is noticeable throughout almost the entire boundary layer. In general, the SFPGC tends to reduce the turbulent shear stress correlation, whereas the APGC has the opposite effect.

4.3.2 Pressure Gradient Ratios

Two-component velocity data were acquired for different pressure gradient ratio (P_{rat}) conditions in the mid-plane of the test surface. The data sets presented were acquired at $\alpha \approx 15°$ for zero and strong favorable streamwise pressure gradients. In the strong favorable pressure gradient cases (SFPG), typical values for the streamwise acceleration parameter $k = \nu / U_e^2 \cdot dU_e / ds$ were: $k \approx 1.2 \times 10^{-6}$ for TS1 and $k \approx 1.8 \times 10^{-6}$ for TS2. These conditions correspond to a pressure gradient ratio of $P_{rat} \approx 0.73$ for strong curvature (TS1) combined with SFPGC and 1.22 for moderate curvature (TS2) combined with SFPGC.

In Figure 4.10, the mean streamwise velocity normalized with the shear velocity, is shown as a function of the normalized wall-normal coordinate in the typical fashion of the law of the wall. The largest increase of the wake component occurred when the longitudinal ZPG interacted with the convex curvature, especially for the moderate curvature case, whereas the strong FPG had the tendency to oppose the wake-enhancing effect of the stabilizing curvature. This effect was most pronounced in the moderate curvature case which corresponds to the high P_{rat} case, whereas in the presence of the strong convex curvature, the reduction of the wake component relative to the corresponding ZPG case was minimal. Thus, inner variable scaling accounts for the effects of the interacting strain rates in the inner region, and the mean velocity profiles collapse. The largest deviations are observed in the outer portion of the TBL, where inner scaling is not applicable.

The streamwise and wall-normal root-mean square (RMS) velocities, along with the primary Reynolds shear stress component, shown in Figures 4.11 and 4.12 further illustrate the effects of the different pressure gradient ratios. The inner normalized RMS velocities, shown in Figure 4.11, exhibit some new features in addition to the ones discussed in section 4.3.1. For both curvature cases, the streamwise normal stress is reduced in the presence of favorable pressure gradients relative to the ZPG cases but this reduction is greater for the higher pressure gradient ratio. For the wall-normal RMS component, the same trends occur now throughout the entire boundary layer.

Profiles of the primary Reynolds shear stress, $-\overline{uv}$, are shown in Figure 4.12, where the effects of the interacting strain rates under different pressure gradient ratio conditions are obvious. The imposed favorable streamwise pressure gradient, coupled with convex curvature, further reduces $-\overline{uv}$ throughout almost the entire TBL. This effect is consistent for both curvature cases. It is noteworthy that the reduction in the outer portion ($y^+ \geq 50$) of the boundary layer is greater for the higher P_{rat} case, i.e. moderate curvature combined with SFPGC. The stabilizing effects of the different strengths of curvature can also be observed in the outer portion of the Reynolds stress profiles. Comparing both ZPG cases with different curvatures, the destruction of the energy-containing eddies is more advanced in the case of the stronger convex curvature, resulting in greater suppression of $-\overline{uv}$ in the outer portion of the TBL. In summary, streamwise acceleration of the turbulent boundary layer combined with moderate convex curvature yields stronger stabilization of the TBL than an accelerated flow (same magnitude FPG) combined with strong convex curvature.

4.4 Turbulence Production Cycle

4.4.1 Turbulent Bursting Period

In Figure 4.13, the mean burst period normalized with inner variables ($\overline{T}_B^+ = \overline{T}_B \cdot u_\tau^2 / \nu$) is shown for both curvature cases as a function of the streamwise distance along the convex wall for ZPG (both compensated and uncompensated), FPGCs, and APGC. For the strong curvature case (Figure 4.13a), the burst period was elevated immediately downstream of the onset of curvature (less frequent bursting), and even further elevated in the presence of favorable pressure gradients. On the other hand, it was reduced for the adverse pressure gradient, indicating a more frequent occurrence of these events. The same trends were also observed for mixed and outer normalization of the burst period (Schwarz & Plesniak, 1996a). The (inner normalized) burst period was 18% greater at $\alpha \approx 15°$ ($s\text{-}s_0 \approx 105$ mm) for the strongest FPGC case (SFPGC) compared to the ZPGC case. In addition, the duration of ejections became shorter in the presence of SFPGC. The (inner normalized) duration times for ejections at four different stations for all streamwise pressure gradients are listed in Table 4.1. It clearly shows that the duration decreases in the presence of favorable streamwise pressure gradients. The values shown in table 4.1 correspond to a particular threshold value of H=0.2 but the trends are the same for the entire threshold independent range. Thus, because bursts are less frequent and of shorter duration upstream of the initial region ($\alpha \leq 20^0$), FPGC in the convex turbulent boundary layer is associated with a suppression of the turbulence production cycle. Although the difference in the (inner normalized) burst period decreased with downstream distance, the combination of the strong curvature with strong FPGC resulted in an increased stabilization of the turbulent boundary layer throughout the measurement domain (28% at 55°, $s\text{-}s_0 \approx$ 384 mm). Different levels of FPGC were found to suppress the turbulence production cycle to some extent, complementing the stabilizing effect of convex curvature.

On the other hand, the interaction of the strong convex curvature with APGC had the opposite effect. Especially in the initial curved wall region (but even up to $\alpha \approx 35°$, $s\text{-}s_0 \approx 244$ mm), the burst period was reduced relative to the ZPGC values. In any case, the turbulent burst period remains elevated in the initial region, immediately downstream of the onset of curvature, which is attributed to the sudden change in surface curvature and the associated local FPG. However, in the presence of APGC, the ejection duration is reduced compared to all other cases along the entire test surface, as shown in Table 4.1. This perhaps surprising behavior can be linked to the initially strong application rate of the streamwise strain rate, causing a reduction in the duration of uv_2 events, accompanied with more frequent occurrence of the bursting events. Overall, APGC is associated with increased turbulence production, which coincides with an increase of the primary Reynolds shear stress, despite the fact that the ejection duration of the detected events was reduced. Therefore, an important result of this study is that not only the magnitude but also the *rate of application* of the strain rate dictates the state of the turbulence throughout the measurement domain.

In Figure 4.13b, the burst periods for the moderate curvature case are shown. Also included is the value for the upstream flat plate reference station. In this case, data are shown for three different streamwise pressure gradient distributions, two zero (compensated and uncompensated) and strong favorable pressure gradient (SFPGC). The uncompensated zero pressure gradient (ZPGU) exhibits a stronger local acceleration at the onset of curvature compared to the compensated case (ZPGC), because the flexible wall opposite the measurement wall was not compensated to counteract the initial acceleration. As in the strong curvature case, the burst period is elevated near the onset of curvature due to the stabilizing nature of the local favorable pressure gradient. The burst period decreases monotonically downstream for both ZPGs. On the other hand, a dramatic increase in T_B occurs initially in the presence of the SFPGC, reaching a maximum at $\alpha \approx 15°$ ($s\text{-}s_0 \approx 183$ mm). This trend is completely opposite to that observed for the strong curvature case, where the burst period decreased monotonically after reaching a maximum value immediately downstream of the onset of curvature. In comparison with Figure 4.13a, it is evident that the turbulence production cycle experiences a higher suppression when SFPGC and moderate curvature are combined. Recall, that the ratio of the streamwise (SFPGC) to radial pressure gradient, P_{rat}, is 1.22 for the moderate and 0.73 for the strong convex curvature.

The inner normalized duration of ejection events for the moderate curvature data, shown in tables 4.1 and 4.2, support the bursting period trends except for the anomalous APGC discussed above. In general, the ejection duration is shorter in the presence of SFPGC than for either ZPG case. This indicates that the strong favorable pressure gradient has a stabilizing effect on the turbulent boundary layer when combined with a more moderate convex curvature and it is in good agreement with the Reynolds stress measurements. Overall, the analysis of the turbulence production cycle in terms of the burst period and ejection duration has shown that both extra rates of strain (streamwise and wall-normal) affect the near-wall dynamics of the turbulent boundary layer, and that the application rate in conjunction with the magnitude of the newly applied strain rates have to be considered when interpreting these results.

4.4.2 Reynolds Stress Production Terms

As reported in section 4.3.2, changes in the pressure gradient ratio have a significant effect on the Reynolds stresses and on the turbulence production cycle. In order to examine this behavior further, the dominant production terms for the streamwise normal Reynolds stress and the primary Reynolds shear stress for the same cases are discussed next. For a curved boundary layer, the production terms for the streamwise normal and primary Reynolds shear stress are (cf. Prabhu and Rao, 1981; and Bradshaw, 1973)

$$\mathrm{Prod}\left(\overline{u^2}\right) = -\overline{uv}\left[\frac{\partial \overline{U}}{\partial y} - h\overline{U}\right] \tag{4.7}$$

and

$$\mathrm{Prod}\left(-\overline{uv}\right) = \overline{v^2}\frac{\partial \overline{U}}{\partial y} - h\overline{U}\left[2\overline{u^2} - \overline{v^2}\right] \tag{4.8}$$

where $h = 1 + y/R$.

These quantities are plotted in Figure 4.14 using inner normalization. They are compared with the measured flat plate data and the DNS data of Spalart (1988). The profiles for the production of the streamwise normal Reynolds stress (Figure 4.14a) are essentially identical to each other and to the flat plate data throughout the entire boundary layer. Small differences are noticeable outside the log-law region, where streamwise favorable pressure gradient augments the stabilizing effect of the convex curvature as already seen in the Reynolds stresses (Figures 4.11 and 4.12). On the other hand, the production for the primary Reynolds shear stress, shown in Figure 4.14b, exhibits some interesting features. As expected, the production of $-\overline{uv}$ is reduced in the same portion of the boundary layer as the primary Reynolds shear stress.

Combined with the results from chapter 3, these data indicate that the applied extra rates-of-strain effects on the near-wall region of the turbulent boundary layer are completely scaled by changes in u_τ, and that the flow field is most obviously affected in the outer portion of the boundary layer. Since the turbulence bursting period shows significant changes for the different cases discussed, these results suggest that the bursting phenomenon is controlled by the dynamics of the entire boundary layer. Furthermore, they imply that the production cycle mechanisms are closely coupled with the applied strain rates.

Table 4.1 Inner normalized ejection duration $\Delta\tau_E^+ = \Delta\tau_E u_\tau^2 / \nu$ for different streamwise pressure gradients (H=0.2) with $\delta_0 / R \approx 0.10$

Case	$\alpha \approx 15°$	$\alpha \approx 20°$	$\alpha \approx 35°$	$\alpha \approx 55°$
APG	1.45	1.70	1.71	1.78
ZPG	1.95	2.17	2.33	2.13
FPG	2.05	2.02	2.18	2.13
SFPG	1.68	1.88	2.04	2.07

Table 4.2 Inner normalized ejection duration $\Delta\tau_E^+ = \Delta\tau_E u_\tau^2 / \nu$ for different streamwise pressure gradients (H=0.2) with $\delta_0 / R \approx 0.05$

Case	$\alpha \approx 0°$	$\alpha \approx 10°$	$\alpha \approx 15°$	$\alpha \approx 20°$	$\alpha \approx 30°$
ZPGU	2.43	2.12	1.94	1.83	1.49
ZPGC	2.13	1.87	1.93	1.83	1.75
SFPG	2.16	1.64	1.73	2.02	1.56

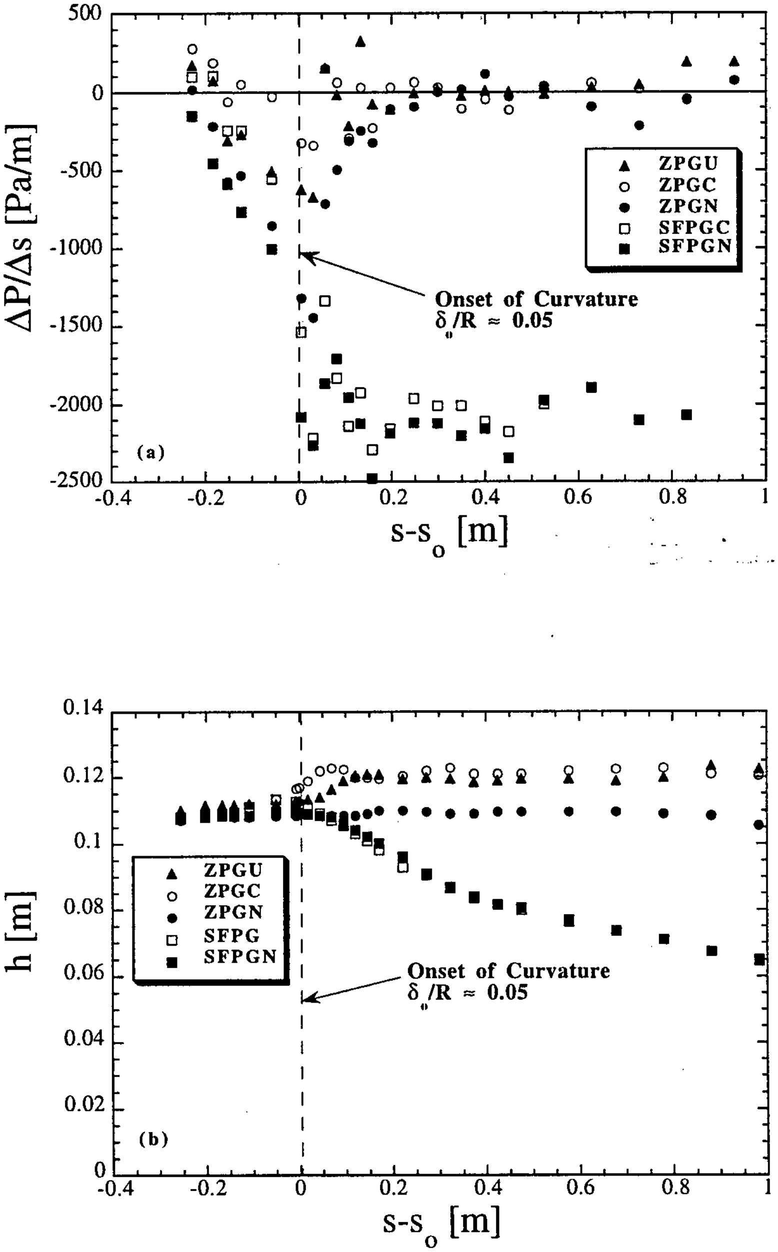

Figure 4.1 Distributions of (a) pressure gradient and (b) wall shape for flow over a convex wall with moderate curvature

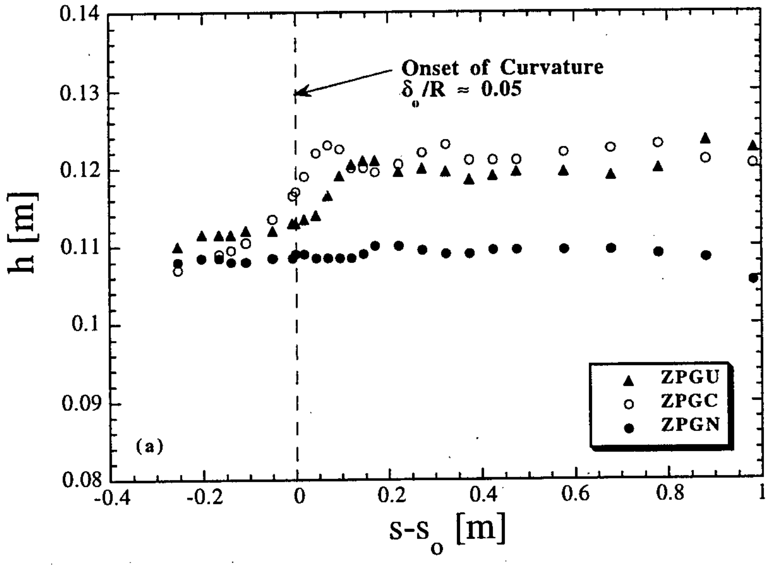

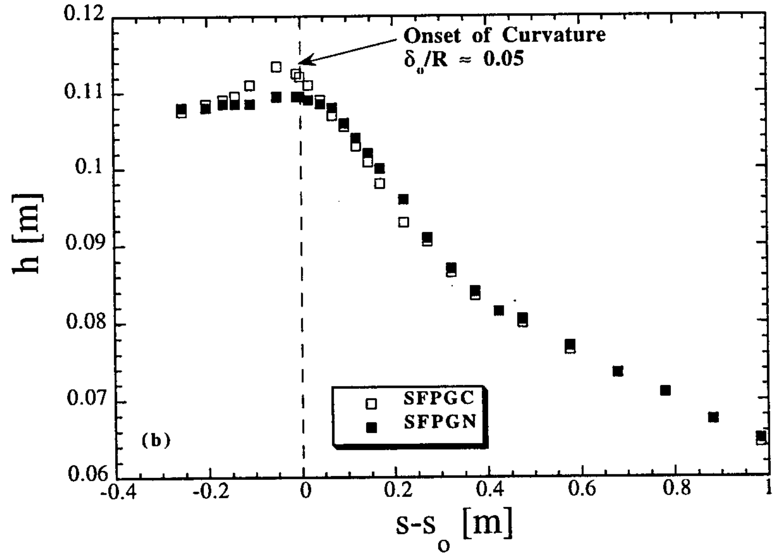

Figure 4.2 Wall contours for (a) zero pressure gradient cases and (b) strong favorable pressure gradients for flow over a convex wall with moderate curvature

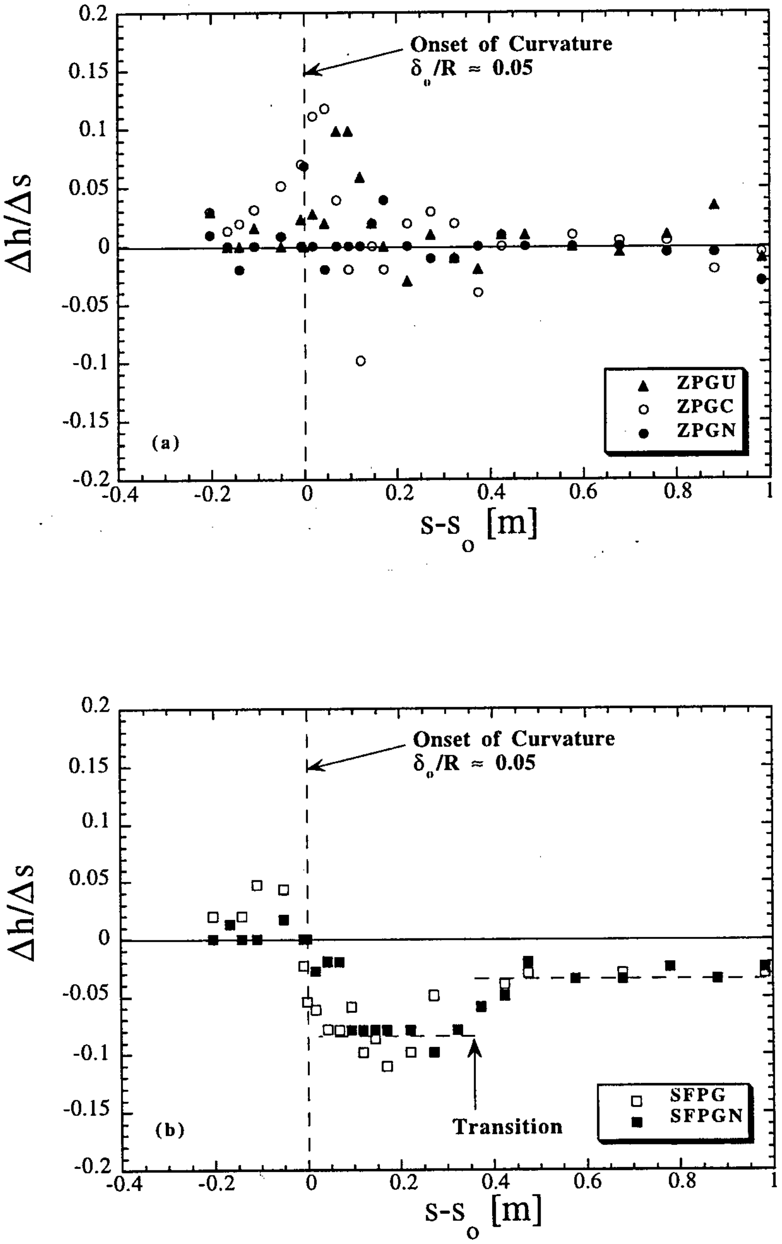

Figure 4.3 Wall slopes for (a) zero pressure gradient cases and (b) strong favorable pressure gradients for flow over a convex wall with moderate curvature

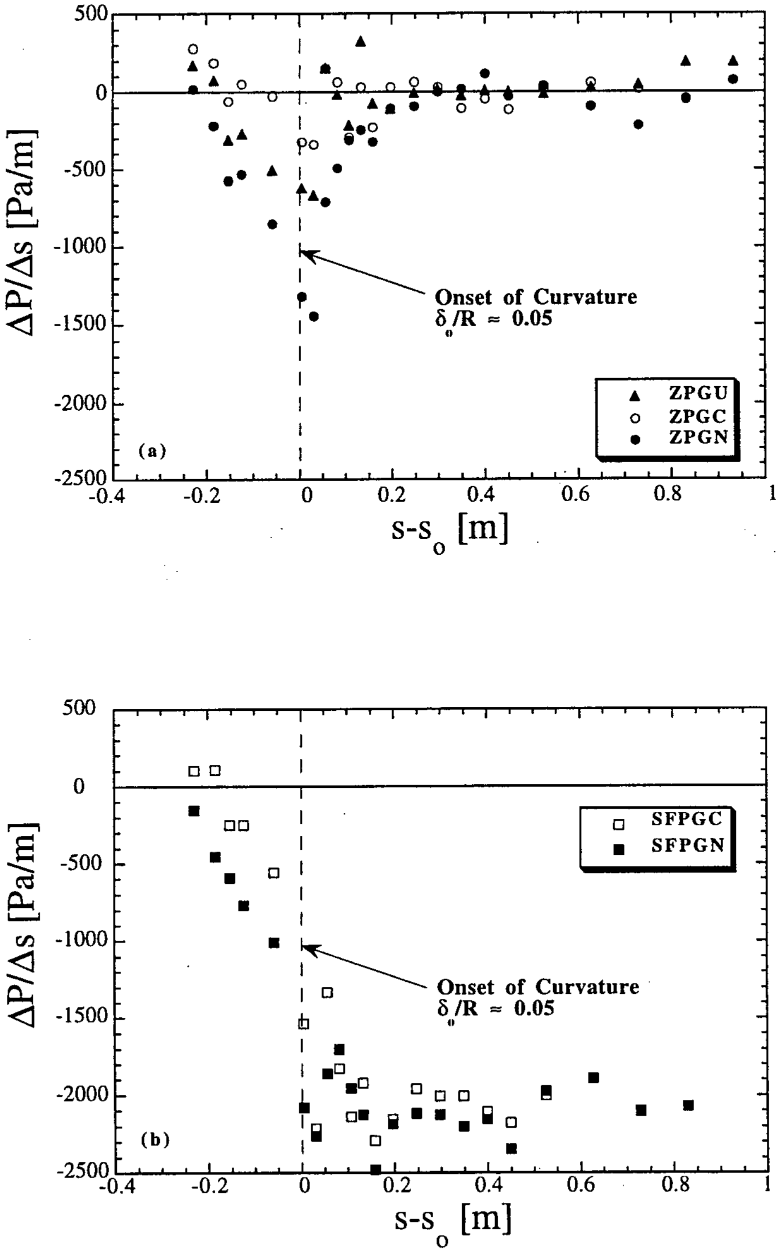

Figure 4.4 Streamwise pressure gradients for (a) zero pressure gradient cases and (b) strong favorable pressure gradients for flow over a convex wall with moderate curvature

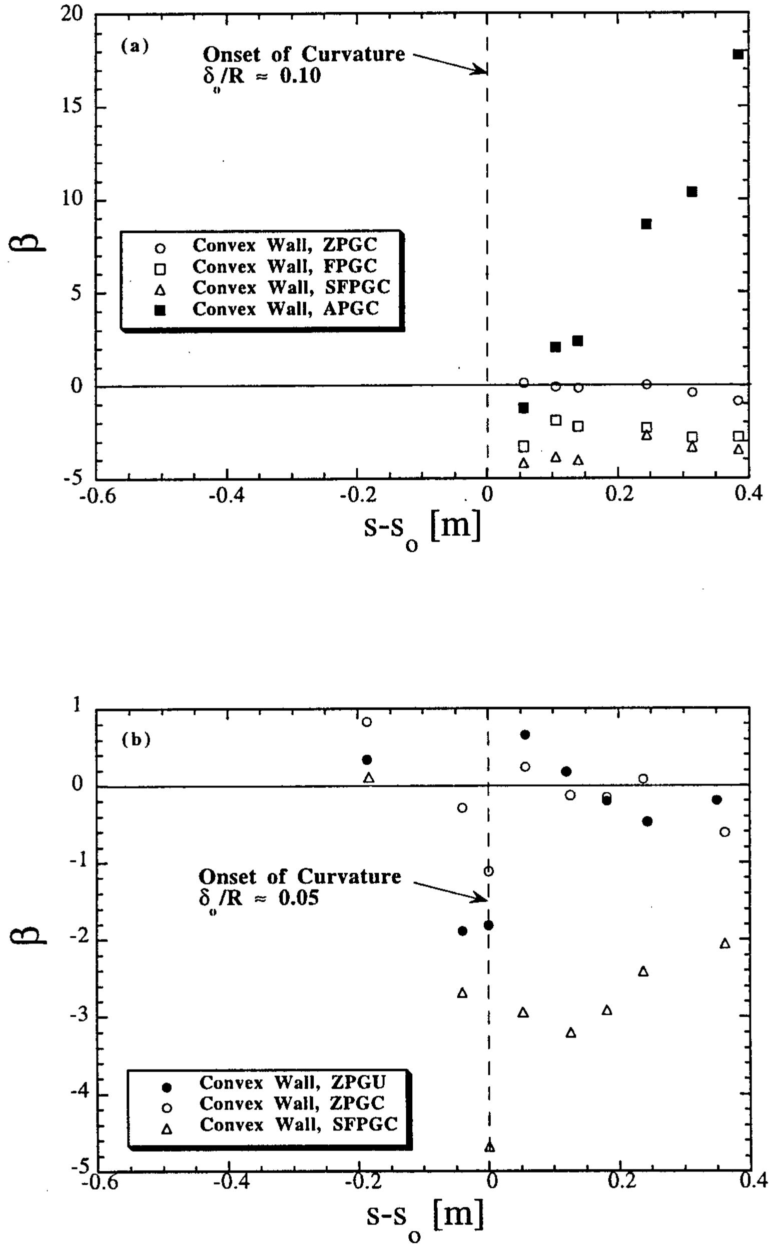

Figure 4.5 Clauser equilibrium parameter for (a) zero pressure gradient cases and (b) strong favorable pressure gradients for flow over a convex wall with moderate curvature

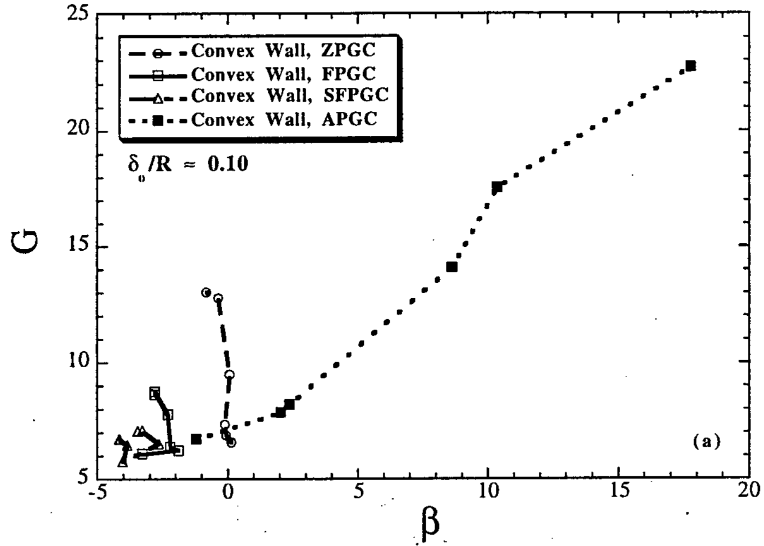

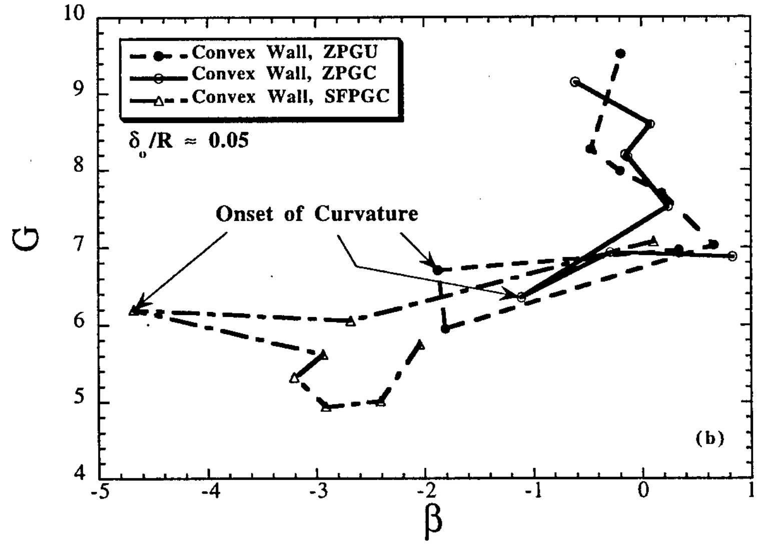

Figure 4.6 Pressure gradient trajectories for (a) zero pressure gradient cases and (b) strong favorable pressure gradients for flow over a convex wall with moderate curvature

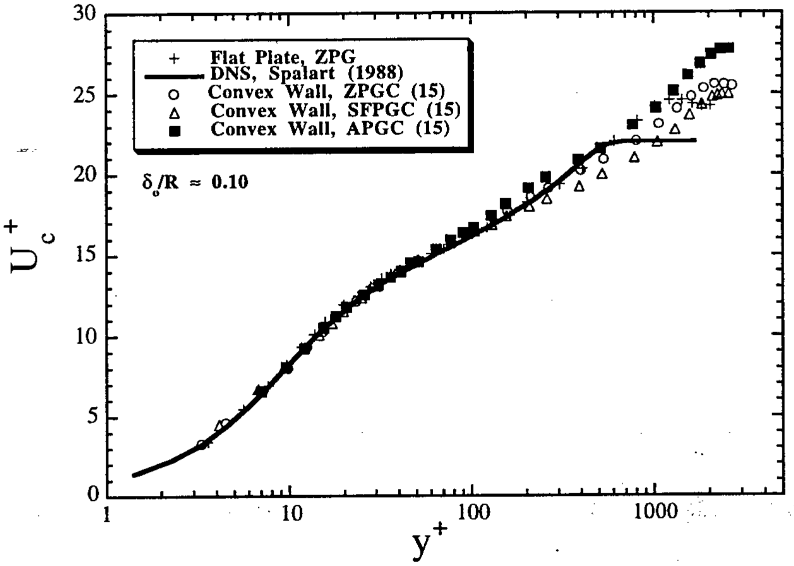

Figure 4.7 Mean streamwise velocity profiles for TS2 under different streamwise pressure gradient conditions at $\alpha \approx 15^{\circ}$

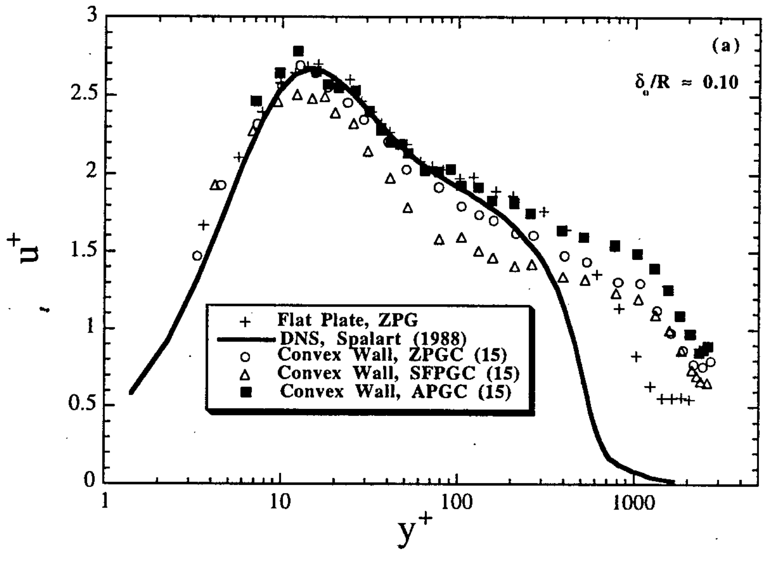

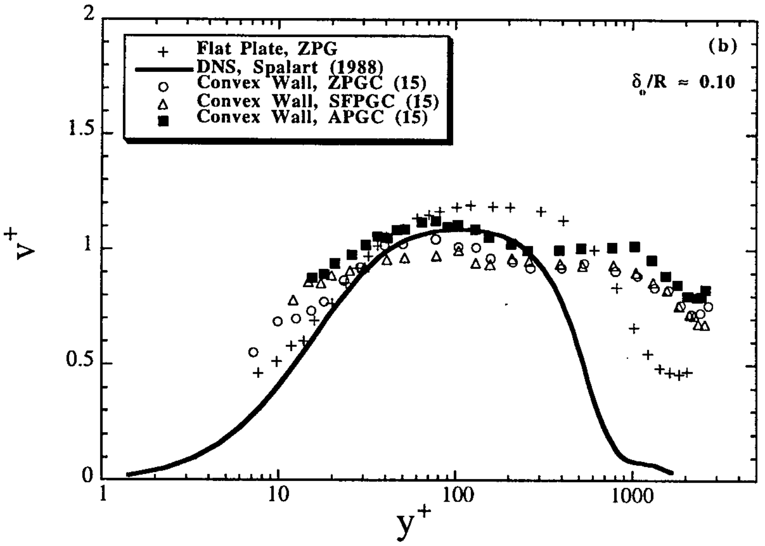

Figure 4.8 Profiles of RMS (a) streamwise and (b) wall-normal velocity for TS2 under different streamwise pressure gradient conditions at $\alpha \approx 15^{0}$

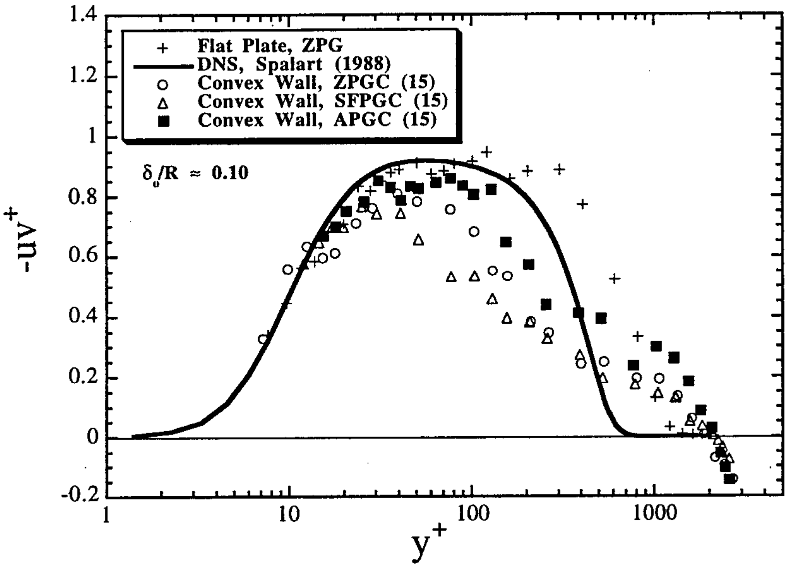

Figure 4.9 Primary Reynolds shear stress profiles for TS2 under different streamwise pressure gradient conditions at $\alpha \approx 15^0$

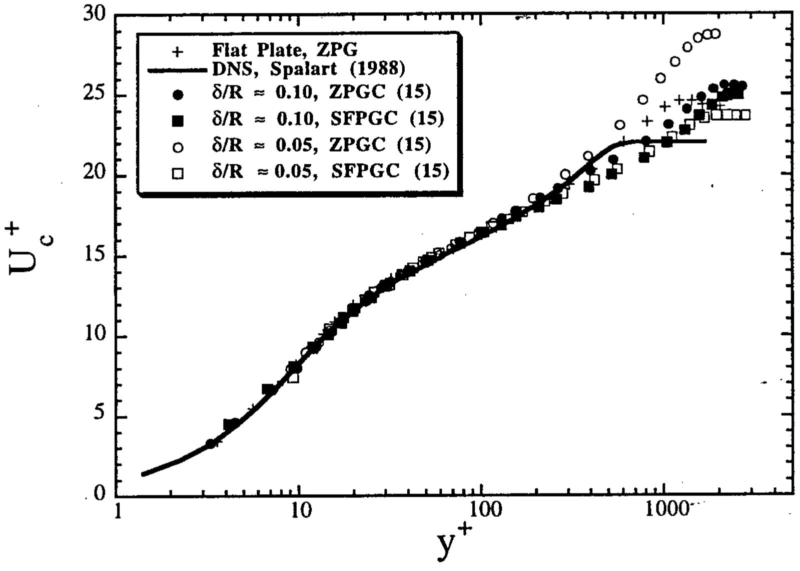

Figure 4.10 Mean streamwise velocity profiles for TS1 and TS2 under different streamwise pressure gradient conditions at $\alpha \approx 15^{o}$

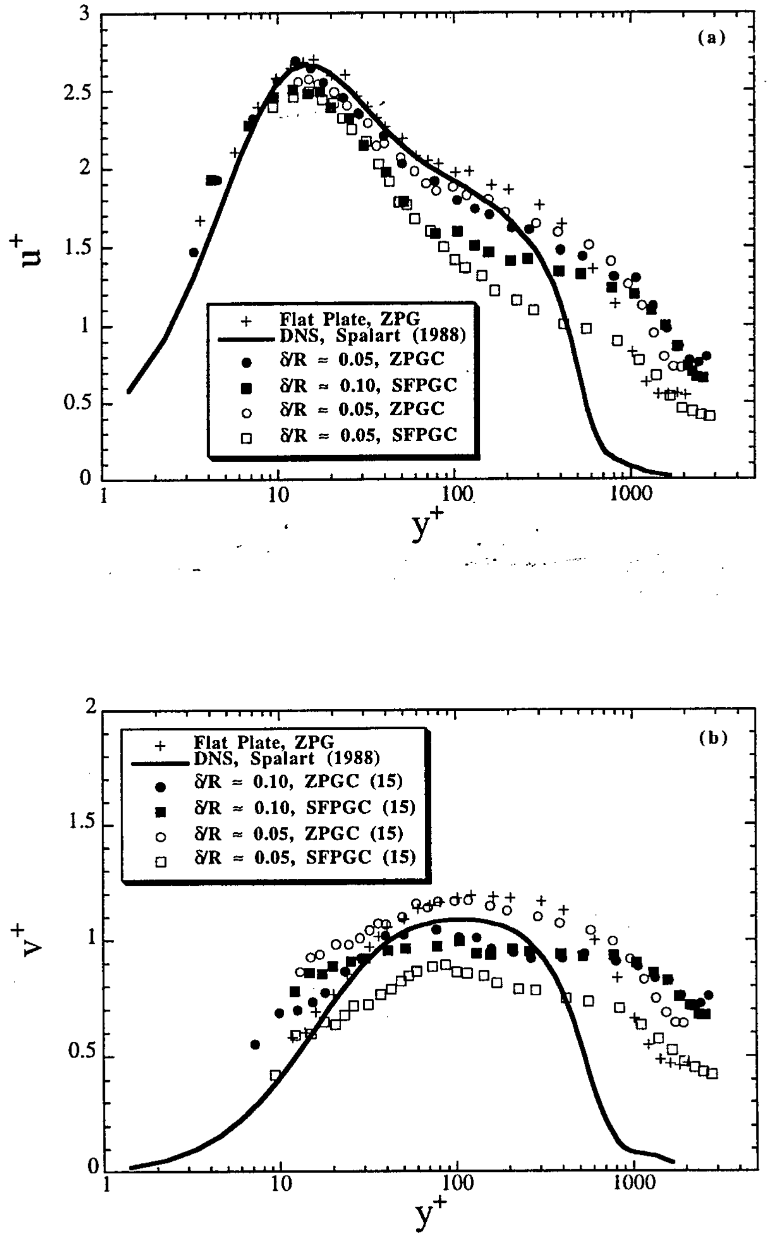

Figure 4.11 Profiles of RMS (a) streamwise and (b) wall-normal velocity for TS1 and TS2 under different streamwise pressure gradient conditions at $\alpha \approx 15^{o}$

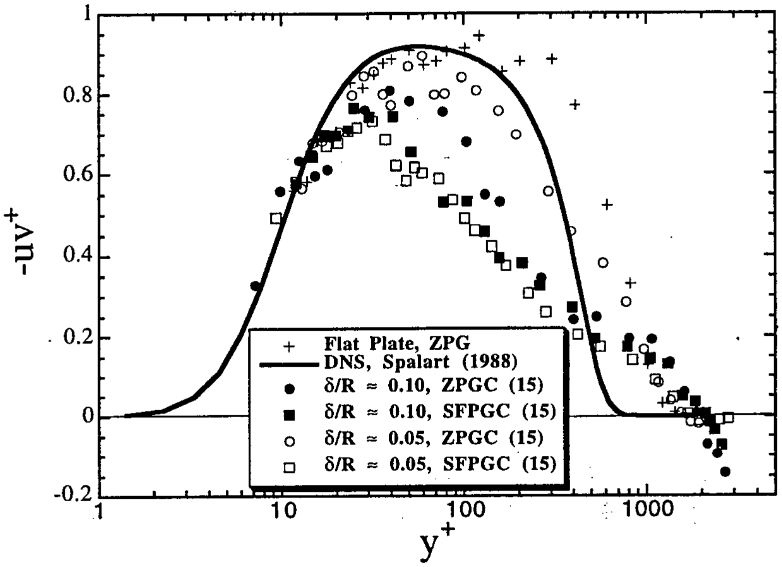

Figure 4.12 Primary Reynolds shear stress profiles for TS1 and TS2 under different streamwise pressure gradient conditions at $\alpha \approx 15^{\circ}$

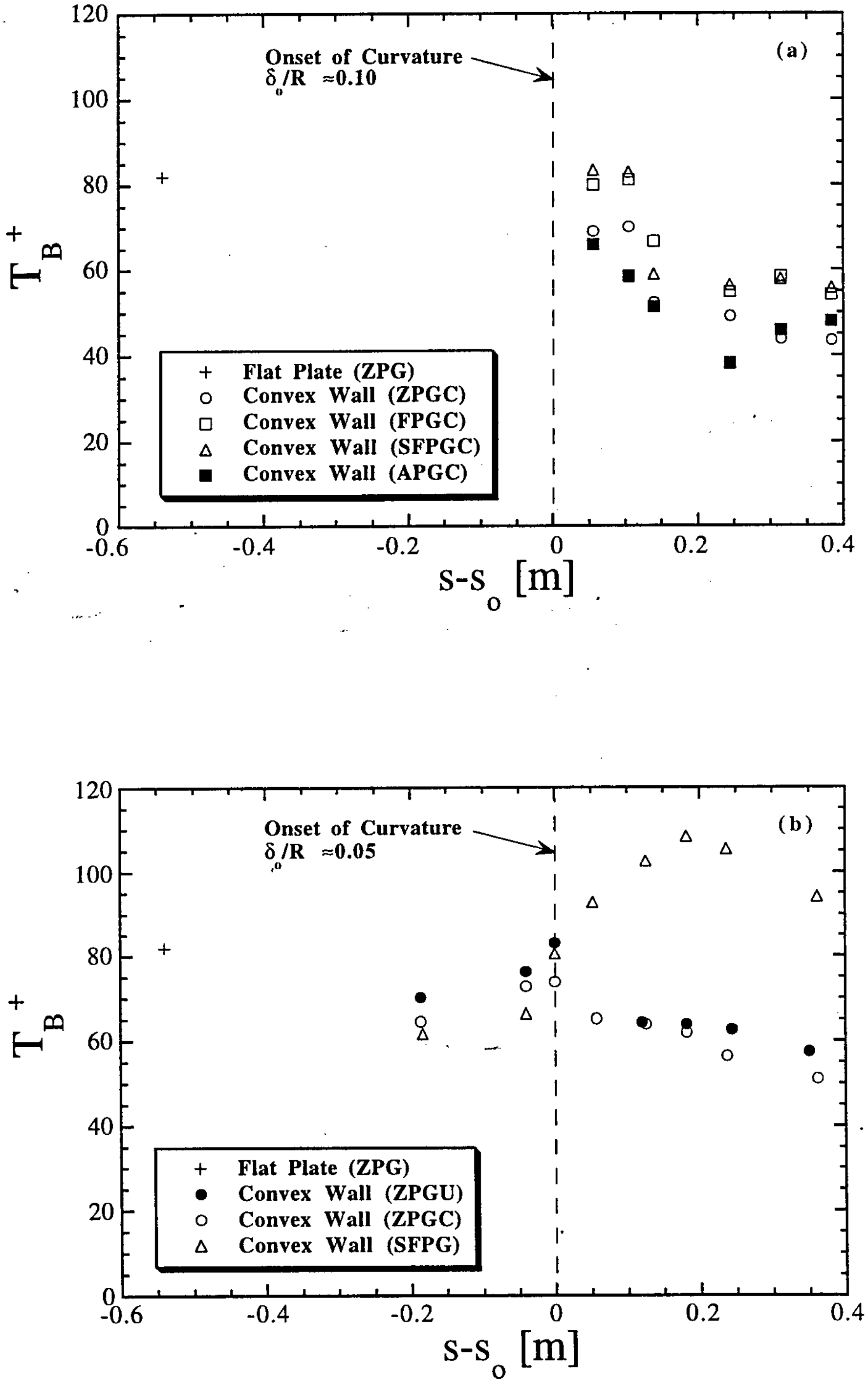

Figure 4.13 Streamwise distribution of inner normalized burst period for (a) TS1 and (b) TS2 under different streamwise pressure conditions

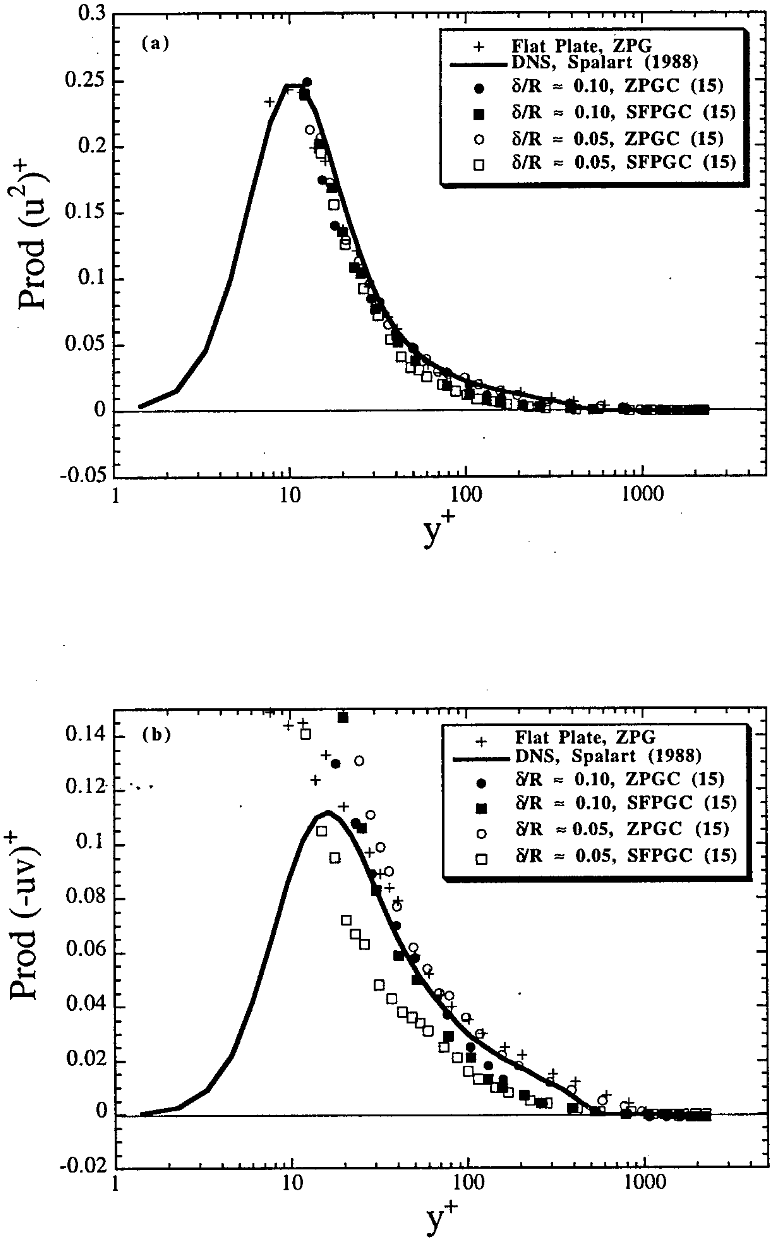

Figure 4.14 Production of (a) normal and (b) primary shear Reynolds stress for TS1 and TS2 under different streamwise pressure conditions

CHAPTER 5. APPLIED STRAIN RATE EFFECTS

5.1 Combined Strain Rate Effects on Skin-Friction Coefficient

To further examine the effect of combined strain rates on the turbulence structure, correlations between a standard integral parameter (i.e. wall-shear stress or skin-friction coefficient, c_f) and the bursting period were examined. These parameters were chosen because c_f depends upon the wall shear stress, $\tau_w = \mu\, \partial\overline{U}/\partial y|_{y=0}$, which is affected by extra strain rates, i.e. $-\overline{U}/R$ and $\partial\overline{U}/\partial s$.

In Figures 5.1 through 5.3, the time between bursts (normalized using inner and outer variables) as a function of the skin-friction coefficient are shown for all applied streamwise pressure gradients and curvatures, i.e. both curvature cases (TS1 and TS2) and all streamwise pressure gradients. The inner and outer normalized burst period are defined as follows:

$$T_{B,in} = T_B^+ = \frac{\overline{T_B}\, u_\tau^2}{\nu} \tag{5.1}$$

$$T_{B,out} = \frac{\overline{T_B}\, U_e}{\theta} \tag{5.2}$$

A Buckingham-Pi analysis (Fox and Mc Donald, 1985) was performed to determine non-dimensional grouping. Evaluating the Π groups for $c_f = f(U_e, \theta, \rho, \overline{T_B}, \mu, \delta^*)$ with U_e, θ, and ρ as the primary dimensions leads to the following relation:

$$\Pi_1 = \frac{\tau_w}{0.5\, \rho U_e^2} = f\left(\frac{\overline{T_B}\, U_e}{\theta}, \frac{\mu}{\rho U_e \theta}, \frac{\delta^*}{\theta}\right) \tag{5.3}$$

or

$$c_f = f\left(T_{B,out}, Re_\theta^{-1}, H\right) \tag{5.4}$$

Equation 5.4 shows that the skin-friction coefficient changes proportionally to the outer normalized burst period as well as the shape factor, and it is inversely proportional to the momentum thickness Reynolds number. A similar exercise was repeated using a inner region velocity and length scale, i.e. u_τ and u_τ^2/ν, to show that the skin-friction coefficient also scales with inner-normalized bursting period ($T_{B,in}$).

In Figures 5.1 and 5.2 the skin-friction coefficient is shown as a function of the inner (Figure 5.1) and outer (Figure 5.2) normalized burst period for the strong (TS1) and moderate (TS2) convex curvature case. In all cases, the general trend is a monotonic increase in the skin-friction coefficient with increasing burst period. Generally, an increase in the bursting period is also accompanied by a decrease in the ejection duration, as mentioned in chapter 4. These observations imply that the skin friction becomes elevated as the turbulence production cycle (TPC) is reduced. At a first glance, this is perhaps surprising because it is expected that an increase of the burst period is associated with a more stabilized boundary layer. However, the elevation in the skin friction is associated with a turbulent boundary layer that undergoes streamwise acceleration, which has a stabilizing effect on the turbulence production. In Figure 5.3, results for both test sections are combined. These results show how the skin-friction coefficient is directly related the bursting period for all strain rate cases, independent of whether the burst period is normalized using inner or outer variables. Two data points, which correspond to the most downstream APG data ($\alpha \approx 45^{\circ}$ and 55°) for TS1, clearly fall outside of the general trends observed, which can be attributed to the boundary layer being far away from equilibrium conditions as seen in the previous chapter. It was shown in this section that the skin-friction coefficient is simply coupled to the burst period for a complex turbulent boundary layer.

5.2 Strain Rate and Reynolds Stress Tensor Principal Axes

As pointed out in chapter 1, Spalart and Shur (1997) proposed an eddy-viscosity turbulence model that accounts for system rotation and streamline curvature. Their proposal of a Galilean-invariant quantity to dispose of $-\overline{U}/r$ led to an expression for the Lagrangian derivative of the angle of the strain rate principal axis, α_{SR} (Equation 5.5). In this section, the principal axes angles for both the strain rate tensor and the Reynolds tensor, α_{ReS}, are presented to examine the Spalart and Shur (1997) model. The equations for the principal axes angles for a two-dimensional flow are:

$$\alpha_{SR} = \frac{1}{2} \operatorname{atan}\left[\frac{-2\, S_{sn}}{S_{nn} - S_{ss}}\right] \tag{5.5}$$

$$\alpha_{ReS} = -\frac{1}{2} \operatorname{atan}\left[\frac{-2\, \overline{uv}}{\overline{u^2} - \overline{v^2}}\right] \tag{5.6}$$

The wall-normal diagonal strain rate component was determined from the measurements of the wall-normal velocity, $\overline{V}$, whereas the streamwise diagonal strain rate component was inferred using the continuity equation for (s,n) coordinate system according to

$$\frac{\partial \overline{U}}{\partial s} \approx -\frac{\partial}{\partial n}\left[\overline{V}\left(1 + \frac{n}{R}\right)\right] \tag{5.7}$$

In this approximation, the spanwise derivative of the z-component of the mean velocity ($\overline{W}$) was neglected. As discussed in chapter 3 and shown in Table 3.2, it was reasonable to assume locally two-dimensional flow.

In Figure 5.4, the principal axes for the strain rate and the Reynolds stress tensor are shown for the same data sets discussed in chapter 4.3.2 to illustrate the effect of different strain rate ratios on the structural features of the boundary layer. For a plane constant shear, the principal axis is $\alpha_{SR} = 45^{\circ}$, but the principal axes of the Reynolds stress tensor are not aligned with those of the strain rate tensor for non-homogeneous turbulence (Gence and Mathieu, 1979). In Figure 5.4a, no major trends are apparent in the wall-normal profile of the strain rate tensor principal axes. The high "noise" level in the data is due to uncertainties that arise from evaluating the different strain rate tensor components, especially the normal components S_{ss} and S_{nn}.

The angle of the principal axes of the Reynolds stresses can be interpreted as an indirect measure for how well the velocity fluctuations in the streamwise and wall-normal direction are correlated with each other, and also the degree to which the flow is locally isotropic, i.e. $\overline{u^2} - \overline{v^2} \Rightarrow 0$. Both trends would increase the magnitude of the Reynolds stress principal axes. The Reynolds stress principal axes angle, α_{ReS} shown in Figure 5.4b is unaffected by the interacting strain rates inside the log-law region ($y^+ \leq 100$). In the outer portion of the TBL, the ZPGC case with strong convex curvature (TS1) shows the largest reduction of α_{ReS} relative to flat plate values. This behavior is consistent with the highest local application rate of newly introduced strain rates especially in the streamwise direction (Figure 3.1). The strain rate and Reynolds stress orientation results imply the violation of the Boussinesq approximation, which requires the principal axes of these tensors to be aligned. One of the major shortcomings of standard turbulence models (e.g. k-ε model) is the use of an isotropic scalar eddy viscosity.

To demonstrate the behavior of α_{ReS} further, its streamwise evolution immediately downstream of the onset of curvature for ZPGC and SFPGC in TS2 is shown in Figure 5.5. Here, the angle of the principal Reynolds shear stress tensor axes is immediately suppressed for the ZPGC case (Figure 5.5a), but remains essentially unchanged for the SFPGC case. The same trend for a zero pressure gradient turbulent boundary layer forming over a convex wall has been predicted by Hong and Murthy (1986), who developed the Large Eddy Interaction Model (LEIM), a finite velocity transport approach which is an alternative to the more frequently used simple gradient diffusion hypothesis. They found that the angle of the principal axes of the stress decreased with convex curvature. As before, the TBL for the ZPGC case is exposed to a *rapidly* changing application rate of streamwise acceleration / deceleration causing α_{ReS} to be reduced. These results demonstrate that the rate of application of the newly applied strain rates is as least as important as the magnitude of the strain rates itself.

5.3 Total Combined Strain

The concept of total or combined effective strain rates has been investigated in the past (cf. Maxey, 1982; and Sreenivasan, 1985). Sreenivasan (1985) suggests that the turbulence structure at any given stage is completely determined by the local value of the total strain parameter

$$\beta_{TSt} = \int_0^{T_E} \left(\frac{\partial \overline{U}}{\partial y} \right) dt \qquad (5.8)$$

if the applied mean shear is sufficiently large. Here T_E is the typical lifetime of the large eddy (also eddy turnover time) which is on the order of $1/3\,\overline{q^2}/\varepsilon$ in equilibrium. Hence, the large-eddy lifetime can be viewed as the ratio of the turbulent kinetic energy to the isotropic turbulent dissipation rate. This quantity is essential identical to what Bradshaw (1973) denoted as the memory time in Equation 4.1 (divided by the convection velocity, $\overline{U}$). Note that this approach is strictly correct only for equilibrium flows. For the two-component data, an estimate for the total strain parameter can be found by expressing the large eddy lifetime in terms of measured quantities according to

$$T_E \approx \frac{1}{2}\frac{\overline{u^2}+\overline{v^2}}{-\overline{uv}\left(\partial\overline{U}/\partial y\right)} \tag{5.9}$$

for a flat plate boundary layer, and

$$T_{E,rad} \approx \frac{1}{2}\frac{\overline{u^2}+\overline{v^2}}{-\overline{uv}\left(\partial\overline{U}/\partial y-\overline{U}/r\right)} \tag{5.10}$$

for flow over convex wall. Hence, the local total strain parameter can be calculated from

$$\beta_{TSt} \approx T_E\frac{\partial\overline{U}}{\partial y} \approx \frac{1}{2}\frac{\overline{u^2}+\overline{v^2}}{-\overline{uv}} \tag{5.11}$$

and

$$\beta_{TSt,rad} \approx T_{E,rad}\frac{\partial\overline{U}}{\partial y} \approx \frac{1}{2}\frac{\overline{u^2}+\overline{v^2}}{-\overline{uv}}\frac{1}{1-S_{rad}} \tag{5.12}$$

respectively, where $S_{rad}=\dfrac{\overline{U}/r}{\partial\overline{U}/\partial y}$ is the curvature strain rate ratio. The total strain parameter can also be interpreted as the ratio of the large-eddy lifetime to a distortion time scale. This ratio is a useful measure to determine whether or not the flow should be treated as a rapidly distorted flow. In rapid distortion theory (RDT), the governing equations can be linearized under the assumptions that the turbulence is weak ($u' << \overline{U}$) and that the distortion time is far less than a typical integral time scale, or in other words, $\beta_{TSt} >> 1$ (see Savill, 1987).

In Figure 5.6, the estimated total strain parameter is shown as a function of the inner normalized wall-normal coordinate for the initial region in TS2 under ZPGC (Figure 5.6a) and SFPGC (Figure 5.6b) conditions. The profiles for the flat plate and the DNS data sets are included for comparison. There is good agreement between all data sets for the inner, near-wall region, as seen previously. Outside the log-law region ($y^+ \geq 100$), the total strain parameter becomes elevated as soon as the flow enters the curved portion of the test section. This trend is independent of the applied streamwise strain rate.

In order to gain a better understanding, the streamwise variation of the total strain parameter in the outer portion of the boundary layer ($y/\delta \approx 0.4$ as suggested by Sreenivasan, 1985) is examined. Figure 5.7 shows the streamwise development under different conditions, i.e. moderate convex curvature (TS1) with different streamwise pressure gradient in Figure 5.7a, and both curvature cases with zero, favorable and adverse (only for TS1) streamwise pressure gradients in Figure 5.7b. The trends are striking. For both curvature cases, the total strain parameter is elevated immediately downstream of the onset of curvature, relative to the flat plate values. Note that the equilibrium value for homogeneous plane shear flow is approximately 4.5 (see Sreenivasan, 1985). However, this value is magnified by approximately a factor of 4 for the strong curvature case. It is still questionable whether or not the flow reaches a new, higher total strain parameter (approximately 5.5 for TS2 and 13.0 for TS1), especially in the case of strong convex curvature. This information would be valuable in assessing the modified turbulence structure for curved boundary layer flows.

The following interpretation of these results is proposed. The nonlinear cascade process describes the interaction of the different size eddies, where it is assumed that the large, energy-containing eddies lose their energy to somewhat smaller eddies, which in turn lose their energy to still smaller eddies all the way down to the smallest scale eddies, which finally dissipate the energy by viscous interaction. It is this last stage that is described by the isotropic dissipation rate ε, which is an integral part of a variety of turbulent models (see van den Berg, 1984). However, the rate of dissipation is determined by the first few stages of the cascade process, i.e. by the large eddies. In addition, the effectiveness at which the large eddies extract energy from the mean shear flow is believed to be linked to how well the principal axes of vorticity is aligned with that of the mean strain rate

(Tennekes and Lumley, 1972). Any mechanism that would suppress or even inhibit the initial stage in the nonlinear cascade process, or any mechanism that would affect the dynamic interaction between the turbulence and the mean flow, would instantly result in a variation of ε, which would cause the total strain parameter to change.

In a direct numerical simulation (DNS) of an elliptical shear flow by Blaisdell and Shariff (1996), which combines a homogeneous turbulent flow with the effects of solid body rotation and strain, it was found that the nonlinear cascade process was suppressed for early times. This effect was enhanced for stronger rotation, whereas it recovered as the flow field developed further in time. The relationship to the present results is as follows: The newly applied extra rates of strain at the onset of curvature have a significant effect on the turbulence structure of the developing boundary layer. Immediately downstream of the onset of curvature, the turbulence production cycle is inhibited and the total strain parameter is elevated. Equation 5.13 shows how the total strain parameter is related to the TKE and the turbulence dissipation rate.

$$\beta_{\mathrm{TSt}} \propto \frac{k}{\varepsilon}\frac{\partial \overline{U}}{\partial y} \tag{5.13}$$

Since the data show that neither the TKE nor the mean shear rate are significantly altered when the additional strains are imposed, the increase in β results from a reduction of the turbulence dissipation rate ε. This, in turn, implies that either the nonlinear cascade transfer process is inhibited or the dynamic interaction between the turbulence and the mean flow is affected. This behavior can only be caused by the abrupt change in wall curvature, and it was more pronounced for stronger convex curvature.

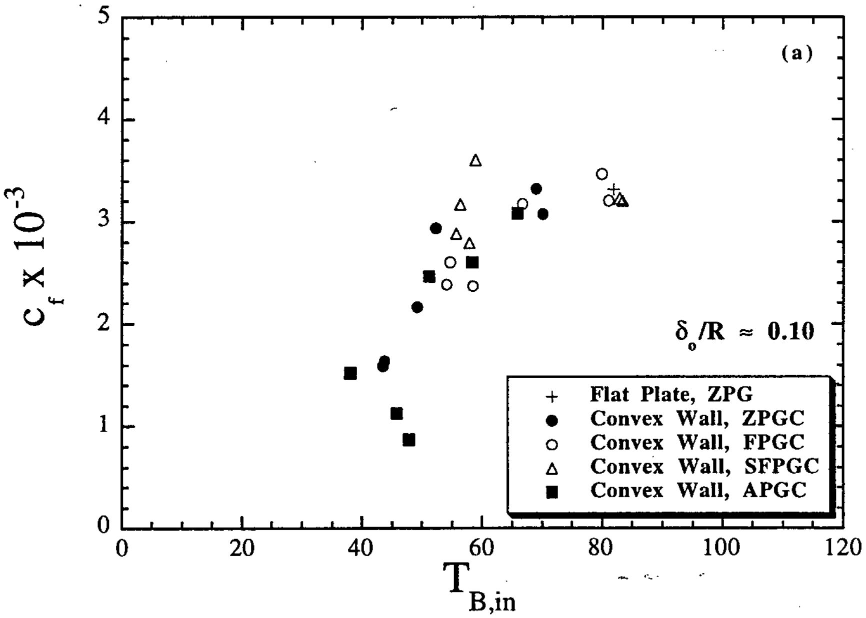

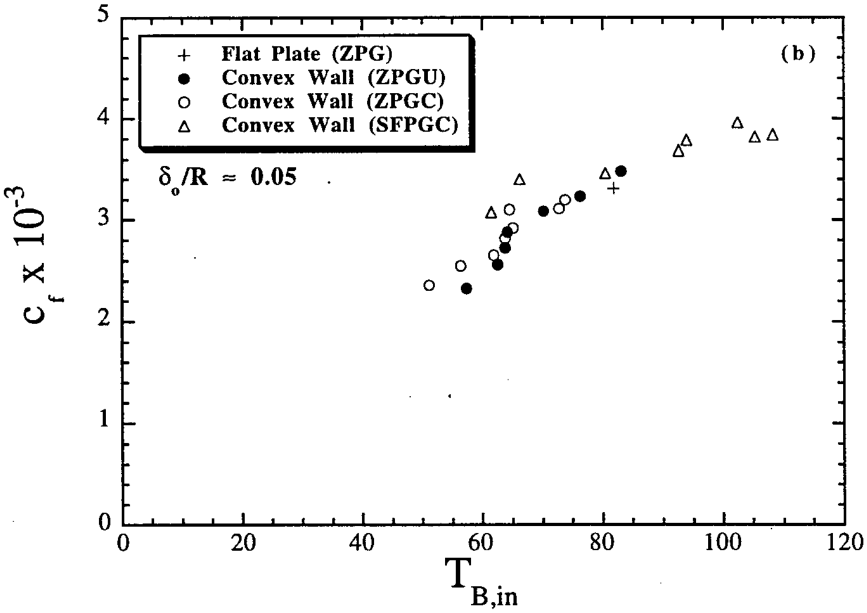

Figure 5.1 Skin-friction coefficient as a function of the inner normalized bursting period for (a) TS1 and (b) TS2

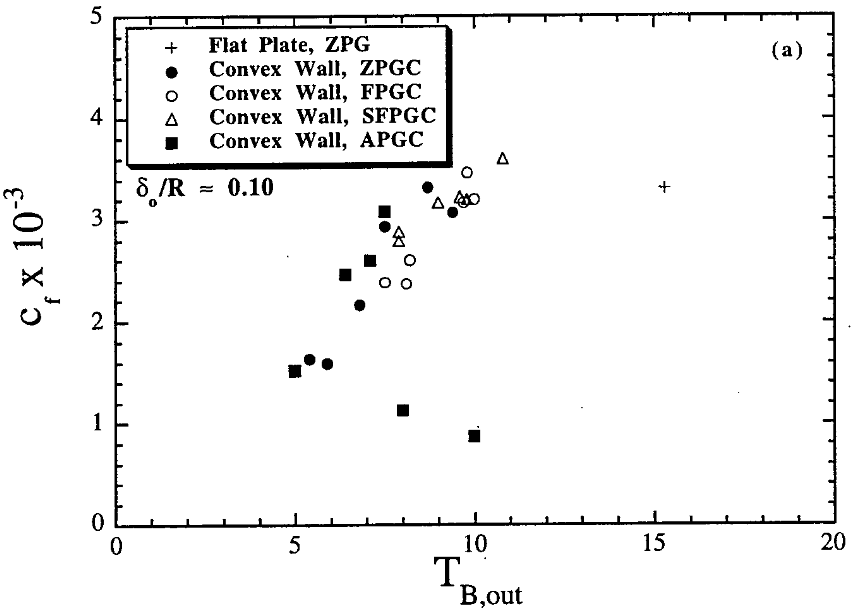

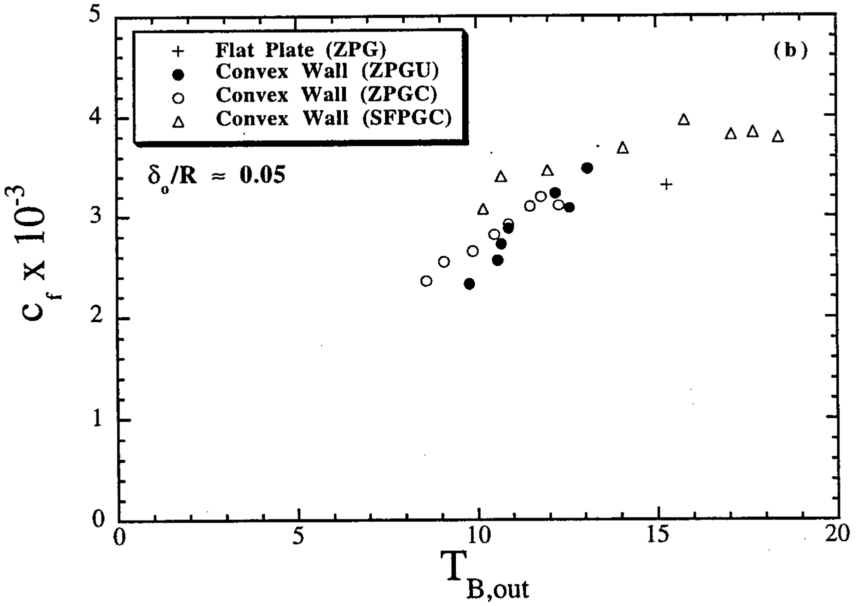

Figure 5.2 Skin-friction coefficient as a function of the outer normalized bursting period for (a) TS1 and (b) TS2

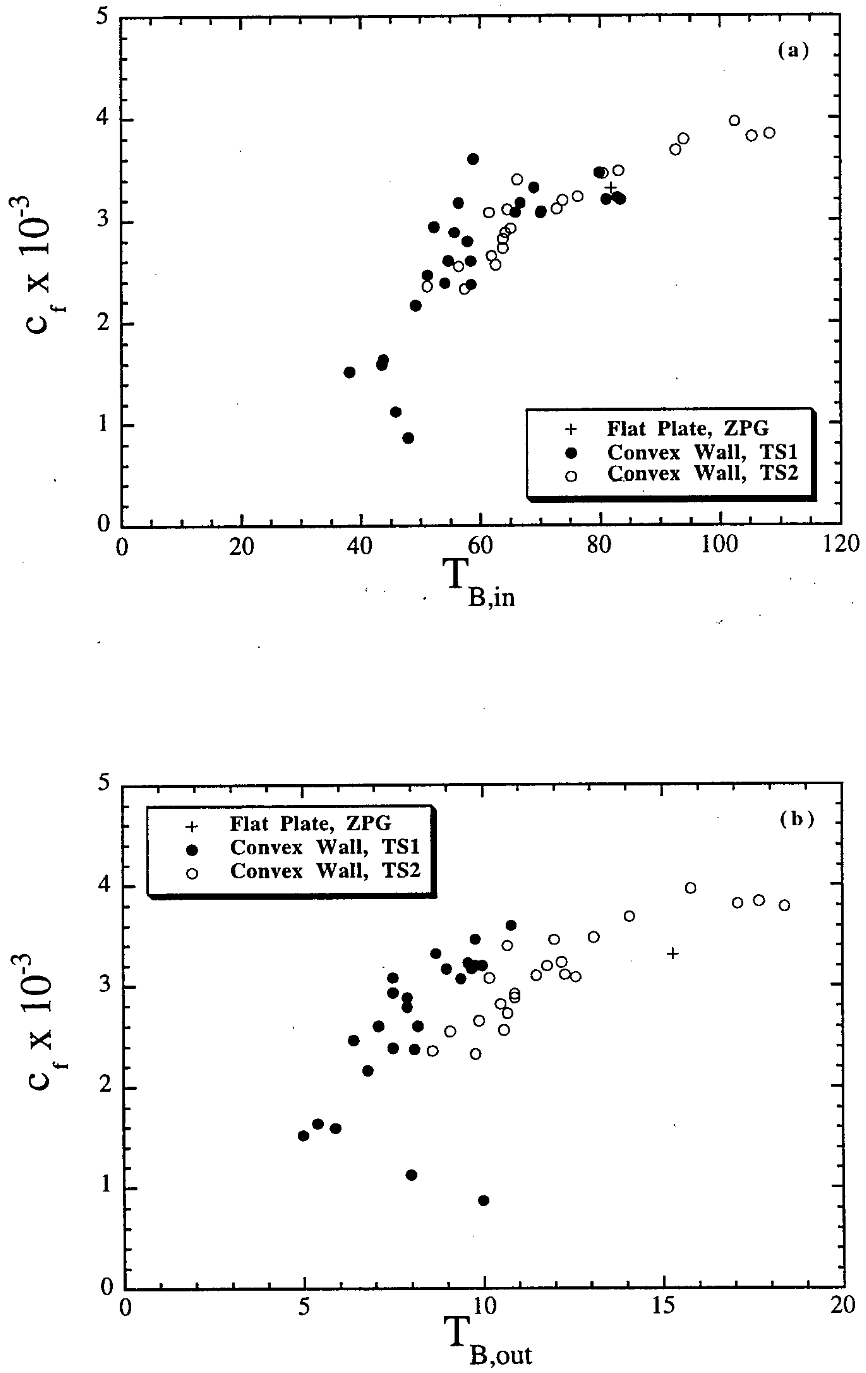

Figure 5.3 Skin-friction coefficient as a function of the (a) inner and (b) outer normalized bursting period for TS1 and TS2

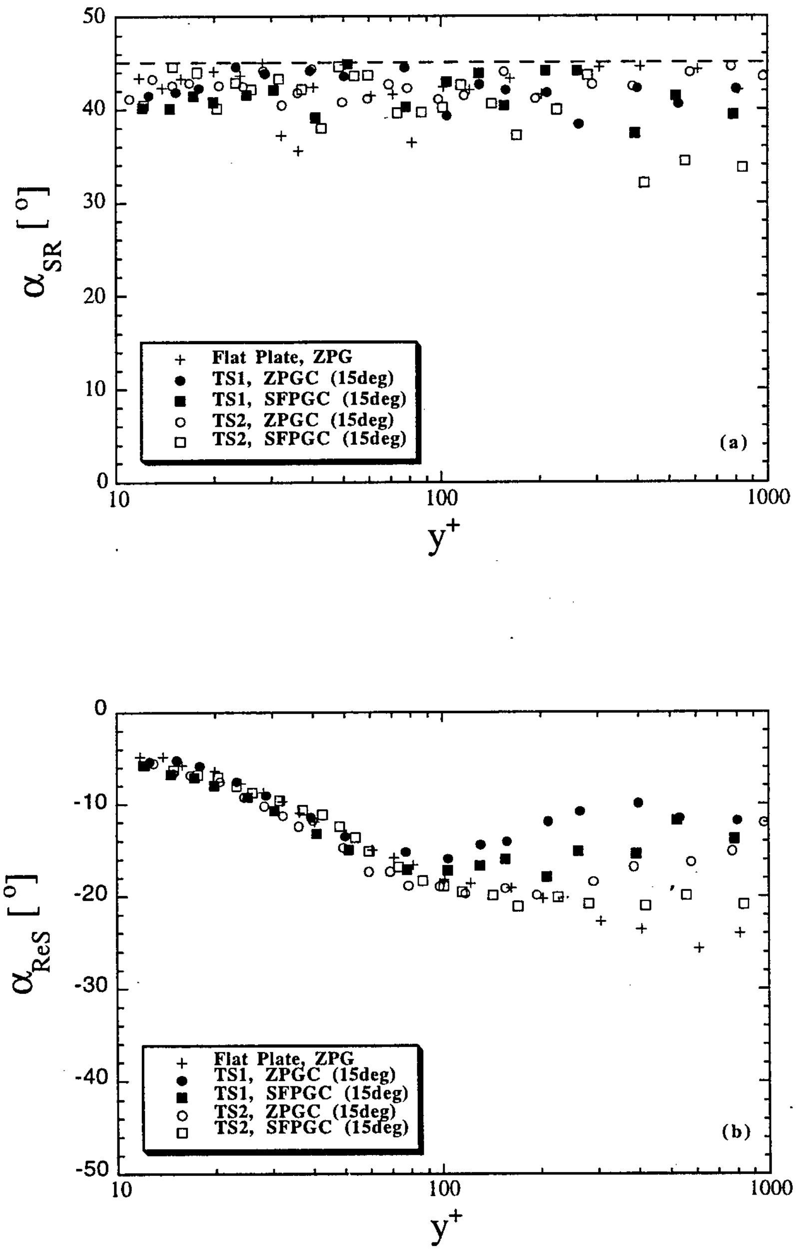

Figure 5.4 Angle of principal axes of (a) the strain rate and (b) Reynolds stress tensor with different pressure gradient ratios

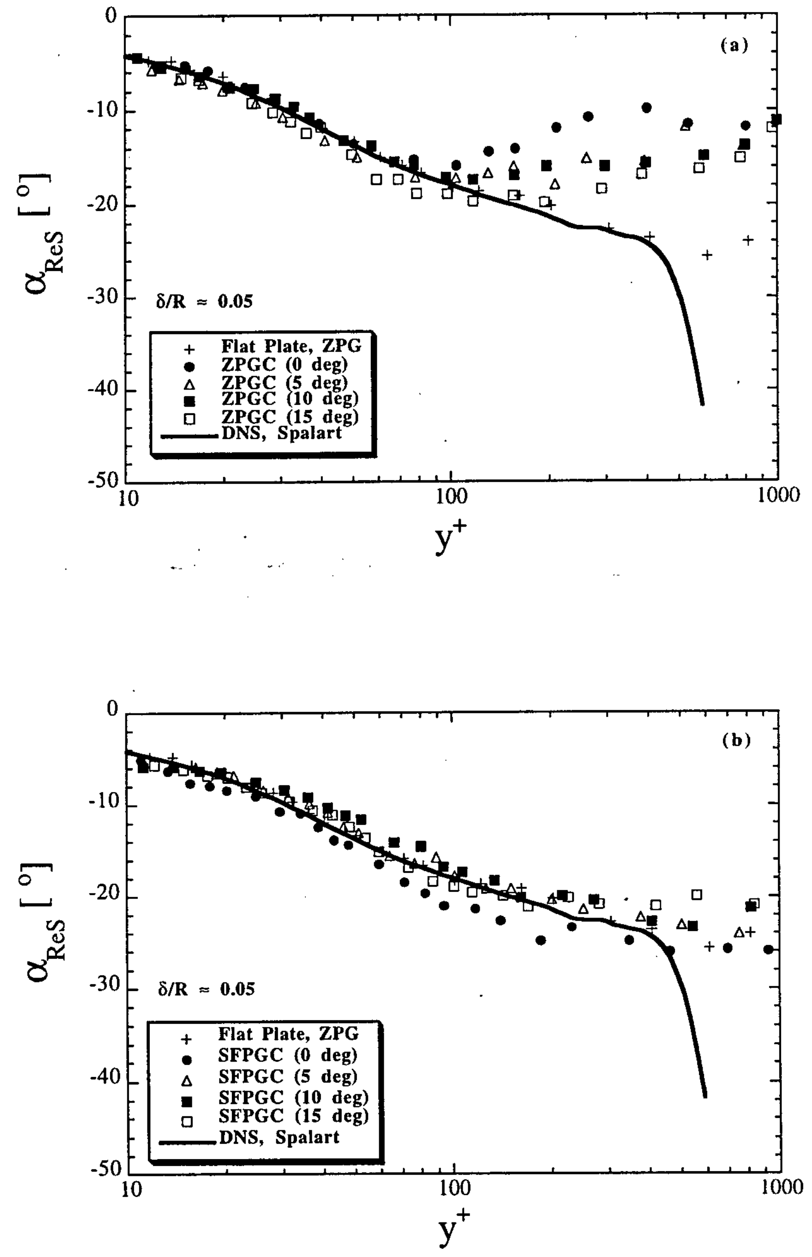

Figure 5.5 Angle of the Reynolds stress tensor principal axes for TBL with (a) compensated zero and (b) strong favorable streamwise pressure gradient

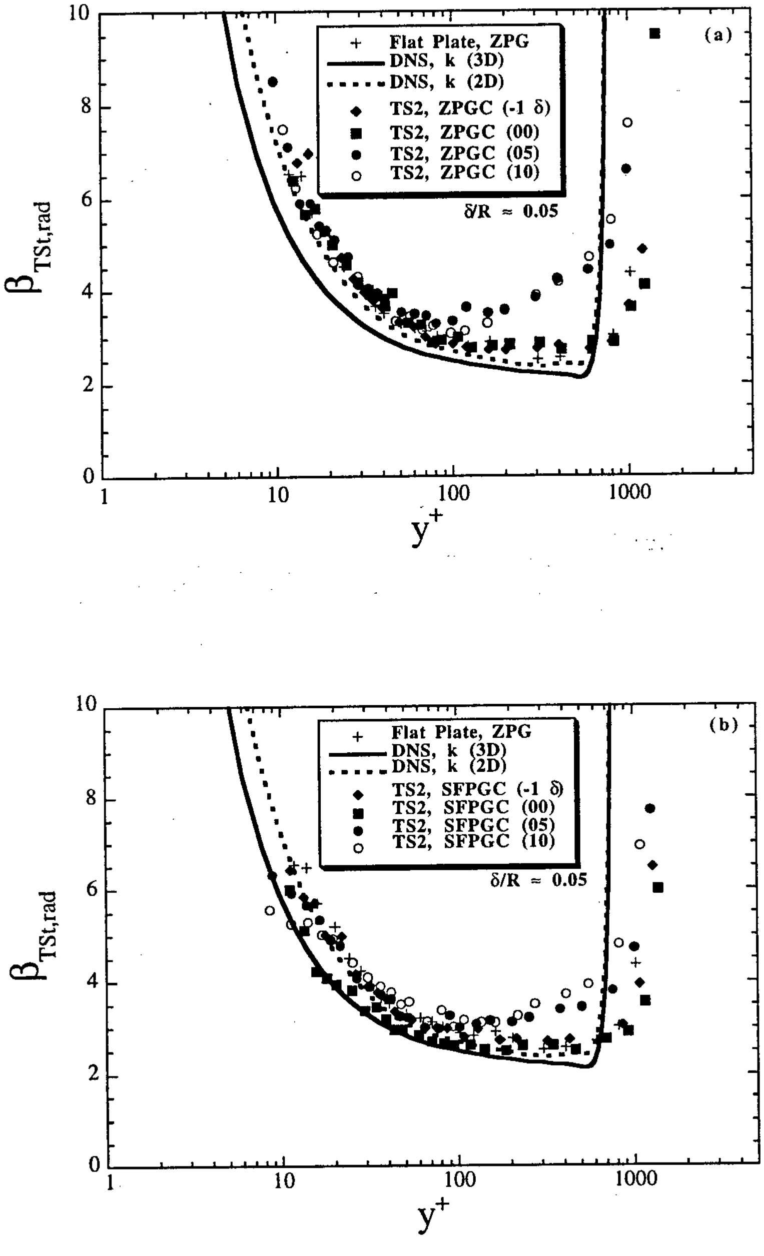

Figure 5.6 Total strain parameter for TBL with (a) compensated zero and (b) strong favorable streamwise pressure gradient for TS2

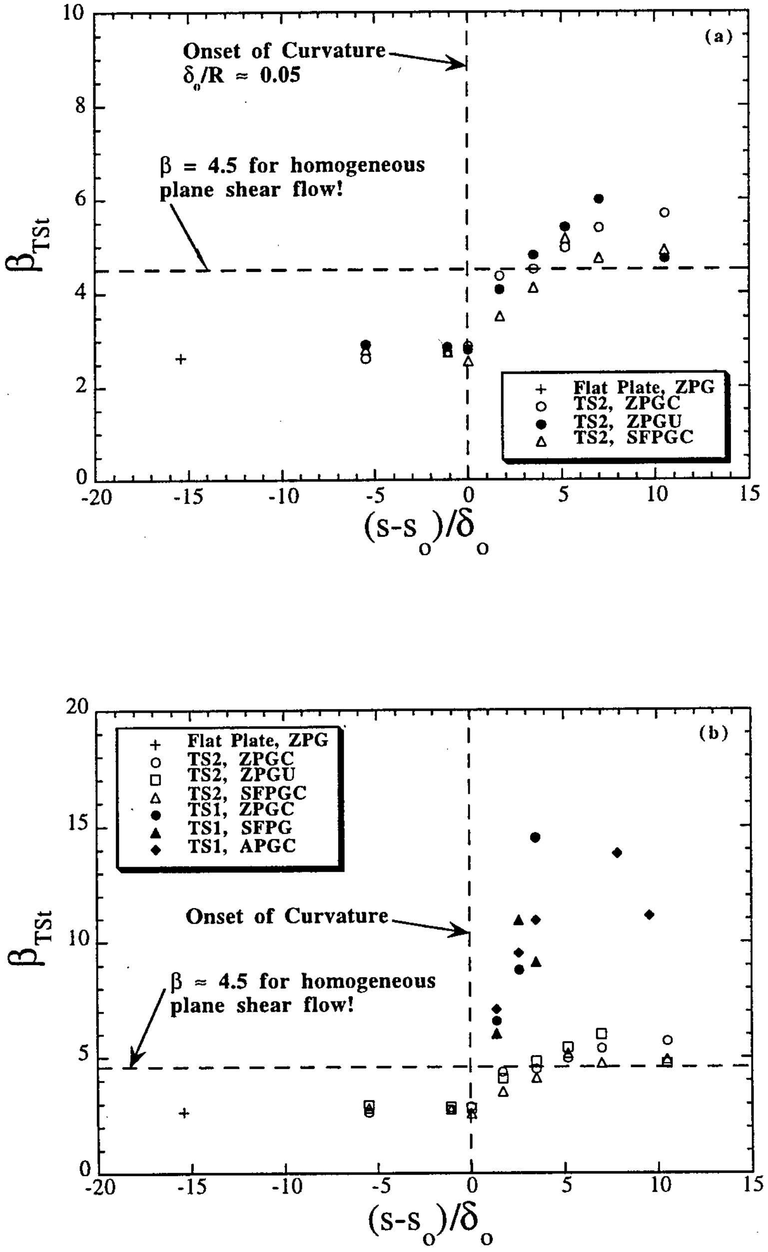

Figure 5.7 Streamwise variation of the total strain parameter for (a) TS2 and (b) TS1 and TS2 combined in the outer portion of the TBL

CHAPTER 6. CONCLUSIONS AND RECOMMENDATIONS

6.1 Conclusions

In this study, detailed measurements have been made and analyzed to examine the response of a turbulent boundary layer to multiple strain rates. The turbulent boundary layer was exposed to multiple, extra rates of strain due to streamline curvature and streamwise pressure gradients. The measurements allowed examination of the entire turbulent production cycle including near-wall region, with the emphasis on whether these additional strains would interact with each other and how the turbulent production cycle would be affected.

It was evident from the results that the two extra strain rates not only interacted with each other, but that their interaction was nonlinear. For the strong curvature case ($\delta_0/R \approx 0.10$), the TBL reached a state of similarity, as inferred from the collapse of the mean and fluctuating velocities for both zero and favorable streamwise pressure gradients. However, in the presence of an adverse pressure gradient, no similarity was achieved. For the moderate curvature case, the TBL had not reached a similarity state at the last measurement station ($\alpha \approx 30^o$).

The outer portion of the boundary layer (outside the log-law region, i.e. $y^+ \geq 100$ for convex TBL) was more strongly affected by the extra applied strain rates than the inner layer. Strictly speaking, physical changes of the near-wall quantities were compensated by the local shear velocity u_τ, whereas variations in the outer portion of the boundary layer were not. Stabilization of the boundary layer turbulence due to convex curvature was augmented by favorable pressure gradient and counteracted by adverse pressure gradient.

The effect of the different interacting strain rates on the turbulence production cycle, which was characterized by the turbulent bursting period, the ejection duration and specific terms in the Reynolds transport equations, was strongest in regions of rapidly changing newly introduced strain rates, i.e. at the onset of curvature. The turbulence production cycle was reduced in regions of locally strong accelerated flow, a trend which was more pronounced for higher pressure gradient ratios, i.e. moderate curvature in combination with strong favorable pressure gradient. The turbulent bursting period can be directly correlated to the skin-friction coefficient as demonstrated by analysis of the relevant non-dimensional

Π groups and supported by the measurements. Using both inner and outer normalization for the burst period successfully implies the importance of both the inner and outer layer in the bursting process.

The energy-containing structures in the turbulent boundary layer were affected immediately downstream of the onset of curvature, i.e. reduction of the Reynolds stress principal axes and increase in the total strain parameter. An increased application rate of the newly introduced extra strain rates (wall-normal and streamwise) resulted in a larger variation of the turbulent bursting period and the total strain parameter. The resulting suppression of the nonlinear cascade process in conjunction with a reduction of the turbulence production cycle emphasizes the importance of the inner / outer layer dynamics.

6.2 Recommendations for Further Studies

It has become clear that the application rate of the newly applied extra rate-of-strain is critical to determine the effects on a turbulent boundary layer. Therefore, it is necessary to carefully define a quantity that adequately represents the different application rates in terms of measurable quantities, e.g. distribution of wall static pressures. Also, additional studies with various step changes in the streamwise pressure gradient that occur simultaneously with the step change in wall curvature or lag/lead the wall curvature change would give a deeper insight into the interaction process between the extra strain rates.

Spectral information of the velocity fluctuations would be a great asset in further investigating the outer layer dynamics of the turbulent boundary layer, especially in regions of rapidly changing boundary conditions, i.e. transition from flat to curved surfaces. The information on the large-scale structure would not only assist in supporting our main conclusions, but it would also help to test whether rapid distortion approximations are reasonable. This information could be used in modifying present turbulence models that are based on the RDT approach. In regard to developing reliable turbulence models for complex turbulent boundary layers, it is suggested to combine a RDT type model for the outer portion of the boundary layer in combination with a standard, near-wall gradient-diffusion type model, i.e. Reynolds stress or k-ε.

Additional measurements of the third (spanwise) velocity components including the respective cross correlations is important to not only check the two-dimensionality of the flow field, but also to attain all components of the Reynolds stress and strain rate tensors.

Finally, detailed measurements of selected combinations of multiple strain rates under thermal boundary layer conditions have to be conducted to investigate how changes in the momentum transport affect the temperature fields under complex flow conditions. These experiments are necessary to address the nonlinear manner in which turbulence and turbulent heat transport respond to a three-dimensional strain field in wall-bounded flows. Combined with the results found in this study, it should be possible to make a major leap forward in the understanding and determination of convective heat transfer between the working fluid of a turbine and the material surfaces.

LIST OF REFERENCES

LIST OF REFERENCES

ALVING, A. E., SMITS, A. J. & WATMUFF, J. H. 1990 Turbulent boundary layer relaxation from convex curvature. *J. Fluid Mech.* **211**, 529.

ARORA, S. C. & AZAD, R. S. 1980 Turbulent kinetic energy in a flow with adverse pressure gradient. *AIAA Paper* 80-0073.

BANDYOPADHYAY, P. R. & AHMED, A. 1993 Turbulent boundary layers subjected to multiple curvatures and pressure gradients. *J. Fluid Mech.* **246**, 503.

BARLOW, R. S. & JOHNSTON, J. P. 1988a Structure of turbulent boundary layers on a concave surface. *J. Fluid Mech.* **191**, 137.

BARLOW, R. S. & JOHNSTON, J. P. 1988b Local effects of large-scale eddies on bursting in a concave boundary layer. *J. Fluid Mech.* **191**, 177.

BARLOW, R. S. & JOHNSTON, J. P. 1985 Structure of turbulent boundary layers on a concave surface. Stanford University Report, **MD-47**.

BASKARAN, V., SMITS, A. J. & JOUBERT P. N. 1987 A turbulent flow over a curved hill. Part 1. *J. Fluid Mech.* **182**, 47.

BASKARAN, V., SMITS, A. J. & JOUBERT P. N. 1991 A turbulent flow over a curved hill. Part 2. *J. Fluid Mech.* **232**, 377.

BLACKWELDER, R. F. & KAPLAN, R. E. 1976 On the bursting phenomenon near the wall in bounded shear flows. *J. Fluid Mech.* **76**, 89.

BLACKWELDER, R. F. & KOVASZNAY, L. S. G. 1972 Large-scale motion of a turbulent boundary layer during relaminarization. *J. Fluid Mech.* **53**, 61.

BLAISDELL, G. A. & SHARIFF, K. 1996 Simulation and modeling of the elliptic streamline flow. *Center for Turbulence Research, Proceedings of the Summer Program 1996.*

BOGARD, D. G. & TIEDERMAN, W. G. 1986 Burst detection with single-point velocity measurements. *J. Fluid Mech.* **162**, 389.

BOGARD, D. G. 1982 Investigation of burst structures in turbulent channel flows through simultaneous flow visualization and velocity measurements. Ph.D. Thesis, Purdue University, West Lafayette, IN.

BRADSHAW, P. 1973 Effects of streamline curvature on turbulent flow. *AGARDograph* 169.

BRADSHAW, P. 1975 Review - Complex turbulent flows. *ASME J. Fluids Eng.*, 146.

BRADSHAW, P. 1994 Turbulence: the chief outstanding difficulty of our subject. *Exp. Fluids* **16**, 203.

BRADSHAW, P. 1996 Turbulence modeling with application to turbomachinery. *Prog. Aerospace Sci.* **32**, 575.

CEBECI T. & BRADSHAW, P. 1977 Momentum transfer in boundary layers. Hemisphere Publishing.

CHIWANGA, S. C. & RAMAPRIAN, B. R. 1993 The effect of convex wall curvature on the large-scale structure of the turbulent boundary layer. *Experimental Thermal and Fluid Science* **6**, 168.

CLAUSER, F. C. 1954 Turbulent boundary layers in adverse pressure gradients. *J. Aeronaut. Sci.* **21**, 91.

DURBIN, P. A. & BELCHER, S. E. 1992 Scaling of adverse-pressure-gradient turbulent boundary layers. *J. Fluid Mech.* **238**, 699.

EVANS, R. L. 1985 Freestream turbulence effects on turbulent boundary layers in an adverse pressure gradient. *AIAA J.* **23**, 1814.

FOX, R. W. & MCDONALD, A. T. 1985 *Introduction to fluid mechanics*. John Wiley & Sons.

GENCE, J. N. & MATHIEU, J. 1979 On the application of successive plane strains to grid-generated turbulence. *J. Fluid Mech.* **93**, 501.

GIBSON, M. M. 1988 Effects of surface curvature on the law of the wall. *Near-Wall Turbulence*, 1988 Zoran Zaric Memorial Conference, Edited by S.J. Kline & N.H. Afgan, Hemisphere Publ. Corp.

GIBSON, M. M. 1984 Effects of streamline curvature on turbulence. *Frontiers in Fluid Mechanics* (S.H. Davis, J.L. Lumley, Eds.) Springer Verlag, 184-198.

GIBSON, M. M., VERRIOPOULOS, C. A. & VLACHOS, N. S. 1984 Turbulent boundary layer flow on a mildly curved convex surface. *Exp. Fluids* **2**, 17.

GILLIS, J. C. & JOHNSTON, J. P. 1983 Turbulent boundary layer flow and structure on a convex wall and its redevelopment on a flat wall. *J. Fluid Mech.* **135**,123.

HINZE, J. O. 1975 *Turbulence*. McGraw Hill, New York, 75.

HOFFMAN, P. H., MUCK, K. C. & BRADSHAW, P. 1985 The effect of concave surface curvature on turbulent boundary layers. *J. Fluid Mech.* **161**, 371.

HUNT, I. A. & JOUBERT, P. N. 1979 Effects of small streamline curvature on turbulent duct flow. *J. Fluid Mech.* **91**, 633.

KLINE, S. J. & MCCLINTOCK, F. A. 1953 Describing uncertainties in single sample experiments, *Mech. Eng.*, 3.

KLINE, S. J., REYNOLDS, W. C., SCHRAUB, F. A. & RUNSTADLER, P.W. 1967 The structure of turbulent boundary layers. *J. Fluid Mech.* **30**, 741.

KOSKIE, J. E. 1991 Turbulence structure and polymer drag reduction in adverse pressure gradient boundary layers. PhD Thesis, Purdue University, West Lafayette, IN.

LIAKOPOLOUS, A. 1984 Explicit representations of the complete velocity profile in a turbulent boundary layer. *AIAA Journal* **22**, 844.

LIAN, Q. X. 1990 A visual of the coherent structure of the turbulent boundary layer in flow with adverse pressure gradient. *J. Fluid Mech.* **215**, 101.

LU, S. S. & WILLMARTH, W. W. 1973 Measurements of the Reynolds stress in a turbulent boundary layer. *J. Fluid Mech.* **60**, 481.

MAXEY, M. R. 1982 Distortion of turbulence in flows with parallel streamlines *J. Fluid Mech.* **124**, 261.

MCLAUGHLIN, D. K. & TIEDERMAN, W. G. 1973 Biasing correction for individual realization of laser velocimeter measurements in turbulent flows. *Phys. Fluids* **16**, 2082.

MOFFAT, R. J. 1988 Describing the uncertainties in experimental results. *Exp. Thermal Fluid Sci.*, **3**, 3.

MOSER, R. D. & MOIN, P. 1987 The effects of curvature in wall-bounded turbulent flows. *J. Fluid Mech.* **175**, 479.

MUCK, K. C., HOFFMAN, P. H. & BRADSHAW, P. 1985 The effects of convex curvature on turbulent boundary layers. *J. Fluid Mech.* **161**, 347.

NAGANO, Y., TAGAWA, M. & TSUJI, T. 1991 Effects of adverse pressure gradients on mean flows and turbulence statistics in a boundary layer. *8th Symposium on Turbulent Shear Flows*, University of Munich, **2-3**.

NARASHIMHA, R. & SREENIVASAN, K. R. 1979 Relaminarization of fluid flows. *Advances in Applied Mechanics*, **19**, Indian Institute of Science, Bangalore, India, 221.

NARASHIMHA, R. & SREENIVASAN, K. R. 1973 Relaminarization in highly accelerated turbulent boundary layers. *J. Fluid Mech.* **61**, 417.

NARAYANAN, M. A. B. & RAMJEE, V. 1969 On the criteria for reverse transition in a two-dimensional boundary layer flow. *J. Fluid Mech.* **35**, 225.

PATEL, V. C. & SOTIROPOULOS, F. 1997 Longitudinal curvature effects in turbulent boundary layers. *Prog. Aerospace Sci.* **33**, 1.

PRABHU, A. & RAO, B. N. S. 1981 Turbulent boundary layers in a longitudinally curved stream. *Report 81 FM 10,* Department of Aeronautical Engineering, Indian Institute of Science, Bangalore, India.

RAMAPRIAN, B. R. & SHIVAPRASAD, B. G. 1978 The structure of turbulent boundary layers along mildly curved surfaces. *J. Fluid Mech.* **85**, 273.

ROBINSON, S. K. 1991 Coherent motions in the turbulent boundary layer. *Ann. Rev. Fluid Mech.* **23**, 601.

RUNSTADLER, P. G., KLINE, S. J. & REYNOLDS, W. C. 1963 An experimental investigation of flow structure of the turbulent boundary layer. *Report No. MD-8.* Dept. Mech. Engr., Stanford University, Stanford, CA.

SAMUEL, A. E. & JOUBERT, P. N. 1974 A boundary layer developing in an increasingly adverse pressure gradient. *J. Fluid Mech.* **66**, 481.

SCHOFIELD, W. H. 1981 Equilibrium boundary layers in moderate to strong adverse pressure gradients. *J. Fluid Mech.* **113**, 91.

SCHWARZ, A. C. & PLESNIAK, M. W. 1996a The influence of interacting strain rates on turbulence in convex boundary layers. *Phys. Fluids* **8**, 3163.

SCHWARZ, A. C. & PLESNIAK, M. W. 1996b Convex turbulent boundary layers with zero and favorable pressure gradients, in press ASME *J. Fluids Eng.* **118**, (Dec. 1996).

SIMON, T. W. & HONAMI, S. 1981 Incompressible flow entry cases having boundary layers with streamwise wall curvature (0230). *Final Evaluation Report for the* 1980-81 *AFOSR-HTTM-Stanford Conf. on Complex Turbulent Flows: Comparison of Computation and Experiment, Thermosci. Div., Mech. Engng Dept, Stanford.*

SMITS, A. J., MATHESON, N. & JOUBERT, P. N. 1983 Low-Reynolds-number turbulent boundary layers in zero and favorable pressure gradients. *J. Ship Res.* **27**, No. 3, 147.

SMITS, A. J., YOUNG, S. T. B. & BRADSHAW, P. 1979 The effect of short regions of high surface curvature on turbulent boundary layers. *J. Fluid Mech.* **94**, 209.

SO, R. M. C. & MELLOR, G. L. 1973 Experiment on convex curvature effects in turbulent boundary layers. *J. Fluid Mech.* **60**, 43.

SPALART, P. R. & SHUR, M. 1997 Private Communication.

SPALART, P. R. 1988 Direct simulation of a turbulent boundary layer up to $Re_\theta = 1410$ *J. Fluid Mech.* **187**, 61.

SREENIVASAN, K. R. 1985 The effect of contraction on a homogenous turbulent shear flow. *J. Fluid Mech.* **154**, 187.

TENNEKES, H. & LUMLEY, J. L. 1972 *A first course in turbulence.* MIT Press.

TSUJI, Y. & MORIKAWA, Y. 1976 Turbulent boundary layer with pressure gradient alternating in sign. *Aero. Quarterly* **27**, 15.

VAN DEN BERG, B. 1984 Production of turbulence according to the transport equations. National Aerospace Laboratory NLR Report, **MP 84030 U**.

WALKER, D. T. & TIEDERMAN, W. G. 1988 Turbulence structure and mass transport in a channel flow with polymer injection. Report PME-FM-88-2, Purdue University, W. Lafayette, IN.

WEBSTER, D. R., DEGRAAFF, D. B & EATON, J. K. 1996 Turbulence characteristics of a boundary layer over a two-dimensional bump. *J. Fluid Mech.* **320**, 53.

WHITE, F. M. 1974 *Viscous fluid flow*, McGraw Hill, New York, 478.

WHITE, J. B. & TIEDERMAN, W. G. 1990 The effect of adverse pressure gradient on the turbulent burst structure in low-Reynolds number equilibrium boundary layers. *Proceedings of the 12th Symposium on Turbulence*, University of Missouri-Rolla, Rolla, MO, A5.1.

YANTA, W. J. & SMITH, R. J. 1973 Measurements of turbulence transport properties with a laser Doppler velocimeter. *AIAA Paper No. 73-169*.